ORIGAMI-INSPIRED STRUCTURES AND MATERIALS: ANALYSIS AND
METAMATERIAL PROPERTIES
AND
SEISMIC DESIGN OF HYBRID MASONRY STRUCTURAL SYSTEMS

BY

MARYAM EIDINI-NEZHAD

DISSERTATION

Submitted in partial fulfillment of the requirements
for the degree of Doctor of Philosophy in Civil Engineering
in the Graduate College of the
University of Illinois at Urbana-Champaign, 2015

Urbana, Illinois

Doctoral Committee:

      Professor Iwona Jasiuk, Chair
      Professor Taher Saif
      Professor Sascha Hilgenfeldt
      Assistant Professor Ahmed Elbanna

Abstract

This dissertation includes two major sections. The first section presents the research on creating and studying novel classes of origami-inspired metamaterials and structures. The second section deals with seismic design of hybrid masonry structural systems.

1) Origami-Inspired Structures and Materials

Origami, the traditional Japanese art of paper folding, has been recognized to be a significant source of inspiration in science and engineering. Specifically, its principles have been used for innovative design of mechanical metamaterials for which material properties arise from their geometry and structural layout. Most research on origami-inspired materials relies on known patterns, especially on the Miura-ori, i.e., a classic origami pattern with outstanding properties and a wide range of applications.

Motivated by outstanding properties and a broad range of applications of the Miura-ori, in this dissertation, inspired by the kinematics of a one-degree of freedom zigzag strip, we create a novel class of cellular folded sheet mechanical metamaterials. The class of the patterns combines origami folding techniques with kirigami cutting. Using both analytical and numerical models, we study the key mechanical properties of the folded materials. We show that they possess properties as remarkable as those of the Miura-ori on which there has been a surge of research interest. Consequently, the introduced patterns are single degree of freedom (DOF), developable, rigid-foldable and flat-foldable.

Furthermore, we show that depending on the geometry, these materials exhibit both negative and positive in-plane Poisson's ratio. By introducing a novel class of zigzag-base materials, the current study extends the properties of the Miura-ori to those of the class of one-DOF zigzag-base patterns, and our work shows that Miura-ori is only one pattern in this class with such properties. Hence, by expanding upon the design space of the Miura-ori, our patterns are appropriate for a wide range of applications, from mechanical metamaterials to light cellular foldcore sandwich panels and deployable structures at both small and large scales. Furthermore, this study unifies the concept of the in-plane Poisson's ratio from the literature for similar materials and extends it to this novel class of zigzag-base folded sheet metamaterials.

Moreover, in this dissertation, by dislocating the zigzag strips of a Miura-ori pattern along the joining ridges, we create a class of one-degree of freedom (DOF) cellular mechanical metamaterials. We further show that dislocating zigzag strips of the Miura-ori along the joining ridges preserves and/or tunes the outstanding properties of the Miura-ori. The introduced materials are lighter than their corresponding Miura-ori patterns due to the presence of holes in the patterns. They are also amenable to similar modifications available for Miura-ori which make them appropriate for a wide range of applications across the length scales.

Additionally, we study the Eggbox pattern. Similarly to Miura-ori, a regular Eggbox folded sheet includes parallelogram facets which are connected along fold lines. However, Eggbox sheets cannot be folded from a flat sheet of material, and contrary to Miura-ori which has received considerable interest in the literature, there are fewer studies available on Eggbox folded sheet material. By employing both analytical and numerical models, we review and study the key in-plane mechanical properties of the Eggbox folded sheet, and we present cellular folded metamaterials containing

Miura-ori and Eggbox cells. The entire structure of the folded materials is a one-DOF mechanism system and, similarly to Eggbox sheets, the materials composed of layers of Eggbox folded sheets are bi-directionally flat-foldable, resulting in a material flexible in those directions, but stiff in the third direction.

2) Seismic Design of Hybrid Masonry Structural Systems

Hybrid masonry is an innovative seismic lateral-load resisting system. The system comprises reinforced masonry panels within a steel-framed structure as well as steel connector plates which attach the surrounding steel frame to the masonry panel. Depending on the interfacial conditions between a masonry panel and the steel frame, the system is categorized into three major groups: Types I, II and III.

The first part of the research on hybrid masonry systems, in this dissertation, includes a series of exploratory studies aimed at understanding the global behavior of various types of hybrid masonry panels and setting the stage for the study on seismic design of the systems. In this regard, computational analyses were carried out to study the distribution of lateral forces between a masonry panel and a frame in various types of hybrid masonry structural systems. The results are used to demonstrate differences in lateral-force distributions in hybrid masonry systems with different boundary conditions and with various panel aspect ratios as well as with different stiffness of the wall to that of the frame.

Furthermore, this study presents the general methodology for seismic design of Type I hybrid masonry systems as well as the steps of a capacity design process in which two favorable ductile modes of behavior are considered: steel connector plates behaving as fuses or flexural yielding of the masonry panels. Moreover, using the proposed approaches we design several prototype buildings located in a high seismic region and investigate viability of hybrid masonry as a new seismic lateral-load resisting system. According to this design framework and the exploratory studies, both approaches are shown to be feasible for developing realistic system configurations.

Finally, in this study, an integrated approach for performance-based seismic analysis and design of hybrid masonry Type I systems with fuse connector plates is presented. The procedure used in this study is based on the Capacity Spectrum Method. The proposed method includes an iterative process through which a hybrid masonry structural system with fuse connector plates is designed depending on its energy dissipation capacity. In this regard, the value of the system R factor is regulated in the process. In this study, application of the method for design of a sample hybrid masonry building system is presented.

To my family

Acknowledgements

First and foremost, I would like to thank all those genuine professors who promote and encourage academic integrity, sincerity and responsibility, *by their actions*.

I would like to thank Dr. Jasiuk, Dr. Elbanna, Dr. Saif and Dr. Hilgenfeldt for serving on my dissertation committee and for their feedback.

I gratefully acknowledge the support of Schlumberger fellowship during the first two years of my PhD studies. Nevertheless, the prestigious fellowship appeared like an obstacle on my academic progress because of the inappropriate treatment of the award by the others and that the issue was not resolved at the early stages when it was reported. When there is a mistake (even intentional mistakes), the right and the sensible way is to compensate for the mistake rather than covering up the mistake by numerous other mistakes and transferring the mistake from one to another (and consequently leaving the person among numerous unnecessary problems). I am glad though for having to change my research area. Apart from experiencing a new research area, overcoming the unusual challenges and the unnecessary difficulties that I have faced, has improved my self-confidence and has further proved to me that always "*honesty is the best policy*".

I am thankful to all my friends, teachers and professors for their support and/or friendship.

Last but not least, I wish to express my sincere gratitude to my family for their never-ending support and encouragement.

Table of Contents

List of Tables

List of Figures

1 Introduction

This dissertation includes two major parts. The first part includes Chapters 2 to 5 and focuses on origami-inspired structures and materials. The second part, i.e. Chapters 6 to 8, is about seismic design of hybrid masonry structural systems.

Origami-inspired structures and materials

Origami, the Japanese traditional art of paper folding, has proven to be a substantial source of inspiration for engineering applications. Among advantages of origami-inspired materials and structures are: ability of sustaining large unsupported spans, capability of maintaining large deformation without deforming the base material in rigid origami, possessing both the shape and the structure at the same time due to corrugation and folding and having anisotropy in deformation modes. These characteristics make origami-like structures specifically suited for applications in morphing structures, transformable and deployable structures where structures are capable of changing shape and mechanical properties in response to external excitations, i.e. a feature suited for sustainable developments.

Chapter 2 provides an overall view on origami engineering. Chapters 3 to 5 include self-contained articles. Chapter 3 is about Miura- and Eggbox-inspired materials. In this chapter, mechanical properties of Eggbox and Miura-ori are both reviewed and studied, and the geometry of one-degree of freedom (DOF) materials containing both Miura-ori and Egg-box are

introduced. Chapter 4 is about a novel class of origami- and kirigami-inspired mechanical metamaterials. In this Chapter, by creating a class of zigzag-base patterns, we extend the properties of the Miura-ori, i.e. the most remarkable origami pattern with metamaterial properties, to the class of one-DOF zigzag-base patterns. In Chapter 5, we present a novel technique, i.e. dislocating the zigzag strips of the Miura-ori pattern along the joining ridges, to tune and/or preserve the mechanical properties of the Miura-ori. The technique can be used to design adaptable and foldable metamaterials and structures whose properties can be tuned depending on the external excitations. Moreover, we show that the zigzag-base materials introduced in Chapters 4 and 5, due to possessing cellular structures, are naturally lighter than their corresponding ones made from the Miura-ori pattern. Hence, they are well-suited for a broad range of applications at various length scales.

Seismic design of hybrid masonry structural systems

Hybrid masonry in a relatively new lateral load resisting system. The system includes reinforced masonry panels within a framed steel structure. In the system, masonry panels are linked to the surrounding steel frame via steel connector plates. Depending on the interfacial conditions between a masonry panel and the surrounding steel frame, hybrid masonry systems are categorized into three major groups: Types I, II and III. The second section of this dissertation focuses on seismic design of hybrid masonry structural systems. In this regard, Chapters 6 to 8 include self-contained articles. Chapter 6 presents lateral load distribution between a masonry panel and a frame for various types of hybrid masonry systems. Moreover, this chapter sets the stage for further studies on seismic design of these systems. In Chapter 7, we describe the general approach for seismic design of hybrid masonry Type I, considering two cases of plasticity concentrated in steel connectors or in the flexural yielding of steel bars of the masonry panels. Employing these two design approaches, viability of hybrid masonry Type I systems are also studied in this chapter. Finally, Chapter 8 presents a general framework for capacity spectrum method-based seismic design of hybrid masonry Type I with fuse connector plates.

2 Origami Engineering

Origami is the Japanese ancient art of paper folding in which "*ori*" means to fold and "*kami*" means paper. Developing complex spatial objects from a flat sheet of material using origami folding techniques has long attracted attention in science and engineering. Origami has shown to be a significant source of inspiration for innovations and in this regard, "*orimimetics*" refers to the application of this oriental art to solve technical problems [1]. Origami techniques have been used from folding of maps to construction of airbags, car crash boxes, medical stents, tents and shelters, instant food packaging, grocery bags, stadium roofs, etc. Folds and corrugations are also present in natural systems, at various length scales from protein ribbons and DNA to tree leaves and insect wings [2], and in these systems controlled folding and unfolding aims to improve functional and (or) mechanical properties.

Origami can be broadly categorized into five areas of application in engineering (Figure 2.1). *Deployable structures*: where foldable structures are the solution of choice due to limited available transportation space such as deployable solar panels [3, 4] medical stents [5] and deployable space telescope [6]; *Energy absorbing systems*: for instance, sandwich panel cores [7], and airbag folding [8] and origami crash boxes [9]; *Metamaterials*: such as stacked Miura-ori [10]; *Improving mechanical properties of material by adding corrugations and folds*: for example in solar sail structures [11]. *Other engineering applications* of origami include improving acoustic quality by corrugation [12], resonance frequency tuning in electro- magnetic devices [13] and others.
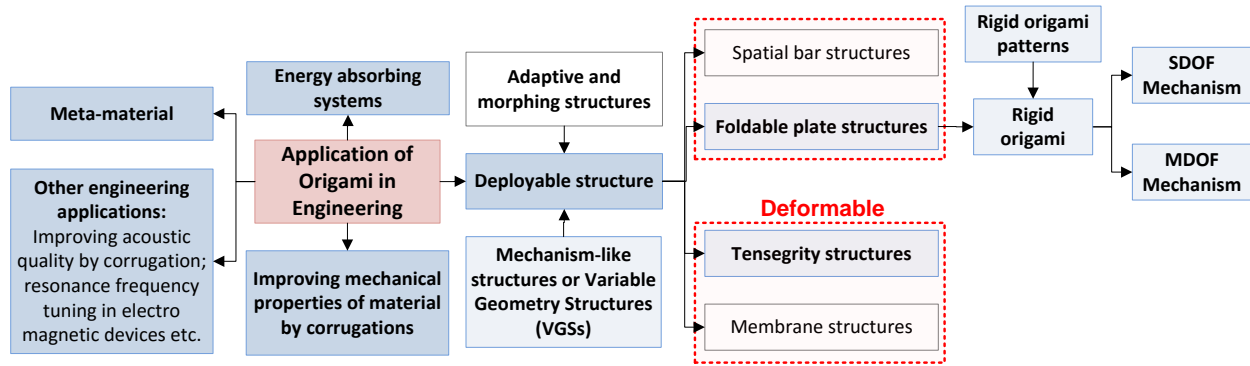
Figure 2.1: Applications of origami in Engineering with emphasis on deployable origami structures.
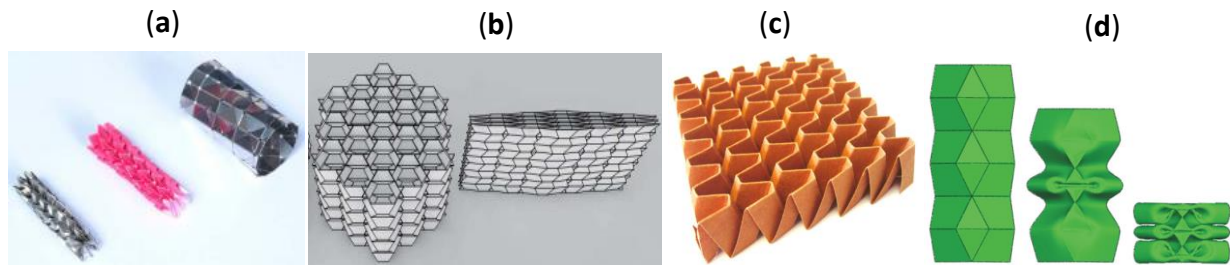
Figure 2.2: Some applications of origami in engineering. (**a**) Deployable medical stents [14]. (**b**) Metamaterial [15]. (**c**) Folded core [16]. (**d**) Car crash boxes [9].

Figure 2.1 illustrates the application of origami in engineering in which the emphasis is placed on the rigid-origami branch of deployable structures as the potential application of origami-inspired structures. The classification of deployable structures in Figure 2.1 is also based on their kinematic and morphological characteristics offered by Hanaor and Levy [17].

2.1 Origami Engineering and Sustainable Development

Rapid reduction of natural resources, increasing of the world population and the change in the climate are placing demands on structural engineering towards a sustainable engineering. To develop sustainable design, some issues must be addressed in construction industry such as environmentally friendly systems, reduced level of energy consumption, operation and

optimization and others [18]. Moreover, the new trends in structural development show an increasing interest in kinetic architecture [19] which is in accordance with sustainable development. In the future, engineering structures can become highly smart, dynamic and adaptive with the capability of transform themselves to optimize their physical and mechanical performance in response to both external and internal excitations. Rigid origami is a subclass of origami structures in which rigid panels are linked through perfect hinges leading to an entirely geometric mechanism. Also, in rigid origami, there is a continuous path between unfolded and folded states. Consequently, rigid origami due to its kinetic characteristic has the potential for application in adaptive systems as well as in self deployable micro mechanisms. When employing thick panels, rigid origami is appropriate for fabrication of large scale gravity-load carrying objects [20]. The major advantages of origami-inspired structures which make them appropriate for applications in sustainable engineering are highlighted as follows:

- Origami-inspired deployable structures can be prefabricated on site, and can be potentially designed to carry gravity and lateral loads in a partially folded configuration. Hence, rapid manufacturing and easy transportability make these types of structures appropriate for reusable construction allowing minimal installation cost.

- They can be adjusted for use in various environmental conditions by folding or unfolding. Hence, they are suitable to create adaptive building envelopes and façades, convertible building covers, and are promising to provide solutions to some of the challenges in the construction industry, i.e. to provide low energy consumption and green sustainable buildings. One may find examples of applications in retractable roof structures for adjusting the light in a stadium [21, 22].

- Rigid origami is capable of sustaining large displacements without stretching of the base material which makes it potentially suitable for transformable structures [23].

- Single-Degree of Freedom (SDOF) rigid mechanism (e.g., Miura-ori) is appropriate for low-energy, efficient and controllable deployable structures [24].

- Multi-degree of freedom (MDOF) rigid origami such as the transformable shell proposed by Resch and Christiansen [25] can be potentially used to cover arbitrary geometric surfaces by stabilizing the shell structure via effective stiffening methods, such as negative pressure, as suggested by Tachi [26]. Hence, due to having both the structure

and providing the form, origami structures can be utilized to construct complex forms by removing the need for complex understructure previously needed to support building covers.

- Origami-inspired materials can be customized to deform easily in some directions while to keep their rigidity in others. Anisotropy in deformation modes makes them suitable for some novel engineering applications such as in morphing structures. They also possess the capability of being designed for a favorable coupling between bending and extension [23].

- They are capable to sustain large span shell structures - see for example, the Pseudo-Cylindrical Concave Polyhedral (PCCP) shells proposed by Miura [27].

2.1.1 Sustainable design in civil engineering and architecture using origami techniques

Adaptive structures that can transform and optimize their functions in response to environmental and functional stimuli have gained significant attention in various areas of engineering. Retractable roofs and environmentally responsive structures such as adaptive building covers and façades [21], responsive shading [28] and ventilation systems are examples of a new generation of architecture using kinetic and controllable smart structures (see Figure 2.3 and Figure 2.4). For civil engineering applications of origami-inspired structures, both folding efficiency and structural performance of the system are of interest. Origami has been applied by architects to attain visual appeal, shape, structure and kinetics. Various folding techniques, geometry and tessellation of a pattern provide versatility to origami-inspired structures making them potentially appealing for civil engineering applications. The Investment Council Headquarters of Abu Dhabi, Al-Bahr towers (Figure 2.3) are equipped with origami-inspired kinetic shading and solar responsive screen which performs as a secondary façade, controls solar light and optimizes the natural light internally. This type of kinetic and responsive shading decreases the energy consumption.
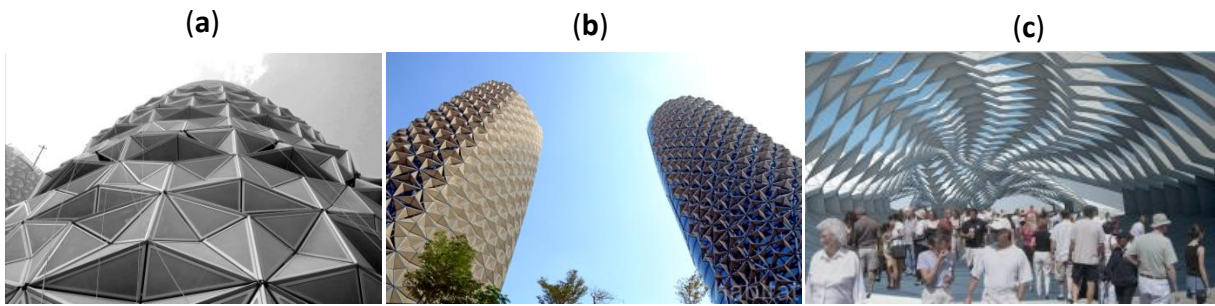
Figure 2.3: (**a**, **b**) Investment Council Headquarters of Abu Dhabi, Al Bahr towers [29], with origami-inspired kinetic shading and solar responsive screen; (**c**) "lightweight origami structure" [28].

Figure 2.4: Dynamic façade; Kiefer Technic showroom Bad Gleichenberg Giselbrecht (pictures by Paul Ott).

2.2 Application of Origami in Engineering

As mentioned in the introduction and illustrated in Figure 2.1, existing applications of origami in engineering can be classified into five general groups: deployable structures, energy absorbing devices, modifying mechanical properties of material by introducing corrugations, metamaterials and other engineering applications. In the following, more details are provided on these applications.

2.2.1 Deployable structures

For common applications of pleating, the folds are generally used to enhance flexibility or motion. Examples include pleated skirts, Japanese traditional and decorative fans and pleated pipelines. Using this characteristic of pleating, deployable structures can be realized using

origami techniques and they can be categorized under the class of adaptive and morphing structures. Deployable structures can transform from a stowed (folded) configuration to an unfolded state while having the capability of carrying load. Hence, origami-like deployable structures are transformable structures whose functions can be optimized in response to environmental and functional stimuli. For the purpose of deployable structures, SDOF rigid mechanism is appropriate for low-energy, efficient and controllable actuation. However, MDOF mechanism is also applicable for deployable structures. For example, Kuribayashi and You developed a medical stent using water-bomb origami pattern, an MDOF mechanism, to open collapsed arteries [14].

2.2.1.1 *Rigid foldable origami (rigid origami)*

The mathematical theory of rigid origami has been studied by various researchers [30, 31, 32, 33, 34, 35]. In rigid origami, fold lines act as hinges and rigid panels (facets) bend along the fold lines, and mathematics of rigid origami implies the presence of soft internal mechanism in the system [34]. Furthermore, for rigid foldability, the entire folding process is of interest and it is about the existence of a continuous path between the unfolded and folded states, whereas flat foldability pays attention to the final folded state. As Figure 2.1 shows, rigid origami which is categorized under adaptive and morphing structures, due to its kinetic behavior, has the potential to serve as adaptable systems such as adaptive architectural façades and covers [28]. Also, the stiffness of a folded sheet, for example Miura-ori sheet, can change at various folded states depending on folding angles. Therefore, it has the potential to be applied as an adaptive structural system for a structure subjected to a varying external load. For rigid origami, in general, the number of kinematic degrees of freedom (DOF) is equal to: DOF = N –3M, where N is the number of fold lines and M is the number of inner vertices.

2.2.2 Impact absorbing devices

Folded sheets can be used as car crash boxes (Figure 2.2(d)). In automobiles, energy absorption devices, i.e. crash boxes, are installed to absorb energy in the event of a car crash. Introducing an origami folding into a car crash box lowers the initial buckling force due to geometric

imperfections, and also forces the buckled mode to a pre-designated favorite buckled shape with higher energy absorption capacity [9]. Moreover, the origami technique of folding a flat sheet of material into three dimensional folded structures has been used to construct packaging material [16] and impact absorbing devices [7]. Hagiwara [36] also pointed out that manufacturing vehicles, with origami-inspired structures, has the potential to reduce the impact energy from collisions. To address the idea by Hagiwara, using the capability of easily crushing and restoring back of origami folded objects, Wu et al. [37] introduced a Cylindrical Origami Structure (COS) taking advantage of *"progressive collapse deformation"* to absorb the impact energy in the event of a collision.

2.2.3 Modifying mechanical properties of materials and structures by corrugation

Folding increases the out-of-plane stiffness of plates. Hence, covering of a large span is possible by a folded plate (Figure 2.5). A folded sheet can also be used in sandwich panel cores as it increases the stiffness of the system [16]. Origami patterns, with large out-of-plane stiffness while having a small planar stiffness, can be applied to reduce the out-of-plane displacement of some engineering systems.
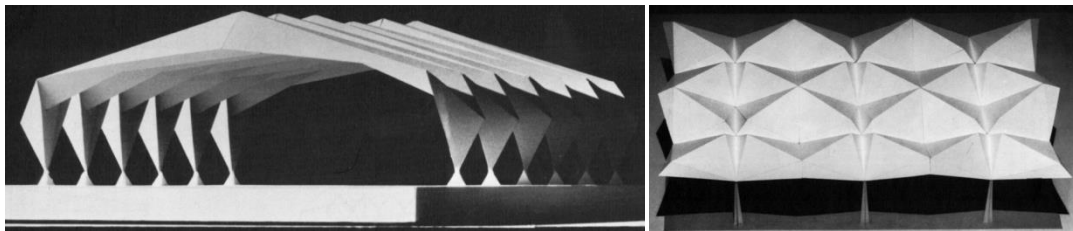
Figure 2.5: Folded plates [38].

2.2.4 Metamaterials

Metamaterials are artificially engineered materials which exhibit the material properties beyond those found in natural materials. Deployable cellular solids [15], folded cellular stacked Miura metamaterial with omni-directional negative Poisson's ratio [10], Miura-ori sheet with in-plane

and out-of-plane Poisson's ratios of opposite signs [23, 10, 39] and curved folded shell structures which can undergo large changes in Gaussian curvature without stretching at the material base (making it potentially appropriate for morphing surfaces [40, 41]) are examples of folded metamaterials.
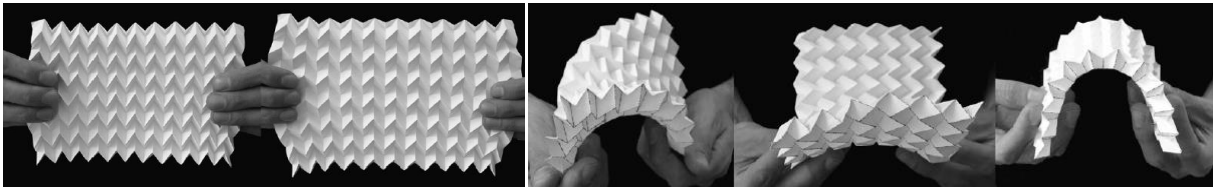
Figure 2.6: Miura-ori sheet with in-plane and out-of-plane Poisson's ratio of opposite signs [23].
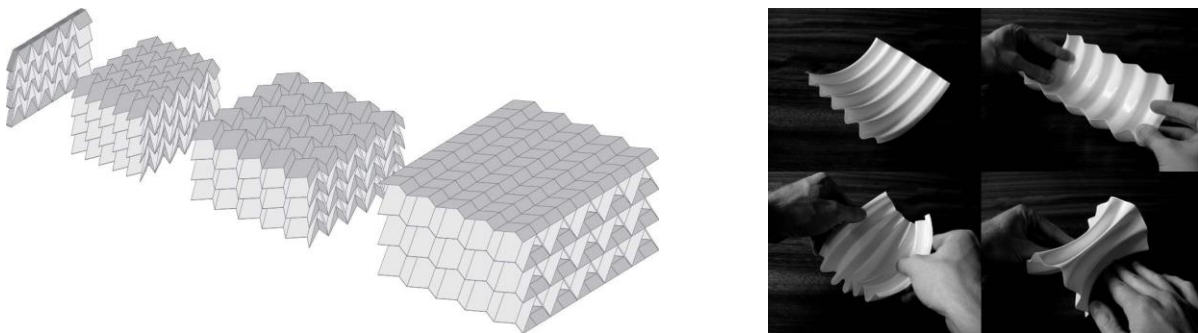
Figure 2.7: (**a**) Stacked Miura folds and unfolds uniformly with negative Poisson's ratio in all directions and highly anisotropic material properties [10]. (**b**) Curved corrugated shell structures [40].

2.2.5 Other engineering applications

Other applications of origami include, but are not limited to: resonance frequency tuning in electromagnetic devices such as "origami tunable frequency selective surfaces" [13] and "origami tunable metamaterial" [42], improving acoustic quality by corrugation and variable acoustic surfaces. Miura-ori pattern has been applied for the ceiling of Meguro Persimmon Hall in Tokyo due to the sound diffusion effect caused by its corrugated surface [12]. Application of Ron Resch for "Resonant Chamber, an interior envelope system that deploys the principles of rigid origami, transforms the acoustic environment through dynamic spatial, material and

electro-acoustic technologies. The aim is to develop a sound-sphere able to adjust its properties in response to changing sonic conditions, altering the sound of a space during performance and creating an instrument at the scale of architecture, flexible enough that it might be capable of being played" [43].

"Significant work in the areas of kinetic tessellated architectural systems and variable acoustic surfaces using specific geometry includes David Serero's 2005 "Variable Geometry Acoustical Domes", Mani Mani's 2009 "Tunable Sound Cloud", the current research of Brady Peters, particularly his 2011 "Distortion II" and Eddy Sykes' 2008 "Yakuza Lou" kinetic rigid origami structure" [43].
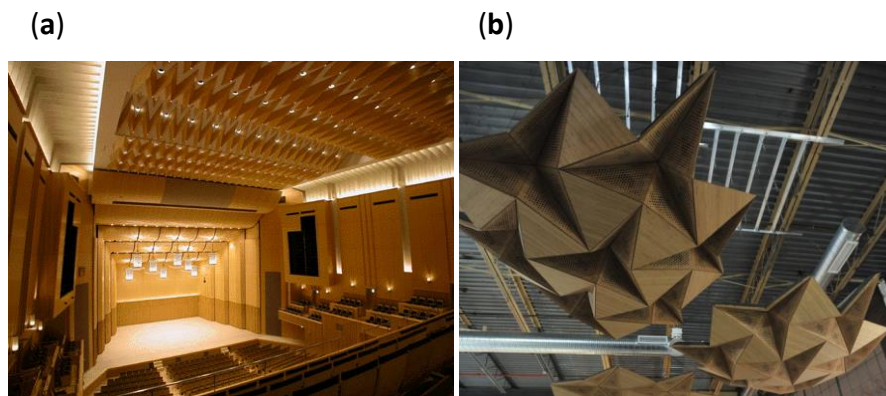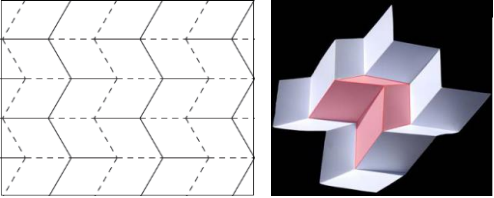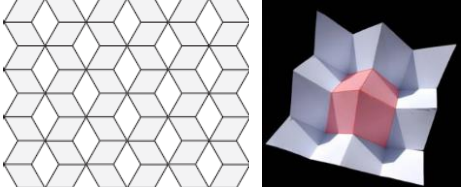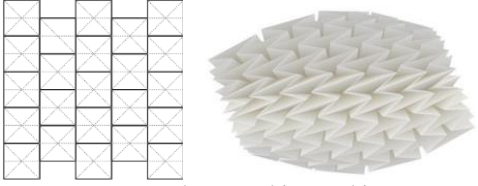
Figure 2.8: (**a**) Meguro Persimmon Hall in Tokyo with Miura-ori pattern applied for the ceiling [12]. (**b**) Resonant Chamber using Ron Resch pattern [43].

2.3   Major Origami Patterns Applied in Engineering

Origami folding can be used to construct three dimensional objects applicable in engineering from two dimensional sheets. Due to manufacturing difficulties, simple folding patterns are used in most applications of origami in engineering such as self-assembly of micro-devices, for example [44, 45] among others. Since the materials constituting the origami facets for civil engineering applications are mostly rigid, rigid origami patterns are of our interest in which the facets do not stretch and bending happens along the fold-lines. In Table 2.1, an overview of the fundamental and major folding patterns applied in engineering is provided. Also, the patterns
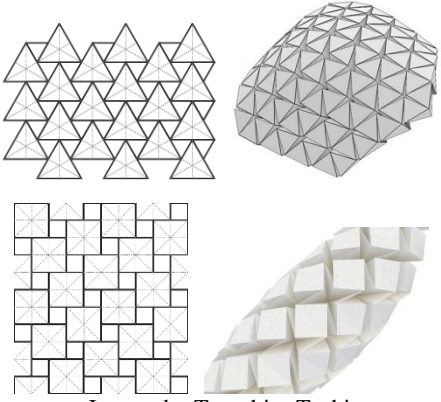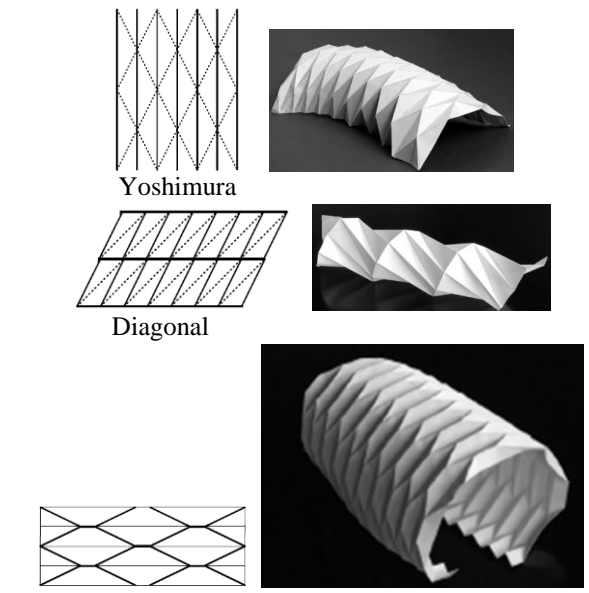
discussed in this section, are mainly selected based on their potential applications in structural engineering and architecture.

Table 2.1: Some major origami patterns applied in engineering, their properties and applications.

Miura-Ori (Herringbone pattern)	
Crease Pattern and folded Stage	Comment
 Images by Schenk and Guest	**Properties:** SDOF pattern; developable; rigid-foldable; flat-foldable; negative in-plane Poisson's ratio and positive out-of-plane Poisson's ratio [23, 10, 39]; possibility of stacking of Miura-ori sheets with various heights while keeping the same kinematics [10]. **Applications:** Folded core [46]; deployable solar panels [3]; curved folded core material [47]; folding of maps [48]; applied for ceiling in the Persimmon Hall in Tokyo due to its sound diffusion effect [12]. Stacked folded core as energy absorption systems [49]. Reprogrammable mechanical metamaterials [50]. Fluidic origami cellular system [51].
Egg-box	
Crease Pattern and folded Stage	Comment
 Images by Schenk and Guest	**Properties:** SDOF pattern; non-developable; rigid-foldable; bidirectional flat-foldable; positive in-plane Poisson's ratio and negative out-of-plane Poisson's ratio [23]. **Applications** "expansible surface structure" [52].
Waterbomb ("Namako" by Shuzo Fujimoto)	
Crease Pattern and folded Stage	Comment
 Images by Tomohiro Tachi	**Properties:** MDOF pattern (3 DOFs per unit cell); developable; flat-foldable; flexible (multi DOF) and complicated motion. Negative Poisson's ratio [53]. Cylinders constructed from waterbomb pattern are not generally rigid foldable [53], but a specific geometry can be found for cylinders with uniform radius making them rigidly foldable [54]. **Applications:** Medical stent [14]; packaging; textured material; cloth folding; deformable wheel robot [55].

12

Table 2.1 (cont.)

Ron Resch; Including 90 degree pattern	
Crease Pattern and folded Stage	Comment
Images by Tomohiro Tachi	**Properties:** MDOF pattern (3 DOFs per unit cell); developable; flexible; strong bending-extension coupling; negative Poisson's ratio. **Application:** Resonant chamber [56].

Yoshimura (Diamond), Diagonal and Hexagonal Yoshimura	
Crease Pattern and folded Stage	Comment
Yoshimura Diagonal Hexagonal Yoshimura Images from reference [57]	**Properties:** Inextensional post-buckling geometry; Increased circumferential bending stiffness while decreasing the in-plane stiffness; to cover a curved architectural surface, without the need to construct curved plates. **Application:** Pseudo-Cylindrical Concave Polyhedral (PCCP) [27]; submarine pressure hulls due to improved buckling capacity [58]; textured drinking cans [59]; lightweight Origami structure for day lighting modulation [28]; construction of curved architectural structures such as vaults by assembling of plane triangles [60]; textured deep submarine pipelines due to their substantial increase in propagation buckling capacity [61].

3 Miura- and Eggbox-inspired Cellular Folded Materials: Synthesis, Analysis and Mechanical Properties

Abstract

Miura-ori is a classic origami pattern with outstanding mechanical properties which has received considerable interest in the literature. Similarly to Miura-ori, a regular Eggbox folded sheet includes parallelogram facets which are connected along fold lines. However, Eggbox sheets cannot be folded from a flat sheet of material, and contrary to Miura-ori, there are fewer studies available on Eggbox folded sheet material. By employing both analytical and numerical models, we review and study the key in-plane mechanical properties of Miura-ori and Eggbox sheets, and present cellular folded metamaterials containing Miura-ori and Eggbox cells. The entire structure of the folded materials is a one-degree of freedom (DOF) mechanism system and, similarly to Eggbox sheets, the materials composed of layers of Eggbox folded sheets are bi-directionally flat-foldable, resulting in a material flexible in those directions, but stiff in the third direction. Moreover, a framework is provided to obtain the Poisson's ratio of both Miura-ori and Eggbox sheets. Apart from further investigation of the in-plane Poisson's ratios of these folded sheets, the framework can be employed to obtain the in-plane Poisson's ratios of similar, but more complex folded sheets for which analytical models are not available.

3.1 Introduction

Although mostly renowned for its visual appeal, origami, the Japanese art of paper folding has been a source of inspiration for designing cellular foldable materials [62, 63, 64, 15, 10, 65] and responsive materials and structures [66, 67], among many other applications. In this regard, Miura-ori, a classic origami folding pattern whose regular form constitutes four parallelogram facets linked via fold lines (Figure 3.1), has been employed for a wide range of applications spanning from folding of maps [48], folded-core cellular sandwich panels [68, 16] to the technologies such as deployable solar arrays [48, 24] and cellular materials and structures [10, 62]. Miura-ori can be folded from a flat sheet of material (*i.e.*, a developable pattern).

Folds and corrugations are also present in natural systems (Figure 3.2), at various scales, from protein ribbons and DNA to tree leaves and insect wings [2]- in these systems, controlled folding and unfolding is used to improve functional and (or) mechanical properties. For instance, folding patterns in insect wings include four panels rotating around four fold-lines intersecting at a point which is similar to a degree-four origami unit cell and, more specifically, to a Miura-ori cell [69]. Leaves of hornbeam (Carpinus betulus) and common beech (Fagus sylvaticus) have similar mechanism and folding pattern to that of Miura-ori [70] (Figure 3.2). In addition, a herringbone pattern forms due to axial compression of a planar stiff thin elastic film at the top of a soft substrate [71, 72, 73] which corresponds to the minimum energy configuration [74]. The pattern naturally arises in embryonic intestine as well [75, 76].
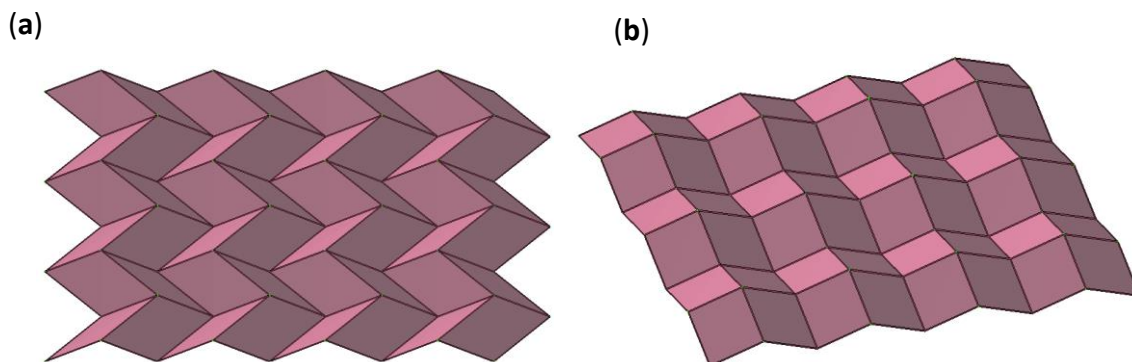
Figure 3.1: Illustration of 4 by 3 sheets of Miura-ori and Eggbox ($m_1=4$, $m_2=3$): (**a**) Miura-ori. (**b**) Eggbox.

Observing patterns similar to Miura-ori in biological systems has opened up a research path to discover associated mechanical, physical and mathematical properties [10, 39, 77]. Some of the most interesting properties of folded sheet material and structures arise basically due to their folding geometry. Miura-ori, for most ranges of geometry, is an auxetic material with a negative in-plane Poisson's ratio, whereas under bending the sheet exhibits positive Poisson's ratio, *i.e.*, the in-plane and out-of-plane Poisson's ratio of the sheet are of opposite signs [10, 39, 78].
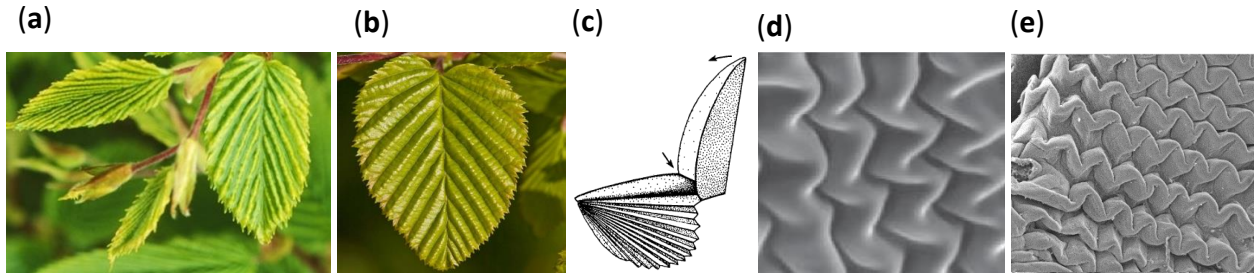
Figure 3.2: Herringbone pattern in natural systems. (**a**) Common beech [79]. (**b**) Hornbeam [80]. (**c**) Insect wing [69]. (**d**) Pattern formed by biaxial compression of a thin film at the top of a soft substrate [71]. (**e**) Natural pattern in turkey embryo [75].

Knowing that the Poisson's ratio of a partially folded Miura-ori sheet is not dependent on the height of the sheet, and that it is only a function of an angle in the horizontal plane, Schenk and Guest [10] introduced metamaterials by stacking Miura-ori sheets with different unit cell geometries while preserving the capability of folding and unfolding. Wei et al. [39] also studied the in-plane stretching and out-of-plane bending responses of the Miura-ori unit cell.

Eggbox is a bi-directionally flat-foldable pattern. It has been introduced as "*expansible surface structure*" by Brunner [52]. The sheet can be made by cutting Miura-ori crease pattern along the zigzags, and joining the strips with special alignment. Hence, a regular Eggbox sheet includes parallelogram facets which are connected along fold lines (Figure 3.1). The pattern cannot be folded from a flat sheet of material. Also, experimental tests [23] show that the sheet exhibits positive and negative Poisson's ratio under stretching and bending, respectively. Similarly to Miura-ori the in-plane and out-of-plane Poisson's ratios of Eggbox sheet are of opposite signs which is a remarkable characteristic of this folded sheet material [23].

Tachi and Miura described cellular materials [62] composed of Miura-base tubes [81] with

rhombus cross sections. The tube unit cell, shown in Figure 3.3(a), includes both Miura-ori and Eggbox cells overlapping by two parallelogram facets. By defining the geometry of Miura-ori and Eggbox cell in relation to an associated tube cell, we can relate the geometric parameters of Miura-ori to those of Eggbox as shown in Figure 3.3(a). The tubes assembled in various ways (e.g., side by side, interleaving etc.) can form the structure of the cellular materials. Special arrangements of Miura-ori and BCH$_2$ (*Basic Cell with Holes* in which a unit cell includes 2 large and 4 small parallelogram facets) [65] tubes form Eggbox surfaces (see Figure 3.4). Hence, similarly to Eggbox sheets, the materials shown in Figure 3.4 are bi-directionally flat-foldable, and the materials fabricated with those geometries are soft in two directions and stiff in the third orthogonal direction.

$$a = a_e \ , \ b = b_e \ , \ \beta_1 = \beta_{1e}, \ w = \ell_e, \ \phi = \phi_e, \ \psi = \psi_e$$
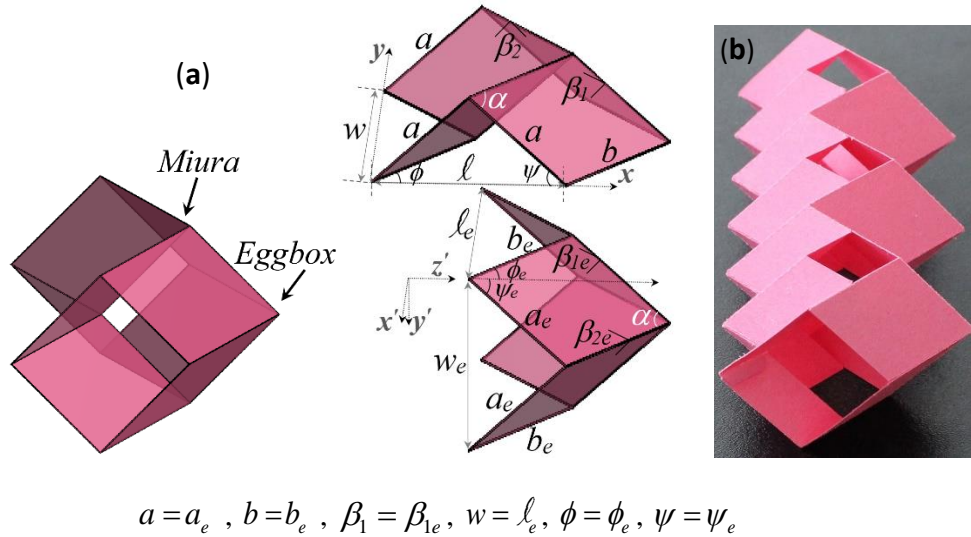
Figure 3.3: (**a**) Tube unit cell with a rhombus cross section decomposed into Miura-ori and Egg-box cells. The parameters shown in the figure are defined in the Sections on Miura-ori and Eggbox. (**b**) A BCH$_2$-based tube forming two different scales Eggbox surfaces at the sides.

In this study, we provide a general overview of the numerical modeling of origami-inspired structures, where the emphasis is placed on the bar framework approach available in the literature. Then, the key mechanical properties of Miura-ori and Eggbox patterns are reviewed and studied and, in this regard, the analytical models for the in-plane stiffness of Miura-ori available in the literature [39] are modified, and the in-plane Poisson's ratios and rigidities of Eggbox are derived. Moreover, a framework is provided to obtain the Poisson's ratio of both

Miura-ori and Eggbox sheets computationally, using the bar-framework origami structural modeling approach proposed by Schenk and Guest [23]. Apart from further investigation of the in-plane Poisson's ratios of Miura-ori and Eggbox sheets, the framework can be employed to obtain the Poisson's ratios of folded sheets with similar kinematics for which analytical models are not available. Finally, we introduce and describe folded one-DOF mechanism metamaterials including both Miura-ori and Eggbox cells.

(a) **(b)**
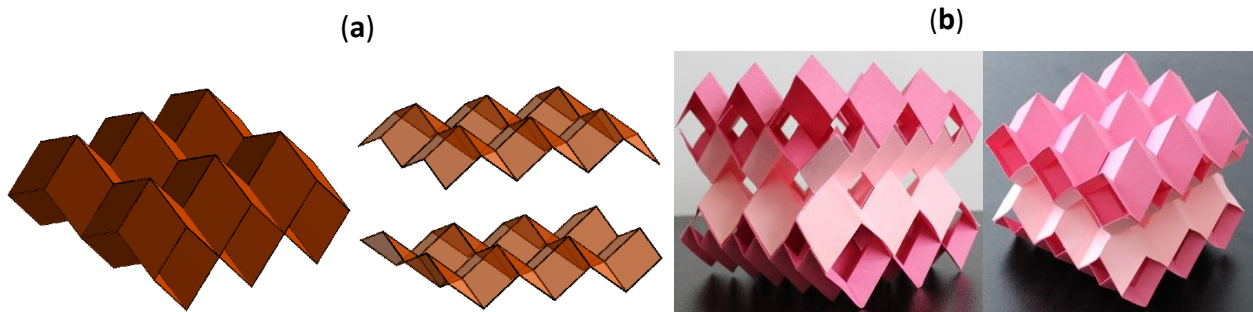
Figure 3.4: Tubular materials forming Eggbox surfaces. (**a**) A tubular material decomposed to layers of Eggbox sheets. (**b**) A novel material created with special assembly of BCH_2 sheets resulting in Eggbox surfaces parallel to the horizontal plane.

3.2   Numerical Modeling of Origami-like Structures

In a folded paper, bending occurs along the fold lines, and the paper has no bending stiffness. Therefore, it can be approximated either using rigid plates hinged together along the fold lines or using membrane elements with high stretching stiffness and no bending stiffness. Another modeling scheme is simulation of origami using pin-jointed truss framework in which the fold-lines and vertices are modeled using rigid bar elements and perfect hinges, respectively.

Two types of analysis in origami structures are of interest: kinematic analysis and stiffness analysis. In general, depending on the application of origami, modeling and analysis methods can be chosen. For example, for kinematic analysis a rigid bar-framework approach and tracking the null space of the compatibility matrix can be used [23] or the folded sheet can be modeled using triangular finite element plates [25]. In addition, rigid origami simulation by properly constraining every vertex has been introduced by Tachi [34]. Balkcom also applied the

mechanism theory for the kinematic analysis [82].

After reaching the mechanism to the desired folded state, to capture the structural properties of a folded shell system, a stiffness analysis can be carried out and structural modeling can be performed using a Finite Element Analysis. Depending on the application, either a bar-framework origami modeling approach or a modeling scheme using nonlinear shell elements [49] can be used at this stage. The next section includes more details on Schenk and Guest's bar framework modeling approach [23] used in current study.

3.2.1 Bar-framework approach

To investigate the effect of geometry on the global behavior of the folded sheet, Schenk and Guest [23] used a bar framework for modeling of partially folded shell structures. In their modeling, fold lines and vertices are modeled with bars and frictionless joints, respectively (Figure 3.5(a)). To stabilize each facet and to model the bending of the facets for stiffness analysis, the facets are triangulated, and diagonal members are added to each facet (Figure 3.5(a)). In this way, this model considers the bending of the facets and the effect of out-of-plane kinematics of the sheets, and therefore is not restricted to rigid origami. In a bar-framework approach the *compatibility* is to relate the nodal displacements d to the bar extensions e via compatibility matrix C as follows

$$Cd = e \tag{3.1}$$

From the relation above, the null space of the compatibility matrix provides the nodal displacements which do not extend the bars. Additionally, for rigid origami we need to prevent the bending of the facets. This can be done by adding an angular constraint to the compatibility matrix. The angular constraint F can be written in terms of the dihedral fold angle between two facets.

$$F = \sin(\rho) = \sin(\rho(P)) \tag{3.2}$$

where ρ is the dihedral fold angle between two adjoining facets; P is the nodal coordinates of two facets. By means of vector products, the angle ρ can be obtained. Hence, the change in the

dihedral angle is equal to

$$d\rho = \boldsymbol{J}\,\boldsymbol{d} = \frac{1}{\cos(\rho)}\sum \frac{\partial F}{\partial p_i}\,dp_i \tag{3.3}$$

In the above expression, $\boldsymbol{J}$ is the Jacobian of the angular constraint; dp_i are the nodal coordinates of joint i. The Jacobian of the angular constraint can be formed for each triangulated facet, and can be augmented to the compatibility matrix. Hence,

$$\bar{\boldsymbol{C}}\boldsymbol{d} = \begin{bmatrix} \boldsymbol{e} \\ d\rho \end{bmatrix} \tag{3.4}$$

in which

$$\bar{\boldsymbol{C}} = \begin{bmatrix} \boldsymbol{C} \\ \boldsymbol{J}_{facet} \end{bmatrix} \tag{3.5}$$

The null space of the above equations provides the solutions that neither extends the bars nor bends the triangulated facets, *i.e.*, a rigid origami model. Also, the number of internal infinitesimal mechanisms can be calculated from

$$m = 3j - rank(\bar{\boldsymbol{C}}) - 6 \tag{3.6}$$

For a modal analysis and also analysis of a folded shell structure subjected to external loads, we need to have a stiffness formulation. For a bar framework, the stiffness matrix is obtained as follows

$$\boldsymbol{K} = \boldsymbol{C}^T \boldsymbol{G}_{bar} \boldsymbol{C} \tag{3.7}$$

In Figure 3.5(a), K_{facet} and K_{fold} are rotational stiffness of the facets and folds, respectively. The equation above can be extended to model the bending of the facets and the fold-lines. Hence, the stiffness matrix of the system can be obtained from the following expression

$$\boldsymbol{K} = \begin{bmatrix} \boldsymbol{C} \\ \boldsymbol{J}_{facet} \\ \boldsymbol{J}_{fold} \end{bmatrix}^T \begin{bmatrix} \boldsymbol{G}_{bar} & 0 & 0 \\ 0 & \boldsymbol{G}_{facet} & 0 \\ 0 & 0 & \boldsymbol{G}_{fold} \end{bmatrix} \begin{bmatrix} \boldsymbol{C} \\ \boldsymbol{J}_{facet} \\ \boldsymbol{J}_{fold} \end{bmatrix} \tag{3.8}$$

Therefore, for the analysis of the system subjected to the external forces f, we have

$$Kd = f \qquad (3.9)$$

where d is the vector of nodal displacements.

For the stiffness analysis, and to remove the stretching of the panels, we consider a very large axial stiffness for the bars. The eigenvalue analyses have been done for a wide range of material properties by changing the ratio of the K_{facet}/K_{fold}.

3.3 Mechanical Properties of Miura-ori and Eggbox Folded Sheet Materials

3.3.1 Miura-ori pattern

The geometry of Miura-ori can be described in various ways. Schenk and Guest [10] defined the geometry using the angles between the facets and horizontal and vertical planes, whereas Wei et al. [39] established the geometry based on the dihedral angles between two adjoining facets (see Section 3.8). However, since the system has only one independent DOF, all these angles are related. The equations relating the angles defining the geometry of Miura-ori are given by Schenk and Guest [10]. The geometric parameters of Miura-ori used in current study are shown in Figure 3.5(b). From the geometry of the unit cell, we have

$$w = 2b\sin\phi \qquad \ell = 2a\frac{\cos\alpha}{\cos\phi} \qquad h = a\sin\alpha\sin\theta \qquad (3.10)$$

Also, the expression relating the angle ϕ and the fold angle θ is given by

$$\tan\phi = \cos\theta\tan\alpha \qquad (3.11)$$
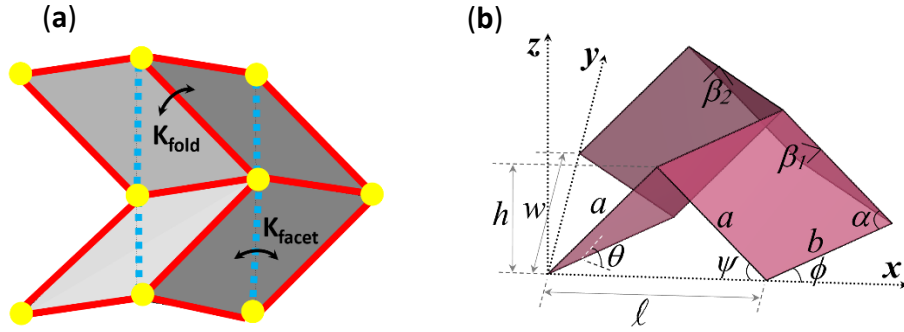
Figure 3.5: (**a**) Illustration of the bar framework approach to model folded shell structures. Fold lines and vertices are replaced with the bars and hinges, respectively. (**b**) Geometry of Miura-ori unit cell.

3.3.1.1 Stiffness analysis of Miura-based folded Materials

The results of the stiffness analysis is shown in Figure 3.6 for a Miura-ori 4x4 sheet with facet angle 60 degrees, $a=b=1$ and $\theta=55°$ for varying K_{facet}/K_{fold}. Modal shapes for the first lowest eigen-values of the sheet show that for the large values of K_{facet}/K_{fold}, the first softest eigen-mode is representing a rigid origami behavior in which the facets do not bend and the bending happens only around the fold-lines. For the smallest values of K_{facet}/K_{fold} the twisting mode is the predominant behavior of a Miura-ori sheet. Miura-ori sheet folded from a printing paper exhibits a saddle shape under bending [23]. As shown in Figure 3.6, the second softest eigen-mode for the values of K_{facet}/K_{fold} around one (*i.e.*, for the paper material) is a saddle shape which further confirms the accuracy of the analysis results.

Moreover, the results of the stiffness analysis is illustrated in Figure 3.7 for a sample stacked Miura. The geometry of the Miura-ori sheets in Figure 3.7 has been chosen according to reference [10], so that the whole system can fold and unfold freely with the same kinematics. The result of the eigenvalue analysis also show that the softest eigen-mode of the system is the rigid origami behavior of the sample stacked Miura-ori for the large values of K_{facet}/K_{fold}. This analysis further verifies the capability of the bar-framework approach for the stiffness analysis of complex SDOF system.
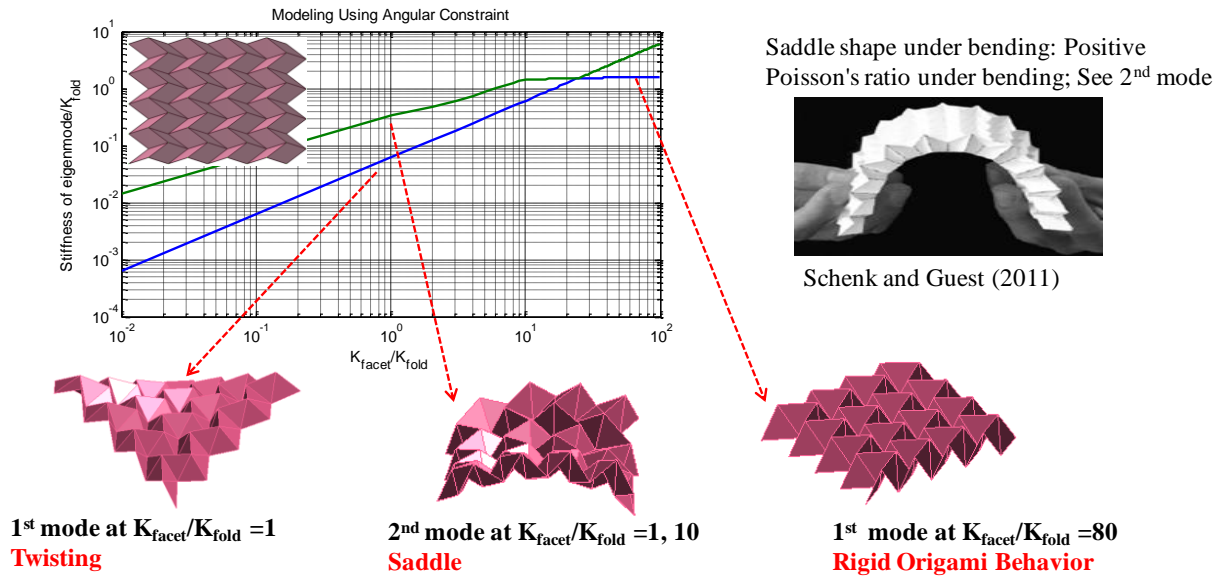
Figure 3.6: Stiffness analysis of Miura-ori pattern.
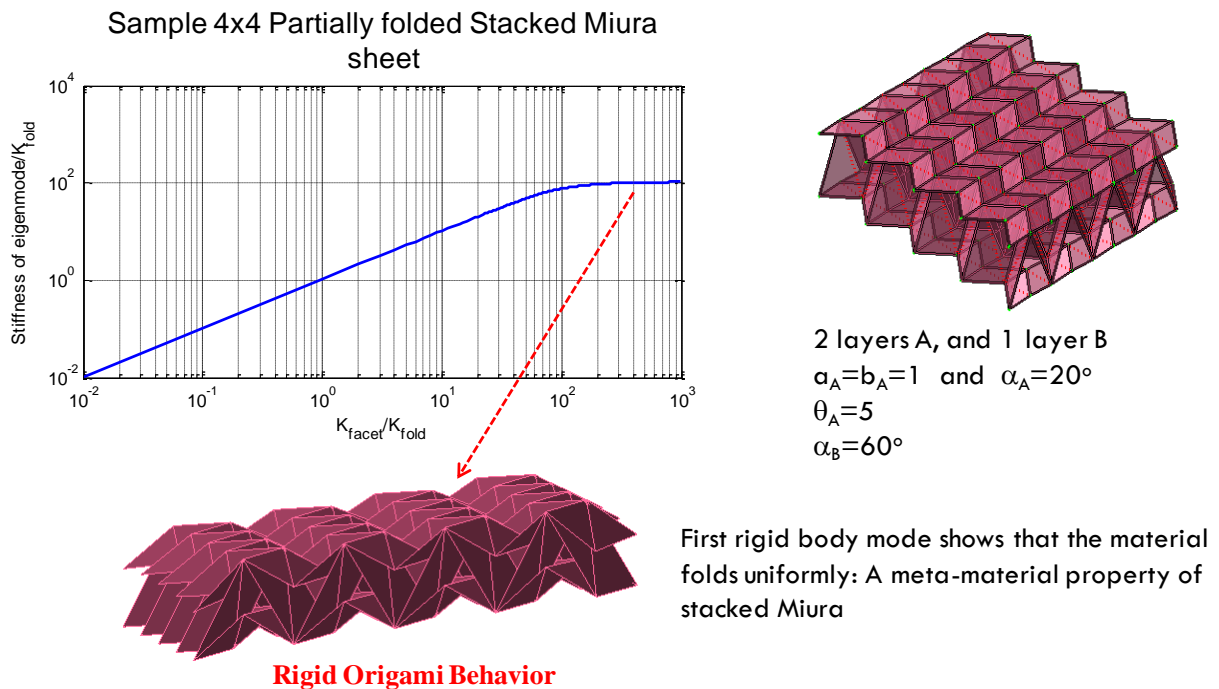
Figure 3.7: Stiffness analysis of stacked Miura-ori pattern.

3.3.1.2 In-plane response of Miura-ori sheet

In-plane Poisson's ratio of Miura-ori

The Poisson's ratio of a (m_1 by m_2) Miura-ori sheet, shown in Figure 3.1(a), is as follows (see reference [65] for details)

$$\left(\upsilon_{WL}\right)_{e-e} = -\tan^2\phi\,\frac{2m_1\lambda\cos\alpha - \cos^2\phi}{2m_1\lambda\cos\alpha + \cos^2\phi} \tag{3.12}$$

in which, $\lambda = a/b$. Therefore, for a Miura-ori sheet, for large number of rows (i.e., $m_1 \to \infty$), Poisson's ratio considering the end-to-end dimension, υ_{e-e}, approaches the corresponding value when considering the projected length of the zigzag strips, υ_z (i.e., $-\tan^2\phi$). Notice that even for a Miura-ori cell in which $m_1=1$, for some ranges of geometric parameters, the Poisson's ratio considering the end-to-end dimensions can be positive.

In-plane stiffness of Miura-ori: Kx and Ky

To obtain the in-plane rigidities, we define the unit cell based on parameters similar to those given in reference [39] (see Section 3.8). The in-plane stretching stiffness of a system in a given direction (e.g., K_x, K_y) is obtained by taking the derivative of the corresponding force with respect to the length parameter in that direction [83]. Accordingly, the in-plane stretching stiffness in the **x** direction is given by

$$K_x = \left.\frac{df_x}{d\ell}\right|_{\beta_{1_0}} = \left.\frac{df_x}{d\beta_1}\cdot\frac{d\beta_1}{d\ell}\right|_{\beta_{1_0}} \tag{3.13}$$

in which β_{1_0} is the initial dihedral angle at unreformed state.

$$K_x = \left(4k\,\frac{a(1-\xi^2)^2 + b\cos^2\alpha}{a(1-\xi^2)^{1/2}\cos\alpha\sin^2\alpha\sin\beta_1}\right)\left(\frac{8a^2\cos\alpha}{\ell^3\sqrt{1-\dfrac{4a^2\cos^2\alpha}{\ell^2}}\sqrt{\dfrac{4a^2}{\ell^2}-1}}\right) \tag{3.14}$$

where k is the rotational hinge spring constant per unit length. The second term within brackets

is missing in reference [39]. The contour plot of the ratio of K_x/k is shown in Figure 3.8 for a Miura-ori unit cell with $a=b=1$, in terms of the facet angle α and fold angle β_1.

Similarly, the stretching stiffness in the **y** direction is obtained as follows

$$K_y \equiv \frac{df_y}{dw}\bigg|_{\beta_{1_0}} = \frac{df_y}{d\beta_{1_0}} \cdot \frac{d\beta_{1_0}}{dw}\bigg|_{\beta_{1_0}} \tag{3.15}$$

$$K_y = \left(2k \frac{a(1-\xi^2)^2 + b\cos^2\alpha}{b(1-\xi^2)^2 \sin\alpha \cos(\beta_1/2)} \right) \left(\frac{2}{\sqrt{4b^2\sin^2\alpha - w^2}} \right) \tag{3.16}$$

The contour plot of the ratio of K_y/k is also shown in Figure 3.9 for a Miura-ori unit cell with $a=b=1$, in terms of the facet and fold angles α and β_1, respectively. Comparison of the two plots in Figure 3.8 (and Figure 3.9) shows that in-plane stiffness values from reference [39] are less stiff than their corresponding values obtained from the modified equations.
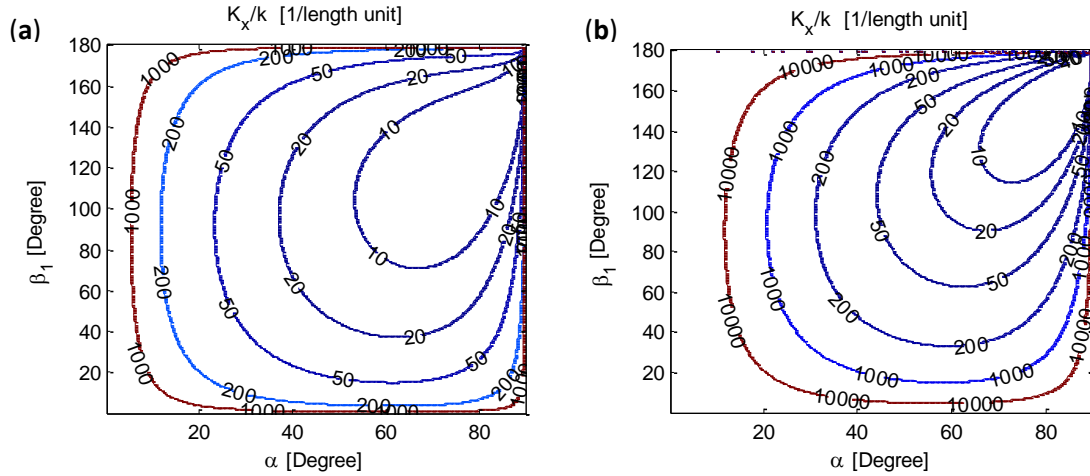
Figure 3.8: K_x/k for a Miura-ori unit cell with $a=b=1$: (**a**) Wei et al.'s equation [39]. (**b**) modified equation (present work).
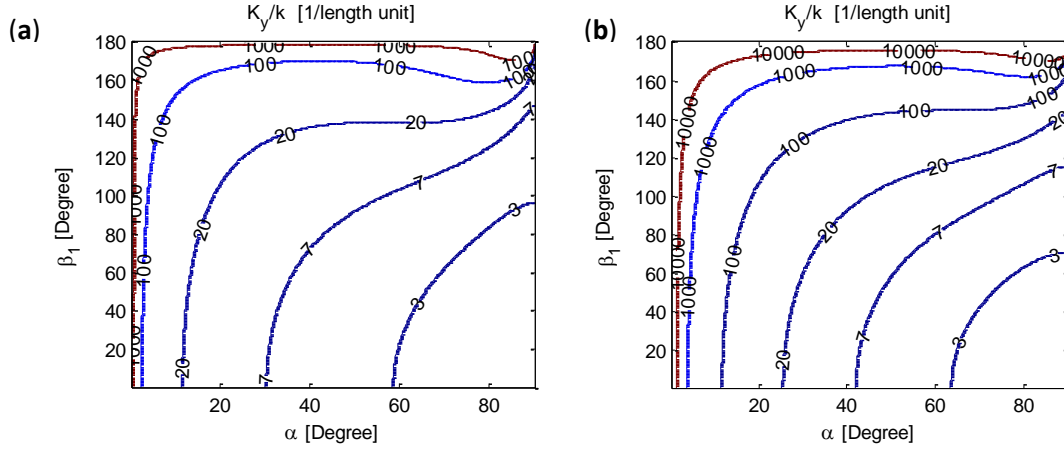
Figure 3.9: K_y/k for a Miura-ori unit cell with $a=b=1$: (**a**) Wei et al.'s equation [39]. (**b**) Modified equation (present work).

Unlike the expressions given in reference [39], the modified relations for the planar rigidities (*i.e.*, K_x/k and K_y/k) are not dimensionless, and thus K_x and K_y have dimension of the in-plane stretching stiffness, which agrees with classical references in structural analysis, e.g. [83].

3.3.2 Eggbox pattern

3.3.2.1 Geometry of Eggbox

The geometric parameters of Eggbox used in current study are shown in Figure 3.10.

From the geometry of the unit cell:

$$\ell_e = 2b_e \sin\phi_e \ , \ \ w_e = 2a_e \sin\psi_e \ , \ \ h_e = a_e \cos\psi_e + b_e \cos\phi_e \tag{3.17}$$

in which $0 \le \psi_e, \phi_e \le \alpha$. Another useful expression is given as

$$\cos\psi_e \cos\phi_e = \cos\alpha \tag{3.18}$$

where ψ_e and ϕ_e are the angles between the z'-axis and the edges a_e and b_e, respectively. Also, β_{1e} and β_{2e} are the dihedral angles between two adjacent facets along the edges a_e and b_e, respectively (Figure 3.10), and are given by

$$\beta_{1e} = 2\sin^{-1}\left(\frac{\sin\phi_e}{\sin\alpha}\right) \tag{3.19}$$

$$\beta_{2e} = 2\sin^{-1}\left(\frac{\sin\psi_e}{\sin\alpha}\right) \tag{3.20}$$
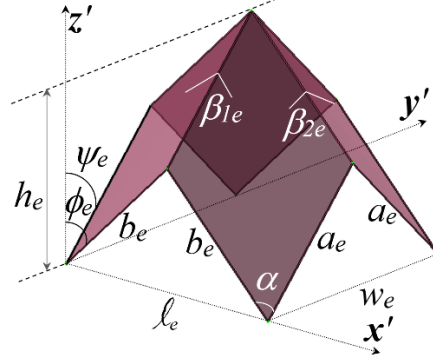
Figure 3.10: Geometry of Eggbox unit cell. The geometry of a regular Eggbox sheet can be parameterized by the geometry of a parallelogram facet (a_e, b_e and α), and one fold angle, e.g. $\phi_e \in [0,~\alpha]$ which is the angle between fold lines b_e and the z'-axis. Other important angles in the figure are angle between the fold lines a_e and the z'-axis, i.e., $\psi_e \in [0,~\alpha]$; and dihedral fold angles between parallelogram facets $\beta_{1e} \in [0,~\pi]$ and $\beta_{2e} \in [0,~\pi]$, joining along fold lines a_e and b_e, respectively.

3.3.2.2 Stiffness analysis of Eggbox sheet

The results of the stiffness analysis are presented in Figure 3.11 for an Eggbox 4x4 sheet with facet angle 60 degrees, $a_e=b_e=1$ and $\psi_e = 45°$ for a wide range of K_{facet}/K_{fold}. Modal shapes for the first lowest eigen-values of the sheet show that for large values of K_{facet}/K_{fold}, the first softest eigen-mode is representing a rigid origami behavior, which agrees with our expectation. For small values of K_{facet}/K_{fold} twisting mode is the predominant behavior of an Eggbox sheet. The Eggbox sheet folded from a printing paper exhibits a spherical shape under bending [23]. As shown in Figure 3.11, the second softest eigen-mode for the values of K_{facet}/K_{fold} around one (*i.e.*, for paper material) is a spherical shape which further confirms the accuracy of the analysis results.

Spherical shape under bending: Negative Poisson's ratio under bending; See 2nd mode

Schenk and Guest (2011)

1st mode
Twisting

2nd mode
Spherical

1st mode
Rigid Origami Behavior
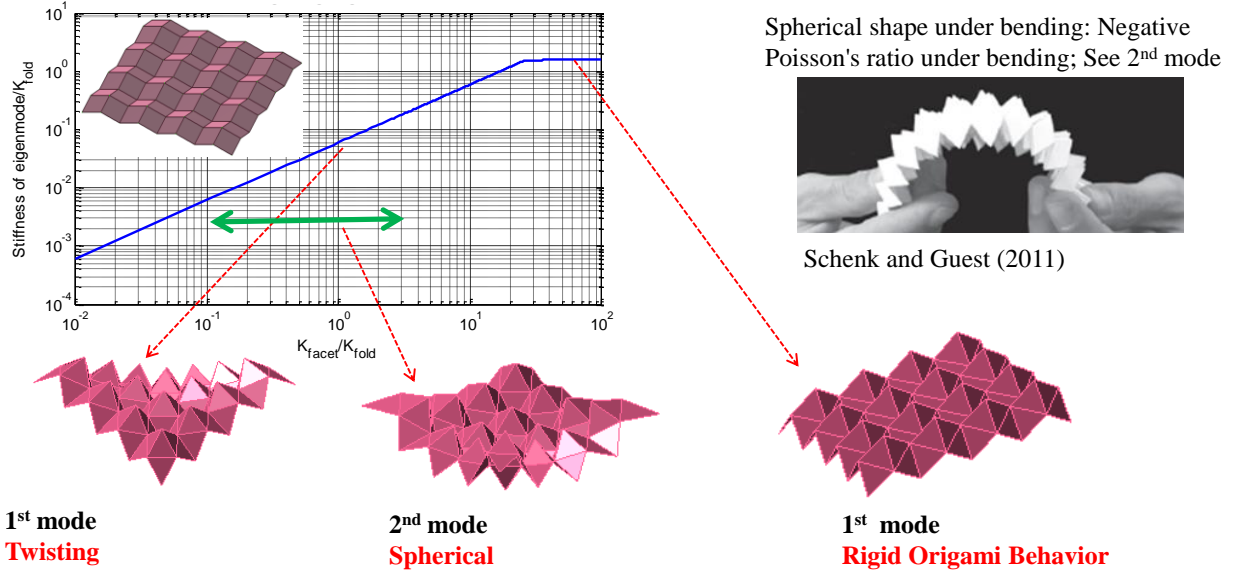
Figure 3.11: Stiffness analysis of Eggbox pattern.

3.3.2.3 In-plane response of Eggbox sheet

In-plane Poisson's ratio

In-plane Poisson's ratio of Eggbox sheet is given by

$$\upsilon_{w_e \ell_e} = \frac{\varepsilon_{\ell_e}}{\varepsilon_{w_e}} = -\frac{w_e}{\ell_e} \frac{d\ell_e}{dw_e} = \frac{\tan^2 \psi_e}{\tan^2 \phi_e} \tag{3.21}$$

From the above expression, the Poisson's ratio of Eggbox is always positive, $i.e.\, \upsilon_{w_e \ell_e} \in [0, \infty)$, which was also quantified in the literature based on the angle ψ_e and the facet acute angle α [23]. However, knowing that the Poisson's ratio is only a function of the angles between the z'-axis and the edges a_e and b_e is insightful for creating foldable materials containing layers of Eggbox sheets with different geometries as presented in Section 3.7. The in-plane Poisson's ratio of Eggbox versus ψ_e for different values of the acute angle α is presented in Figure 3.15(b).

In-plane stiffness: $K_{x'}$ and $K_{y'}$

Considering that the facets are rigid and are bonded via elastic torsional hinges at fold lines, we obtain the in-plane rigidities of Eggbox unit cell in the **x'** and **y'** directions (see Section 3.8) as follows

$$K_{x'} = \frac{4k}{\sin\alpha\cos(\beta_{1e}/2)} \left(\frac{a_e(1-\xi_{1e}{}^2)^2 + b_e\cos^2\alpha}{b_e(1-\xi_{1e}{}^2)^2} \right) \left(\frac{1}{\sqrt{4b_e{}^2\sin^2\alpha - \ell_e{}^2}} \right) \tag{3.22}$$

$$K_{y'} = \frac{4k}{\sin\alpha\cos(\beta_{2e}/2)} \left(\frac{a_e\cos^2\alpha + b_e(1-\xi_{2e}{}^2)^2}{a_e(1-\xi_{2e}{}^2)^2} \right) \left(\frac{1}{\sqrt{4a_e{}^2\sin^2\alpha - w_e{}^2}} \right) \tag{3.23}$$

in which $\xi_{1e} = \sin\alpha\sin(\beta_{1e}/2)$ and $\xi_{2e} = \sin\alpha\sin(\beta_{2e}/2)$.

For the case of $a = a_e$, $b = b_e$, $\beta_1 = \beta_{1e}$ and $w = \ell_e$, shown in Figure 3.3(a), from Equations (3.16) and (3.22), the in-plane stiffness of Miura-ori cell in the **y** direction (K_y), is equal to the in-plane stiffness of Eggbox cell in the **x'** direction ($K_{x'}$). The contour plot of the stiffness ratio in the **x'** direction ($K_{x'}/k$) is shown in Figure 3.12 for an Eggbox unit cell with $a_e = b_e = 1$, in terms of the facet angle α and fold angle β_{1e}.
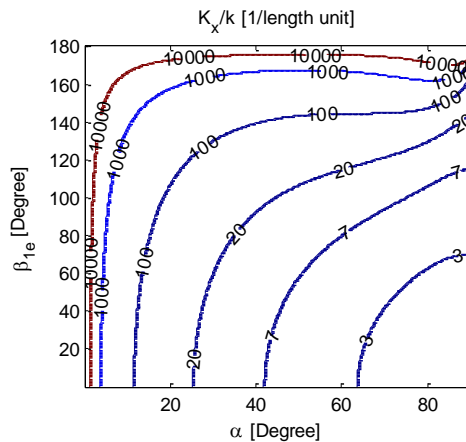
Figure 3.12: In-plane stretching stiffness $K_{x'}/k$ of Eggbox unit cell with $a=b=1$.

3.4   A Framework to Obtain Poisson's Ratio Computationally

Instantaneous Poisson's ratio of Miura-ori is computed numerically in this section. A Miura-ori unit cell is modeled using the bar framework approach, and the Poisson's ratio is calculated for changing α and θ. For the analysis under the external applied loads, we need to remove the rigid body motions of the system while keeping the planar motion by applying appropriate constraints. The simulation set up is illustrated in Figure 3.13(a) in which yellow nodes are constrained to remain in the horizontal (xy) plane (*i.e.*, only displacements in the z direction are constrained, and the system moves freely in the xy plane), and the blue node is constrained for all displacements. External force is also applied in the x direction as shown in Figure 3.13(a). Moreover, to ensure the rigid origami behavior for obtaining the planar Poisson's ratio, the value of K_{facet}/K_{fold} must be large enough, and the axial stiffness of the bars, K_{bar}, is required to be sufficiently large to prevent the extension of the bars. For this example, we choose $K_{bar}=10^9$ and $K_{facet}/K_{fold}=10^3$ - eigen-value analysis of the system confirms that using these values, the rigid origami behavior is obtained for the Miura-ori unit cell considered in this section (Figure 3.14(a)). Figure 3.15(a) shows Poisson's ratio obtained from the simulation matches well with the analytical model.

A similar approach to the one described for Miura-ori has been used to obtain the instantaneous Poisson's ratio of Eggbox. The simulation set up is illustrated in Figure 3.13(b) in which yellow nodes are constrained to move freely in the horizontal (xy) plane (*i.e.*, only displacements in the z direction are constrained), and the blue node is constrained for x and y displacements, and moves freely in z direction. External force is also applied in the x direction as shown in Figure 3.13(b). The mode shapes showing the rigid origami behavior are shown in Figure 3.14(b). Figure 3.15(b) shows that Poisson's ratio obtained from the simulation matches reasonably well the analytical model.
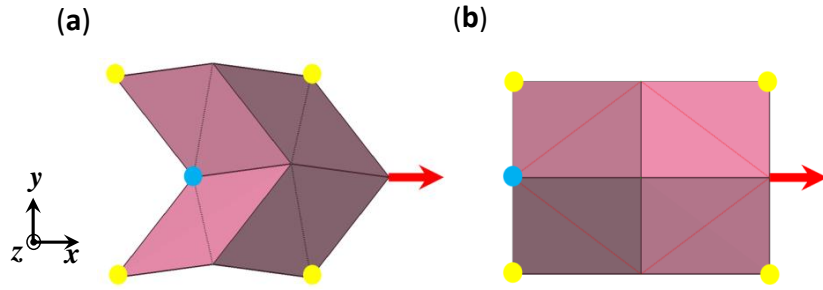
Figure 3.13: Simulation set up to compute Poisson's ratio numerically. (**a**) Miura-ori. (**b**) Eggbox.
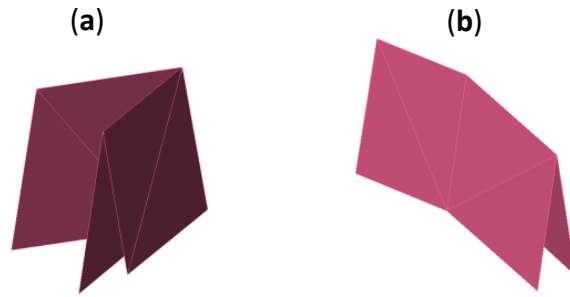
Figure 3.14: First mode illustrating rigid origami behavior: (**a**) Miura-ori. (**b**) Eggbox unit cell.
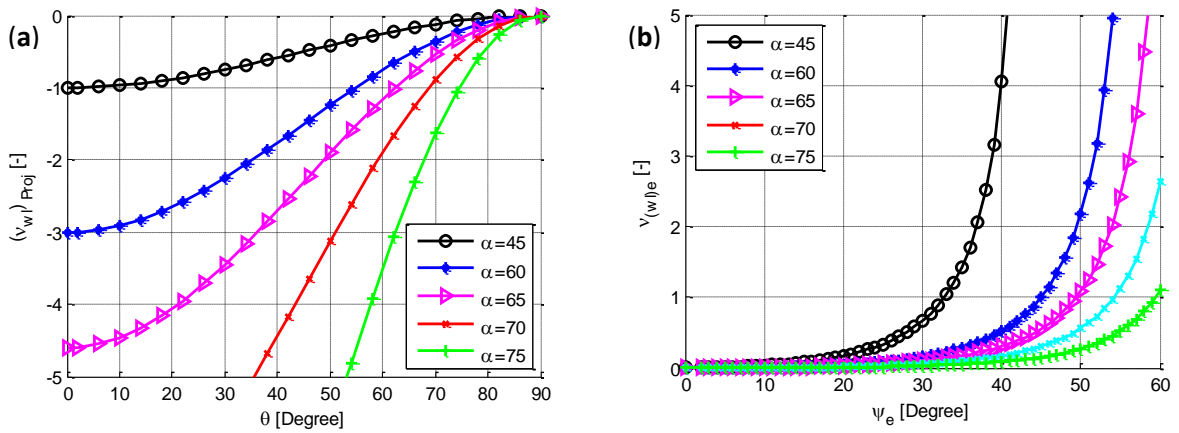
Figure 3.15: Poisson's ratio computed numerically: (**a**) Miura-ori. (**b**) Eggbox unit cell.

3.5   Metamaterials Composed of Miura-ori and Eggbox Cells

From expression 24, the Poisson's ratio of a regular Eggbox sheet is a function of the angles ϕ_e

and ψ_e (see Figure 3.10). Layers of Eggbox sheets with the same Poisson's ratio can be attached along the joining fold lines resulting in a bi-directionally flat-foldable material (Figure 3.4). A similar tubular material composed of Miura-based tubes with identical parallelogram facets has been described by Tachi [62]. The cross section of the tube described by Tachi has identical edges (Figure 3.16(a)). In general, Miura-ori tube is a special case of stacking of Miura-ori sheets [10] in which the angle θ has different signs for the sheets A and B bonded together along the joining fold lines, i.e. $\theta_A \in [-\pi/2, 0]$ and $\theta_B \in [0, \pi/2]$. Meeting the stacking conditions results in a tube cell with the kite-shape cross section shown in Figure 3.16(b) which is generally flat-foldable in one direction.
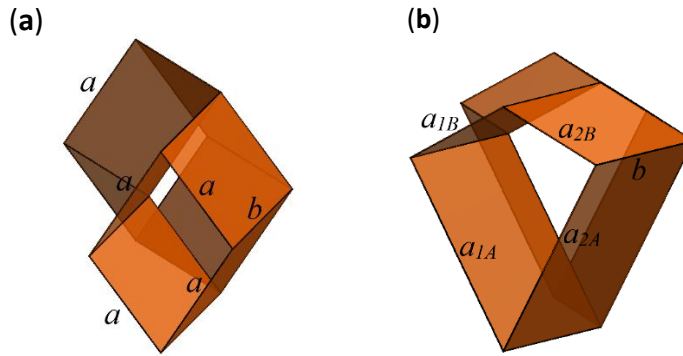
Figure 3.16: (**a**) Tube cell with rhombus cross section. (**b**) General tube cell geometry, for the kite-shape cross section, $a_{1A} = a_{2A}$ and $a_{1B} = a_{2B}$.

For two layers of Miura-ori cells (i.e., layers A and B), from the conditions for stacking of Miura-ori [10] we have

$$(a_{1A} + a_{2A})\cos\psi_A = (a_{1B} + a_{2B})\cos\psi_B \tag{3.24}$$

where a_{1A}, a_{2A}, a_{1B} and a_{2B} are shown in Figure 3.16(b). Also, from the geometry of Miura cell we have

$$\cos\psi = \frac{\cos\alpha}{\cos\phi} \tag{3.25}$$

Combining two above equations results in

$$\left(a_{1A} + a_{2A} \right) \cos \alpha_A = \left(a_{1B} + a_{2B} \right) \cos \alpha_B \tag{3.26}$$

From the above expression, for the special case of $\alpha_A = \alpha_B$, we need to have

$$a_{1A} + a_{2A} = a_{1B} + a_{2B} \tag{3.27}$$

To meet the above equation, we can have

$$a_{1A} = a_{2B} \text{ and } a_{2A} = a_{1B} \tag{3.28}$$

Hence, for the special case of identical acute angles at the top and bottom cells (i.e., $\alpha_A = \alpha_B$), we can have bi-directionally flat-foldable tubes with parallelogram cross sections (Figure 3.17). In the following, we describe tubular folded materials composed of tubes with parallelogram cross sections. As shown in Figure 3.18, with special alignments of tube cells and tessellation and/or combinations of tessellations of corresponding units, we can produce various cellular metamaterials. Tessellation of the alignment of the cells, shown in Figure 3.18(a), can result in materials with either Miura or Eggbox surfaces (see Figure 3.19). Figure 3.18(e) presents a cellular metamaterial with Miura-ori and Eggbox surfaces parallel to the *xz* and *yz* planes, respectively. Therefore, the material is auxetic in the planes parallel to *xz* plane, and expanding the material in the *z* direction results in the expansion and contraction of the material in the *x* and *y* directions, respectively.

3.6   Non-developable Zigzag-base Sheets and Zigzag-base Tubes

In this Section, we use the concept of the Poisson's ratio of a zigzag strip introduced in reference [65] (see Sections 4.2 of the current dissertation), to design non-developable zigzag-base patterns (see Figure 3.20) as well as load-carrying zigzag-base tubes (see Figure 3.21 and Figure 3.22). To construct these structures, zigzag strips with identical kinematics are connected. Figure 3.20 presents non-developable zigzag-base patterns. The patterns shown in the figure are designed so that, in their fully deployed configurations, the Miura-ori rows in the middle (dark pink) are flat, while the outer rows remain non-flat. Using the kinematics of a zigzag strip, we can design

various configurations of non-developable zigzag-base patterns in which the geometry can differ from one zigzag to the other one and even from one V-shape (see Sections 4.2) to the other one while keeping the kinematics identical.

Figure 3.21 and Figure 3.22 show load-carrying zigzag-base tubes. The structures are flat-foldable in one direction and can carry load in their fully deployed configurations.

3.7   Concluding Remarks

Eggbox is a non-developable folded sheet. The sheet is a one-DOF mechanism system and bi-directionally flat-foldable material. Its structure can appear into Miura-inspired tubular materials when assembled in a special way. A sample novel bi-directionally flat-foldable material is shown in Figure 3.4(b) which contains layers of two different scales Eggbox sheets. Unlike Miura-ori, there is limited research available in the literature on Eggbox folded sheet.
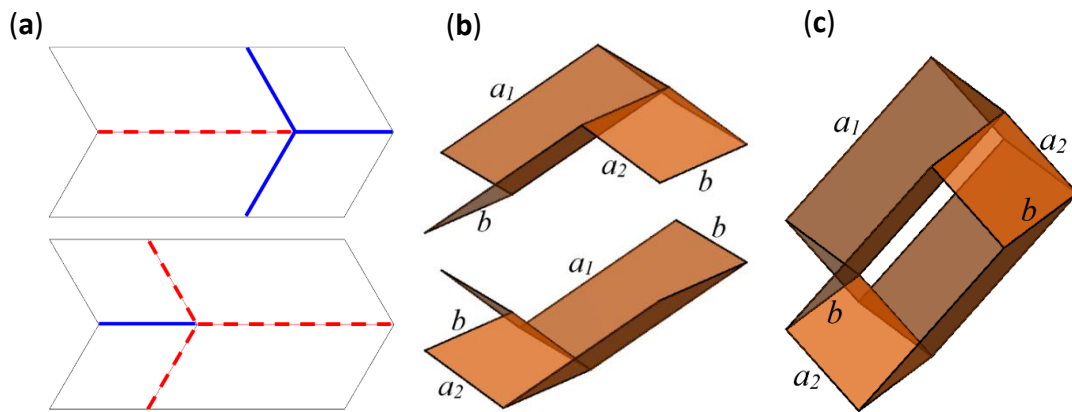
Figure 3.17: Miura-ori based tube with parallelogram cross section. (**a**) Unfolded Miura-ori unit cells with mountain (blue continuous lines) and valley (red dashed lines) assignments. (**b**) Partially folded Miura-ori cells constructing the top and bottom of the tube cell. (**c**) Tube cell with parallelogram cross section.

In this study, the key mechanical properties of Miura-ori and Eggbox are reviewed and studied both analytically and numerically. Specifically, the geometric parameters of Miura-ori and Eggbox are explained in relation to a tube cell with rhombus cross section (see Figure 3.3) which can be decomposed to Miura-ori and Eggbox cells. In this way, mechanical properties of Eggbox

and Miura-ori can be compared appropriately. Furthermore, employing bar-framework numerical approach, a procedure is described to obtain the Poisson's ratio of both Miura-ori and Eggbox. The process can be used to obtain the Poisson's ratio of similar, but more complex sheets for which the analytical models are not available. Verifying the analytical models for Poisson's ratio numerically, as explained in this work, somehow shows the capability of pin-jointed bar framework approach for the analysis of folded shell structures subjected to external loads.

Additionally, Miura-based tube with parallelogram cross section is explained (notice that in the tube shown in Figure 3.17, parallelogram facets of Miura-ori cells are not identical), and the geometry of one-DOF mechanism cellular metamaterials containing tubes with parallelogram cross sections is described. The proposed structures are purely geometric. Hence, they can be applied in a wide range of length-scale from microstructure of materials to deployable structures. Particularly, possessing one DOF is advantageous to provide low-energy, efficient and controllable actuation. Hence, making them appropriate as the bases to construct adaptive structures and materials.

The conditions for stacking Miura-ori sheets with different geometries are described in reference [10]. However, attaching Eggbox sheets with different geometries, while preserving the capability of folding and unfolding is not described in the literature. Inspired by tubes with parallelogram cross sections (Figure 3.17) as well as the fact that the Poisson's ratio of Eggbox is only a function of the angles between the edges a_e and b_e and the z'-axis (see Equation (3.21)), we can design the structure of customizable cellular materials with one-DOF mechanism containing layers of Eggbox sheets (a sample is shown in Figure 3.23). The material shown in the figure contains three layers of Eggbox sheets which are attached along the joining fold-lines. The sheets have different geometries, but the same Poisson's ratios. Hence, the entire system can fold and unfold freely.
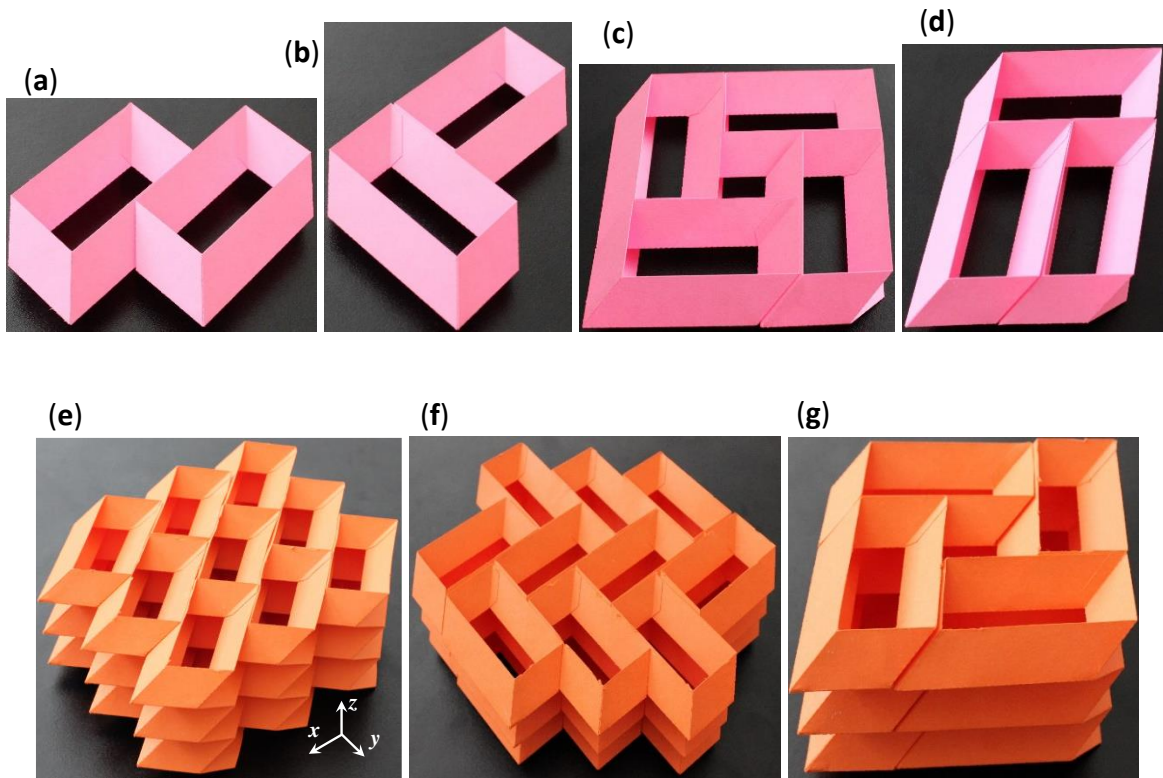
Figure 3.18: (**a-d**) Sample alignments of tube cells with parallelogram cross sections, and sample one-DOF mechanism materials made from them. (**e-g**) Tessellations and/or combinations of these units results in various configurations of materials.
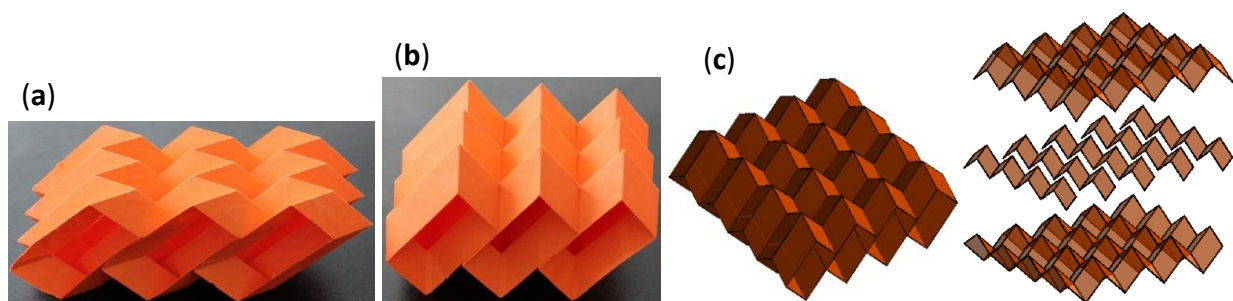
Figure 3.19: (**a**) Material with Miura surfaces at the top and bottom. (**b**) Material with Eggbox surfaces at the top and bottom. (**c**) Bi-directionally flat-foldable tubular materials with parallelogram cross sections decomposed to Eggbox sheets.

Figure 3.20: Non-developable zigzag-base patterns constructed from Miura-ori cells with identical kinematics and different heights of the unit cells (the rule is similar to that used in the stacking, but the cells possessing different heights are connected side-by-side instead of stacking).
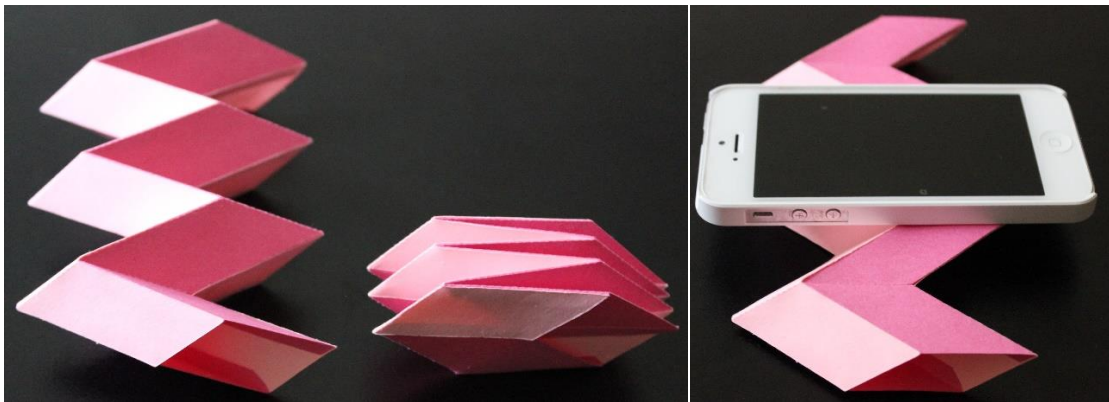
Figure 3.21: Modified zigzag-base tubes constructed from zigzag strips with identical kinematics and different heights (in their semi-folded states) and various acute angles of parallelograms. The presented tubes are flat-foldable in one direction, and they provide a flat and load carrying surface in their fully deployed configurations.

Figure 3.22: A side-by-side assembly of the tubes shown in the figure above. The structure is flat-foldable in one direction and can carry vertical loads in its deployed configuration.
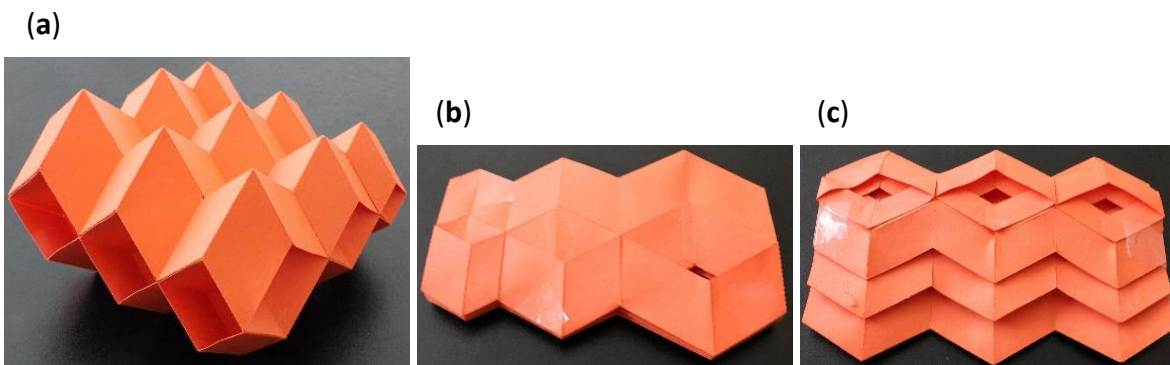
Figure 3.23: (**a**) Sample graded bi-directionally flat-foldable cellular material with one-DOF mechanism inspired by Miura-based tube with parallelogram cross section. The sample material includes 3 layers of Eggbox with the same Poisson's ratio bonded along joining fold lines. (**b, c**) Fully folded states in 2 orthogonal directions.

3.8 Supplementary Materials: In-plane Stiffness
3.8.1 Miura-ori

The geometry of Miura-ori unit cell (Figure 3.5(b)) in reference [22] is parametrized based on the dihedral fold angles between facets as follows

$$\ell = 2a\zeta \qquad w = 2b\xi \qquad h = a\zeta \tan\alpha \cos(\beta_1/2) \tag{3.29}$$

in which,

$$\xi = \sin\alpha \sin(\beta_1/2) \qquad \text{and} \qquad \zeta = \cos\alpha \left(1-\xi^2\right)^{-1/2} \tag{3.30}$$

By substituting ℓ from Equation (3.29) in Equation (3.14) and for a special case of Miura-ori unit cell with $a=b=l_{eq}$ we have

$$K_x = \frac{4k}{\ell_{eq}} \frac{(1-\xi_0^2)^3 + \cos^2\alpha(1-\xi_0^2)}{\xi_0 \cos^2\alpha \sin^3\alpha \sin\beta_{1_0} \cos(\beta_{1_0}/2)} \tag{3.31}$$

By substituting w from Equation (3.29) in equation (3.16) and for a special case of Miura-ori unit cell with $a=b=l_{eq}$ we have

$$K_y = \frac{2k}{\ell_{eq}} \frac{(1-\xi_0^2)^2 + \cos^2\alpha}{(1-\xi_0^2)^2 \sin^2\alpha \cos^2(\beta_{1_0}/2)} \tag{3.32}$$

3.8.2 Eggbox

Potential energy of an Eggbox unit cell subjected to a force in the x' direction can also be calculated from the following equation

$$H = U + \Omega \tag{3.33}$$

in which, U and Ω are elastic energy and potential of the applied load, respectively and can be calculated as

$$U = k\left(a_e(\beta_{1e} - \beta_{1e_0})^2 + b_e(\beta_{2e} - \beta_{2e_0})^2\right) \tag{3.34}$$

$$\Omega = - \int_{\beta_{1e_0}}^{\beta_{1e}} f_{x'} \frac{d\ell_e}{d\beta_{1e}'} d\beta_{1e}'$$

(3.35)

where β_{2e_0} and β_{1e_0} are the initial dihedral angles at unreformed states. Setting the condition $\partial H / \partial \beta_{1e} = 0$, the external force at equilibrium $f_{x'}$ can be obtained from

$$f_{x'} = \frac{dU / d\beta_{1e}}{d\ell_e / d\beta_{1e}}$$

(3.36)

where

$$dU / d\beta_{1e} = 2k \left(a_e (\beta_{1e} - \beta_{1e_0}) + b_e (\beta_{2e} - \beta_{2e_0}) \frac{-\cos\alpha}{1 - \sin^2\alpha \sin^2(\beta_{1e} / 2)} \right)$$

(3.37)

$$d\ell_e / d\beta_{1e} = b_e \sin\alpha \cos(\beta_{1e} / 2)$$

(3.38)

Substituting the two above equations into $f_{x'}$, we have

$$f_{x'} = \frac{2k}{\sin\alpha} \left(\frac{\frac{a_e}{b_e}(\beta_{1e} - \beta_{1e_0}) + (\beta_{2e} - \beta_{2e_0}) \frac{-\cos\alpha}{1 - \sin^2\alpha \sin^2(\beta_{1e} / 2)}}{\cos(\beta_{1e} / 2)} \right)$$

(3.39)

Also, $K_{x'}$ can be obtained from the following equation

$$K_{x'}(\alpha, \beta_{1e_0}) = \frac{df_{x'}}{d\ell_e} \bigg|_{\beta_{1e_0}} = \frac{df_{x'}}{d\beta_{1e}} \cdot \frac{d\beta_{1e}}{d\ell_e} \bigg|_{\beta_{1e_0}}$$

(3.40)

where

$$\frac{df_{x'}}{d\beta_{1e_0}} \bigg|_{\beta_{1e_0}} = \frac{2k}{\sin\alpha} \cdot \frac{1}{\cos(\beta_{1e_0} / 2)} \left(\frac{b_e \cos^2\alpha + a_e (1 - \sin^2\alpha \sin^2(\beta_{1e_0} / 2))^2}{b_e (1 - \sin^2\alpha \sin^2(\beta_{1e_0} / 2))^2} \right)$$

(3.41)

$$\frac{d\beta_{1e}}{d\ell_e} = \frac{2}{\sqrt{4b_e^2 \sin^2\alpha - \ell_e^2}}$$

(3.42)

Substituting equations (3.41) and (3.42) into (3.40) we have

$$K_{x'} = \frac{4k}{\sin\alpha\cos(\beta_{1e}/2)} \left(\frac{b_e\cos^2\alpha + a_e(1-\sin^2\alpha\sin^2(\beta_{1e}/2))^2}{b_e(1-\sin^2\alpha\sin^2(\beta_{1e}/2))^2} \right) \left(\frac{1}{\sqrt{4b_e^2\sin^2\alpha - \ell_e^2}} \right) \quad (3.43)$$

Figure 3.24 shows that increasing the fold length b_e, *i.e.* the fold in the $\boldsymbol{x'}$ direction, makes the unit cell softer in the $\boldsymbol{x'}$ direction. Whereas, increasing the fold length a_e, increases the ratio of K_x/k.
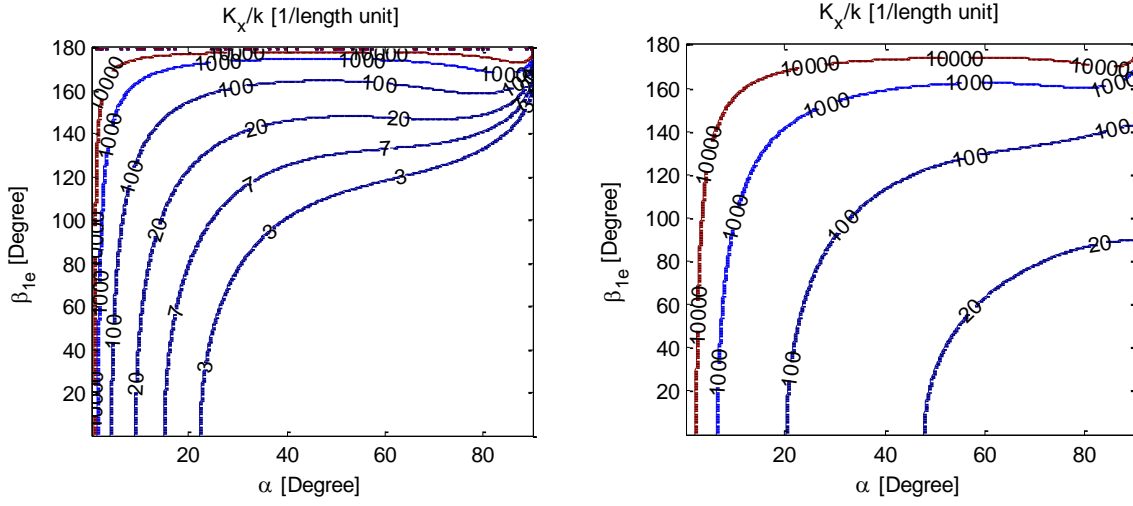
Figure 3.24: Effect of fold lengths on in-plane stretching stiffness K_x/k of Eggbox unit cell: Left ($a_e=1$ and $b_e=5$); Right ($a_e=5$ and $b_e=1$).

Following similar process to the $\boldsymbol{x'}$ direction, for the $\boldsymbol{y'}$ direction we have

$$K_{y'} = \frac{4k}{\sin\alpha\cos(\beta_{2e}/2)} \left(\frac{a_e\cos^2\alpha + b_e(1-\sin^2\alpha\sin^2(\beta_{2e}/2))^2}{a_e(1-\sin^2\alpha\sin^2(\beta_{2e}/2))^2} \right) \left(\frac{1}{\sqrt{4a_e^2\sin^2\alpha - w_e^2}} \right) \quad (3.44)$$

Equation (3.44) is similar to Equation (3.43) where $a_e, b_e, \beta_{1e}, \ell_e$ in Equation (3.43) are substituted with $b_e, a_e, \beta_{2e}, w_e$, respectively.

4 Unravelling Metamaterial Properties in Zigzag-base Folded Sheets

This chapter is adapted from an article authored by Eidini and Paulino, published in *Science Advances* [65].

Abstract

Creating complex spatial objects from a flat sheet of material using origami folding techniques has attracted attention in science and engineering. In the present work, we use the geometric properties of partially folded zigzag strips to better describe the kinematics of known zigzag/herringbone-base folded sheet metamaterials such as Miura-ori. Inspired by the kinematics of a one-degree of freedom zigzag strip, we introduce a class of cellular folded mechanical metamaterials comprising different scales of zigzag strips. This class of patterns combines origami folding techniques with kirigami. Using analytical and numerical models, we study the key mechanical properties of the folded materials. We show that our class of patterns, by expanding on the design space of Miura-ori, is appropriate for a wide range of applications from mechanical metamaterials to deployable structures at small and large scales. We further show that, depending on the geometry, these materials exhibit either negative or positive in-plane Poisson's ratios. By introducing a class of zigzag-base materials in the current study, we unify the concept of in-plane Poisson's ratio for similar materials in the literature and extend it to the class of zigzag-base folded sheet materials.

4.1 Introduction

Origami, the art of paper folding, has been a substantial source of inspiration for innovative design of mechanical metamaterials [10, 50, 39, 40, 62], for which the material properties arise from their geometry and structural layout. Kirigami is the art of paper cutting and, for engineering applications, it has been used as combination of origami with cutting patterns to fabricate complex microstructures through micro-assembly [84], as well as to create 3D core structures [64, 85, 86, 87]. Furthermore, rigid origami is a subset of origami structures where rigid panels (facets) are linked through perfect hinges leading to an entirely geometric mechanism. The mathematical theory of rigid origami has been studied by various researchers [30, 31, 32, 35, 34]. Based on rigid origami behavior of folding patterns, recent research [10, 39] has shown that in Miura-ori, metamaterial properties arise due to their folding geometry. Miura-ori is a classic origami folding pattern and its main constituents are parallelogram facets which are connected along fold lines. Morphology and/or mechanism similar to that of Miura-ori naturally arises in insect wings [69], tree leaves [70] and embryonic intestine [75, 76]. Moreover, it has been reported that a self-organized wrinkling pattern of a planar stiff thin elastic film connected to a soft substrate subjected to biaxial compression, i.e. a herringbone pattern, is similar to the Miura-ori [71, 72, 73]; and herringbone pattern corresponds to the minimum energy configuration [74]. Applications of the Miura-ori pattern range from folding of maps [48] to the technologies such as deployable solar panels [24], foldcore sandwich panels [16, 68] and metamaterials [10, 50, 39]. The patterns introduced in this work are herringbone-base patterns, which are combined with cuts, and shown to possess the remarkable properties of the Miura-ori pattern.

Motivated by outstanding properties and broad range of applications of the Miura-ori, the present study starts with raising a question: Can we design patterns aiming at both preserving the remarkable properties of the Miura-ori and expanding upon its design space? In this regard, upon closer inspection of the Miura-ori, we associate its kinematics to that of a one-degree of freedom (DOF) zigzag strip, and we present a technique to create zigzag-base mechanical metamaterials including various scales of zigzag strips. Through this study, we answer the question affirmatively.

An important material property in the present work is the in-plane Poisson's ratio. It is defined as the negative ratio of elastic extensional strain in the direction normal to the applied load, to the axial extensional strain in the direction of the applied load. Most commonly, when a material is stretched in a given direction it tends to get narrower in the directions perpendicular to the applied load. However, when stretched, materials with negative in-plane Poisson's ratio or auxetic materials expand in the direction perpendicular to the applied load. The out-of-plane bending Poisson's ratio is defined as the negative ratio of curvatures in two perpendicular directions. Under bending, anticlastic (saddle-shape) and synclastic (spherical-shape) curvatures are observed in materials with positive and negative bending Poisson's ratios, respectively [88, 23]. Based on the theory of elasticity, the Poisson's ratio for a thermodynamically stable isotropic linear elastic material is bounded between -1 to 0.5 [89]. Contrary to isotropic solids, the value of Poisson's ratio is unrestricted in an anisotropic elastic material $(-\infty < \upsilon < \infty)$ [90]. Folded sheets are anisotropic materials in which the deformation happens due to folding and unfolding. Thus, in folded sheet materials (for instance in most ranges within geometric parameters of the Miura-ori folding pattern), the Poisson's ratio can assume values outside the bound for isotropic materials [10, 39].

4.2   Kinematics of a Folded One-DOF Zigzag Strip

In this section, we look closely at the kinematics of Miura-ori as a zigzag-base folding pattern, which provides inspiration to create a class of mechanical metamaterials. A regular Miura-ori sheet contains zigzag strips of parallelogram facets, in which each unit cell can be decomposed into two *V*-shapes (Figure 4.1(a)). Each *V*-shape includes 2 rigid parallelogram facets connected via a hinge along the joining ridges as shown in Figure 4.1(b). We show that the kinematics of a properly constrained *V*-shape, as described in the following, is a function of an angle in the horizontal *xy*-plane. The constraints on the *V*-shape are applied to simulate similar conditions to those of the *V*-shapes in Miura-ori sheet, i.e., to create a one-DOF planar mechanism. Hence, to remove the rigid body motions associated with the translational and rotational DOFs, we constrain all translational DOFs of the point *A* and we assume that the edges *AB* and *BC* of the facets move in the *xy*-plane, and the projected length of the edge *AD* in the *xy*-plane remains along the *x*-axis (i.e., point *D* moves in the *xz*-plane). With this set up, the *V*-shape has only one

planar DOF. The expressions defining the geometry of the V-shape are given by

$$\ell_v = a\frac{\cos\alpha}{\cos\phi} \qquad\qquad w_v = 2b\sin\phi \qquad\qquad (4.1)$$

where, ℓ_v is the projected length of the edges a in the **xy**-plane and in the **x** direction; w_v is the width of the semi-folded V-shape in the **xy**-plane and along the **y** direction; ϕ is an angle in the **xy**-plane between the edge b and the **x**-axis. The in-plane Poisson's ratio of the system is given by

$$\left(\upsilon_{w\ell}\right)_V = -\frac{\varepsilon_{\ell_v}}{\varepsilon_{w_v}} = -\frac{d\ell_v/\ell_v}{dw_v/w_v} = -\tan^2\phi \qquad\qquad (4.2)$$

The above expression shows that the kinematics of a V-shape is only a function of the angle ϕ. In particular, it shows that in a unit cell containing two V-shapes arranged side-by-side in the crease pattern, we can scale down the length b of the parallelogram facets to $1/n$ that of the other joining V-shape (n is a positive integer), while preserving the capability of folding and unfolding. Using this insight in our current research, we created a class of zigzag-base metamaterials in which the unit cell includes two different scales of V-shapes possessing the same ϕ angles (Figure 4.1(c)). For instance, for the zigzag strips shown in Figure 4.1(c), the value of n is equal to 2. For the case of $n=2$, from both the numerical model and the geometry, the unit cell has only one planar mechanism (see Sections 4.7.2 and 4.7.6.1), i.e., the geometry of the unit cell constrains the V-shapes properly to yield one-DOF planar mechanism. Therefore, the condition for which we have obtained the kinematics of the V-shape is met.

4.3   BCH$_n$ Zigzag-base Patterns

The *Basic unit Cell with Hole* (BCH$_n$) of the patterns introduced in Figure 4.1(c) is parametrized in Figure 4.2(a). The unit cell includes 2 large and $2n$ small parallelogram rigid panels joined via fold lines. For example, for the unit cell shown in Figure 4.2(a), n is equal to 2. Although theoretically possible, large values of n might not be practical. For a large n, a zigzag strip of small parallelograms approaches a narrow strip. In current research, we use only $n=2, 3$ in the BCH patterns with an emphasis placed on BCH$_2$. We can define the unit cell by the geometry of

the parallelogram facets with sides a and b and acute angle $\alpha \in [0, \pi/2]$, and angle $\phi \in [0, \alpha]$, which is half the angle between the edges b_1 in the **xy**-plane. The expressions defining the geometry of the BCH_n are given by

$$w = 2b\sin\phi \qquad \ell = 2a\frac{\cos\alpha}{\cos\phi} \qquad h = a\sin\alpha\sin\theta \qquad b_1 = b/n \qquad (4.3)$$

(a) **(b)** **(c)**
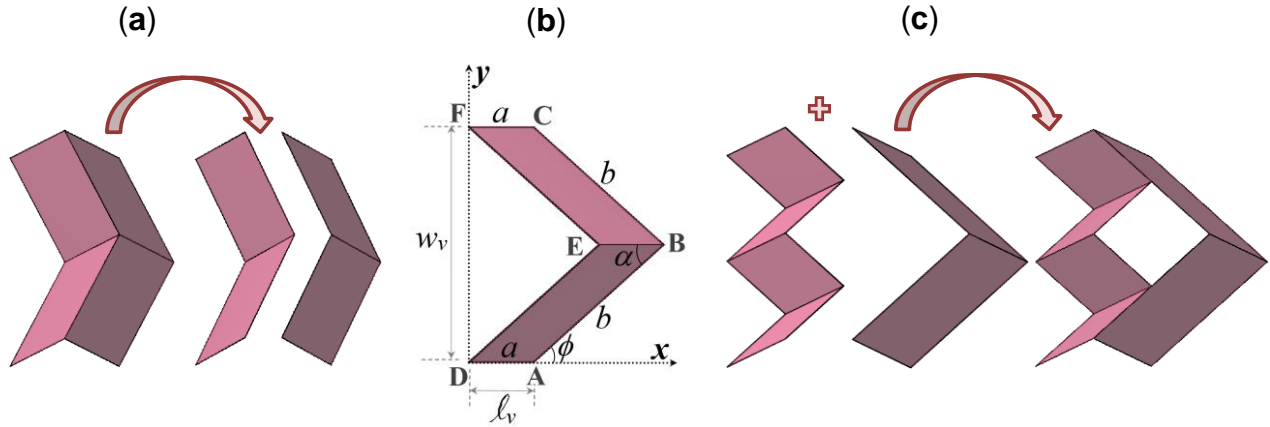
Figure 4.1: From Miura-ori to zigzag-base foldable metamaterials possessing different scales of zigzag strips. (**a**) A Miura-ori unit cell contains two *V*-shapes aligned side-by-side forming one concave valley and three convex mountain folds (or vice versa, if the unit cell is viewed from the opposite side). (**b**) Top view of a *V*-shape fold including two identical parallelogram facets connected along the ridges with length a. Its geometry can be defined by the facet parameters a, b, α and the angle $\phi \in [0, \alpha]$. (**c**) Two different scales of *V*-shapes with the same angle ϕ are connected along joining fold lines. The length b of the parallelogram facets in the left zigzag strip of *V*-shapes is half that of the strip on the right in the unit cell shown.

The relationship between the angle ϕ and the fold angle θ is as follows:

$$\tan\phi = \cos\theta\tan\alpha \qquad (4.4)$$

The outer dimensions of a sheet made of tessellation of the same BCH_n (Figure 4.2(b)) are given by

$$W = m_2 \left(2b \sin \phi \right) \qquad L = m_1 \left(2a \frac{\cos \alpha}{\cos \phi} + \frac{n-1}{n} b \cos \phi \right) + \frac{1}{n} b \cos \phi \qquad (4.5)$$

Note that, in the relation given for the length L, the expression within the parentheses presents the length of the repeating unit cell, and the last term shows the edge effect. The second term within the parentheses is related to the effect of the holes in the tessellation.

For the case of rigid panels connected via elastic hinges at fold-lines, from the geometry, the BCH with $n=2$ has only one independent DOF. In general, the number of DOFs for each unit cell of BCH_n is ($2n-3$). Using at least two consecutive rows of small parallelograms, instead of one, in BCH_n (see Figure 4.9(b)) decreases the DOFs of the BCH to one irrespective of the number of n (see Figure 4.10 and Section 4.7.6.1 in supplementary materials for more details). Additionally, the patterns are all rigid and flat-foldable, and can be folded from a flat sheet of material, i.e., they are developable. In Figure 4.3, a few configurations of the patterns are presented.
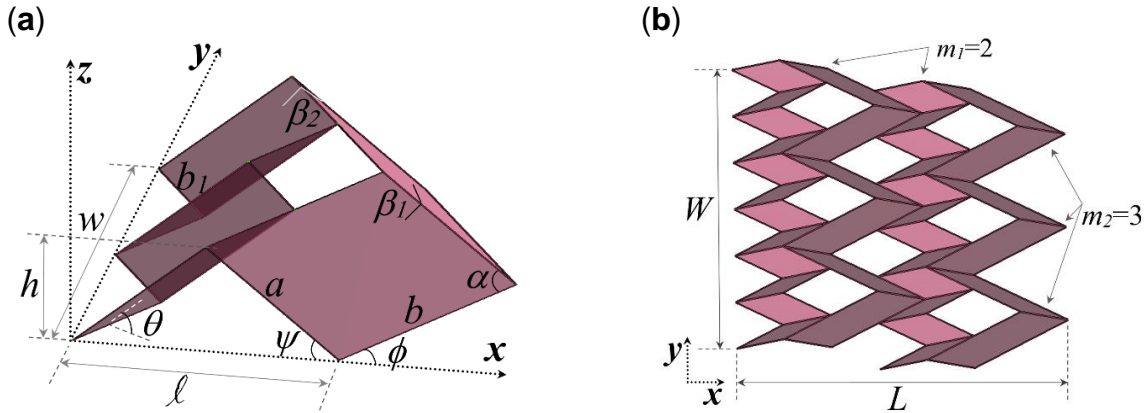
Figure 4.2: Geometry of BCH_n pattern. (**a**) Geometry of the unit cell. The geometry of a sheet of BCH_n can be parameterized by the geometry of a parallelogram facet (a, b and α), half number of small parallelogram facets (n) and fold angle $\phi \in [0, \alpha]$ which is the angle between fold lines b and the x-axis. Other important angles in the figure are fold angle between the facets and the xy-plane, i.e., $\theta \in [0, \pi/2]$; angle between the fold lines a and the x-axis, i.e., $\psi \in [0, \alpha]$; and dihedral fold angles between parallelograms, $\beta 1 \in [0, \pi]$ and $\beta 2 \in [0, \pi]$, joined along fold lines a and b, respectively. (**b**) A sheet of BCH_2 with $m_1=2$, $m_2=3$ and outer dimensions of L and W.

4.4 Mechanical Properties of BCH$_n$ Patterns

In the present research, we obtain the in-plane Poisson's ratio in two different ways:

- Considering the projected lengths of the zigzag strips.
- Considering the end-to-end dimensions of a sheet.

Note that while the first approach is valuable to provide insight on the kinematics of a zigzag-base folded sheet such as the Miura-ori and BCH$_2$, the latter definition can also be relevant depending on the application. To place emphasis on these two important concepts in relation to the folded sheet materials introduced in this work, we designate the value obtained by the first approach as υ_z and the latter as υ_{e-e}, where the indices z and e-e stand for zigzag and end-to-end, respectively (see Figure 4.4(a) and Figure 4.11). In this regard, for the sheet of BCH$_2$ shown in Figure 4.2(b), ℓ and L are used to obtain υ_z and υ_{e-e}, respectively. Notice that ℓ for a sheet is the sum of the projected lengths of the zigzag strips in the xy-plane and parallel to the x-axis, and for a sheet made of tessellation of identical BCH$_2$ is equal to m_1 times that of a unit cell (Figure 4.4(a)). Also, L is the end-to-end dimension of the sheet as shown in Figure 4.2(b). Furthermore, in both approaches $W=w$. Hence, υ_z of the sheet is given in the following which is equal to the kinematics of a V-shape described in the previous sections.

$$\left(\upsilon_{w\ell}\right)_z = -\frac{\varepsilon_\ell}{\varepsilon_w} = -\frac{d\ell/\ell}{dw/w} = -\tan^2\phi \tag{4.6}$$

Accordingly, BCH$_2$ and all other combined patterns of BCH with one-DOF planar mechanism (e.g., patterns shown in Figure 4.3) have υ_z equal to $-\tan^2\phi$ (i.e., υ_z of a Miura-ori sheet with the same fold angle [10, 39] - see Figure 4.4 (a) and (b)). We emphasize that the in-plane Poisson's ratio, obtained by considering the projected lengths of the zigzag strips in the patterns, also provides insight that the components with identical υ_z can be connected to get a material which can fold and unfold freely (e.g., see Figure 4.3(f)). Additionally, using this insight, we can create numerous configurations of metamaterials (see Section 4.7.1 in supplementary materials for more details). For the sheets made of tessellation of the same BCH$_n$ (e.g., Figure 4.3(a)), υ_{e-e} is given by

$$\left(\upsilon_{WL} \right)_{e-e} = -\frac{\varepsilon_L}{\varepsilon_W} = -\frac{dL/L}{dW/W} = -\tan^2\phi \frac{\kappa \cdot \lambda \cos\alpha - \cos^2\phi}{\kappa \cdot \lambda \cos\alpha + \cos^2\phi} \tag{4.7}$$

in which

$$\kappa = \frac{2n \cdot m_1}{m_1(n-1)+1} \qquad \text{and} \qquad \lambda = \frac{a}{b} \tag{4.8}$$

in which $n=2$ (notice that $n=1$ gives the relation for the Miura-ori sheet). Considering the end-to-end dimension, for a unit cell of BCH_2 ($m_1=1$), the υ_{e-e} is similar to that of a Miura-ori unit cell (Figure 4.4(c)) and is given by

$$\left(\upsilon_{WL} \right)_{e-e} = -\tan^2\phi \frac{2\lambda \cos\alpha - \cos^2\phi}{2\lambda \cos\alpha + \cos^2\phi} \tag{4.9}$$

Therefore, unlike υ_z which is always negative (Figure 4.4(b)), υ_{e-e} can be positive for some geometric ranges (Figure 4.4 (c) and (d)). Moreover, υ_z is only a function of the angle ϕ, but υ_{e-e} can be dependent on other geometric parameters, i.e., the geometry of the facets (a, b, α), tessellations (n, m_1) and the angle ϕ. Notice that Poisson's ratio considering the end-to-end dimensions can be positive even for a Miura-ori unit cell (Figure 4.4(c)). Also, note that the shift from negative to positive Poisson's ratio in Miura-ori is only the effect of considering the tail [78], and the difference between two Poisson's ratios (i.e., υ_z and υ_{e-e}) vanishes as the length of the Miura-ori sheet approaches to infinity. However, note that for the BCH patterns with holes, the transition to positive Poisson's ratio is mainly the effect of the holes in the sheets, and unlike the Miura-ori, even for a BCH sheet with an infinite configuration, the difference between these two approaches (i.e., υ_z and υ_{e-e}) does not disappear (see Figure 4.5). In this regard, Figure 4.5 presents Poisson's ratio of a repeating unit cell of BCH_2 pattern (within an infinite tessellation) which corresponds to the following expression.

$$\left(\upsilon_\infty \right)_{e-e} = -\tan^2\phi \frac{4\lambda \cos\alpha - \cos^2\phi}{4\lambda \cos\alpha + \cos^2\phi} \tag{4.10}$$

From the Equation above, $\left(\upsilon_\infty \right)_{e-e}$ for the BCH_2 sheet is positive if $4\lambda \cos\alpha < \cos^2\phi$. The value is negative if $4\lambda \cos\alpha > \cos^2\phi$.

Analogous to Miura-ori sheet [10], similar sheets possessing the same υ_z can be designed to be stacked and attached together along joining fold lines to form cellular folded metamaterials with capability of folding freely (Figure 4.3 (g) and (h), Figure 4.14). Note that the sheets tailored for the stacking have identical υ_{e-e} which further confirms the relevance of defining the υ_{e-e} as an important concept for the folded sheet metamaterials (see Section 4.7.3.1 in supplementary materials for more details).

Considering that the facets are rigid and are connected via elastic rotational springs along the fold lines, we obtained the planar stretching stiffness of BCH$_2$, in both *x* and *y* directions (Figure 4.13) and compared the results with their corresponding values for the Miura-ori cell. From Figure 4.6, we infer that depending on the geometry and considering the same amount of material (compare Figure 4.2(a) with Figure 4.12), BCH$_2$ can be more or less stiff than its corresponding Miura-ori cell in the *x* and *y* directions.

Similarly to Miura-ori pattern, simple experimental observations show that these folded sheets exhibit anticlastic (saddle shape) curvature under bending (see Figure 4.7(a)), which is an adopted curvature by conventional materials with positive out-of-plane Poisson's ratio [88]. This positional semi-auxetic behavior has been observed in the 'anti-trichiral' honeycomb [91] and auxetic composite laminates [92], as well as in other patterns of folded sheets made of conventional materials [10, 23, 39].
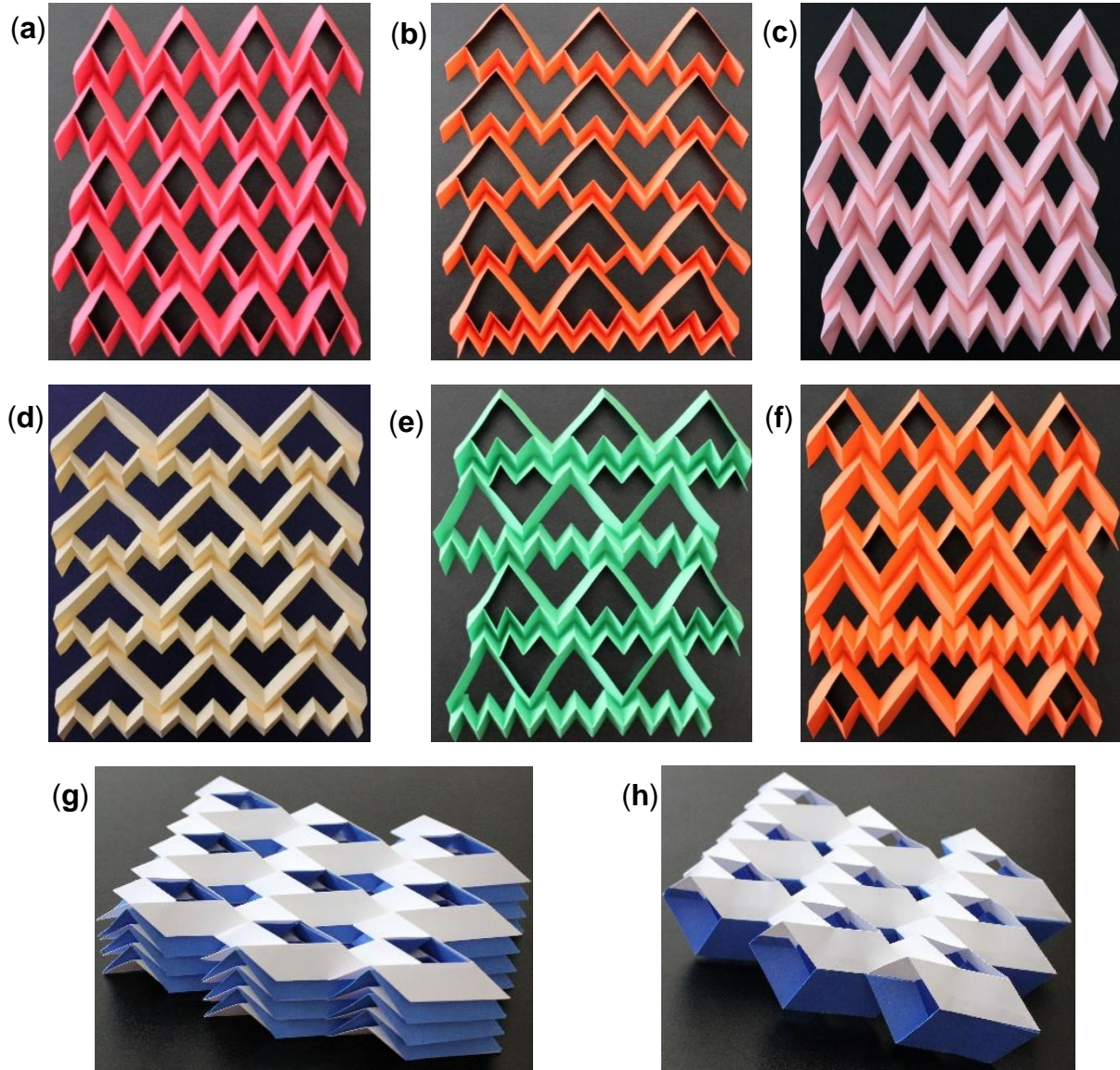
Figure 4.3: Sample patterns including BCH_n and cellular folded metamaterials. (**a**) A sheet of BCH_2. (**b**) A sheet of BCH_3. Adding one layer of small parallelograms to the first row reduces the DOF of the system to 1 for rigid origami behavior. (**c**) Combination of BCH_2 and layers of large and small parallelograms with the same geometries as the ones used in the BCH_2. (**d**) Combination of BCH_3 and layers of large and small parallelograms with the same geometries as the ones used in the BCH_3. (**e**) Sheet of BCH_3 and layers of small parallelograms with the same geometries as the ones used in the BCH_3. (**f**) A sheet composed of various BCH_n and Miura-ori cells with the same angle ϕ. (**g**) A stacked cellular metamaterial made from 7 layers of folded sheets of BCH_2 with two different geometries. (**h**) Cellular metamaterial made from 2 layers of 3x3 sheets of BCH_2 with different heights tailored for the stacking purpose, and bonded along the joining fold lines. The material is flat-foldable in one direction.
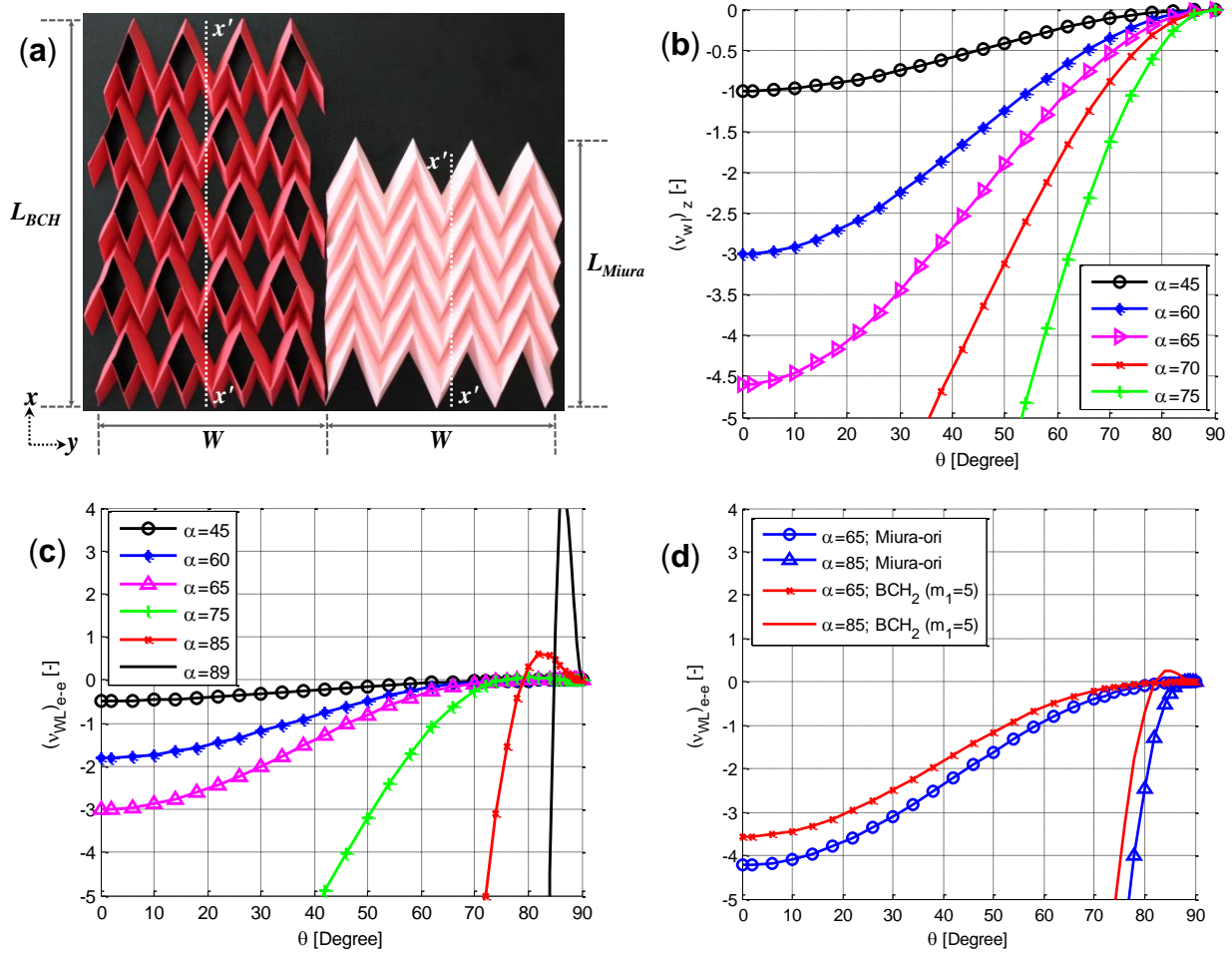
Figure 4.4: In-plane Poisson's ratios of the metamaterials introduced in this work. (**a**) 5x4 (m_1=5 and m_2=4) BCH$_2$ sheet (left image) and its corresponding Miura-ori sheet (right image) with the same geometry, and the same amount of material. Projected lengths of the zigzag strips along **x'-x'** line parallel to the **x**-axis is used to obtain υ_z and L is used to obtain υ_{e-e}. Both sheets have identical υ_z, but they have different υ_{e-e}. (**b**) In-plane kinematics (υ_z) for the class of metamaterials. (**c**) In-plane Poisson's ratio considering the end-to-end dimensions (υ_{e-e}) for the unit cell of Miura-ori and BCH$_2$ patterns with $a=b$. (**d**) In-plane Poisson's ratio considering the end-to-end dimensions (υ_{e-e}) for sheets of Miura-ori and BCH$_2$ with m_1=5 and $a=b$.
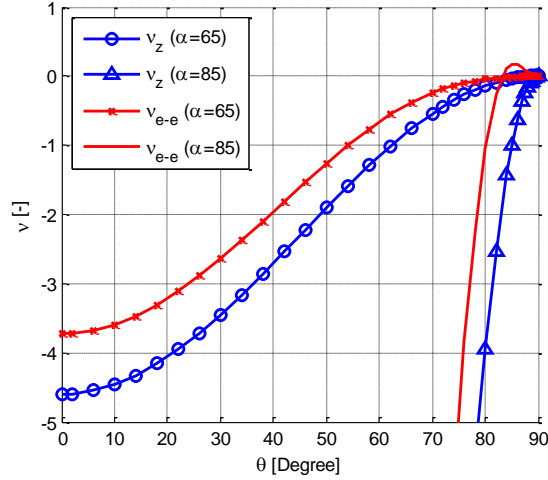
Figure 4.5: In-plane Poisson's ratio of the BCH$_2$ sheet for an infinite configuration. Poisson's ratio obtained by considering the projected length of the zigzag strips, υ_z, versus Poisson's ratio considering the end-to-end dimensions of the sheet when the sheet size approaches infinity, υ_{e-e} (a=b and $m_1 \to \infty$). The latter is equivalent to the Poisson's ratio of a repeating unit cell of BCH$_2$ within an infinite tessellation. The figure shows that, contrary to the Miura-ori, the transition towards positive Poisson's ratio is present for an infinite configuration of the BCH$_2$ sheet.

We investigated the effect of the geometry and material properties on the global behavior of the folded sheets, using the bar-framework numerical approach described by Schenk and Guest [10]. By considering the bending stiffness of the facets and fold lines (K_{facet} and K_{fold}, respectively), we studied the modal responses of the folded shells by changing the ratio of K_{facet} to K_{fold}. For the pattern of BCH$_2$, shown in Figure 4.7, similarly to a regular Miura-ori sheet [23], twisting and bending modes are the predominant behavior of the pattern over a range of K_{facet}/K_{fold} and associated geometries (Figure 4.7, (b) and (c)). Furthermore, the saddle-shaped bending mode obtained from eigen-value analysis of the patterns further confirms that the Poisson's ratio under bending is positive [88]. The results show that for large values of K_{facet}/K_{fold}, the first softest eigen-mode represents a rigid origami behavior (Figure 4.7(d)). The results of the stiffness analysis for several other patterns from the class of metamaterials show similar behavior (see Figure 4.15 to Figure 4.17).
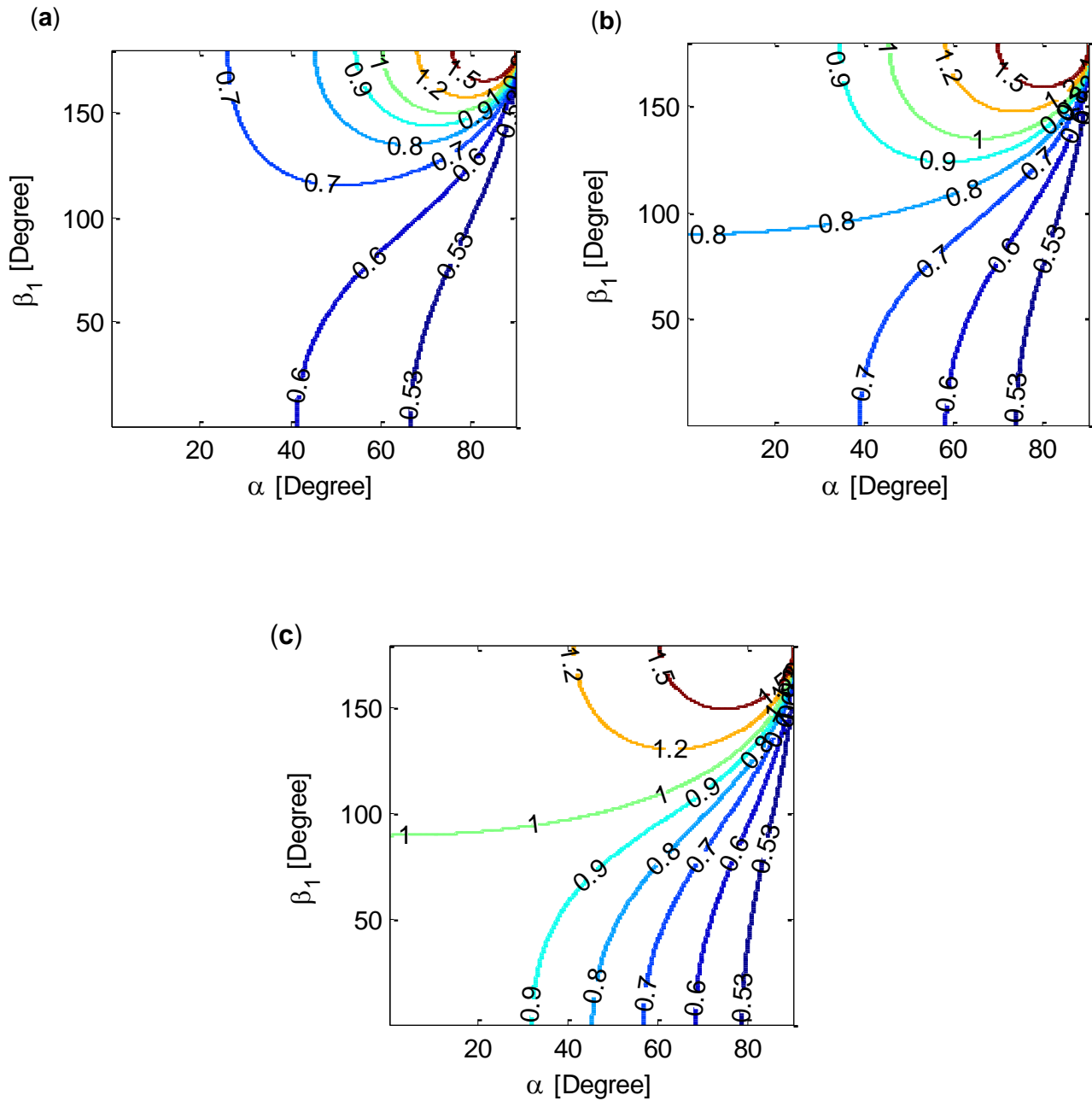
Figure 4.6: Ratio of in-plane stiffness of Miura-ori cell to that of the BCH_2 in the *x* and *y* directions. The results show that depending on the geometry and considering the same amount of material, BCH_2 can be more or less stiff than its corresponding Miura-ori cell in the *x* and *y* directions. (**a**) *a/b=2*. (**b**) *a/b=1*. (**c**) *a/b=1/2*.
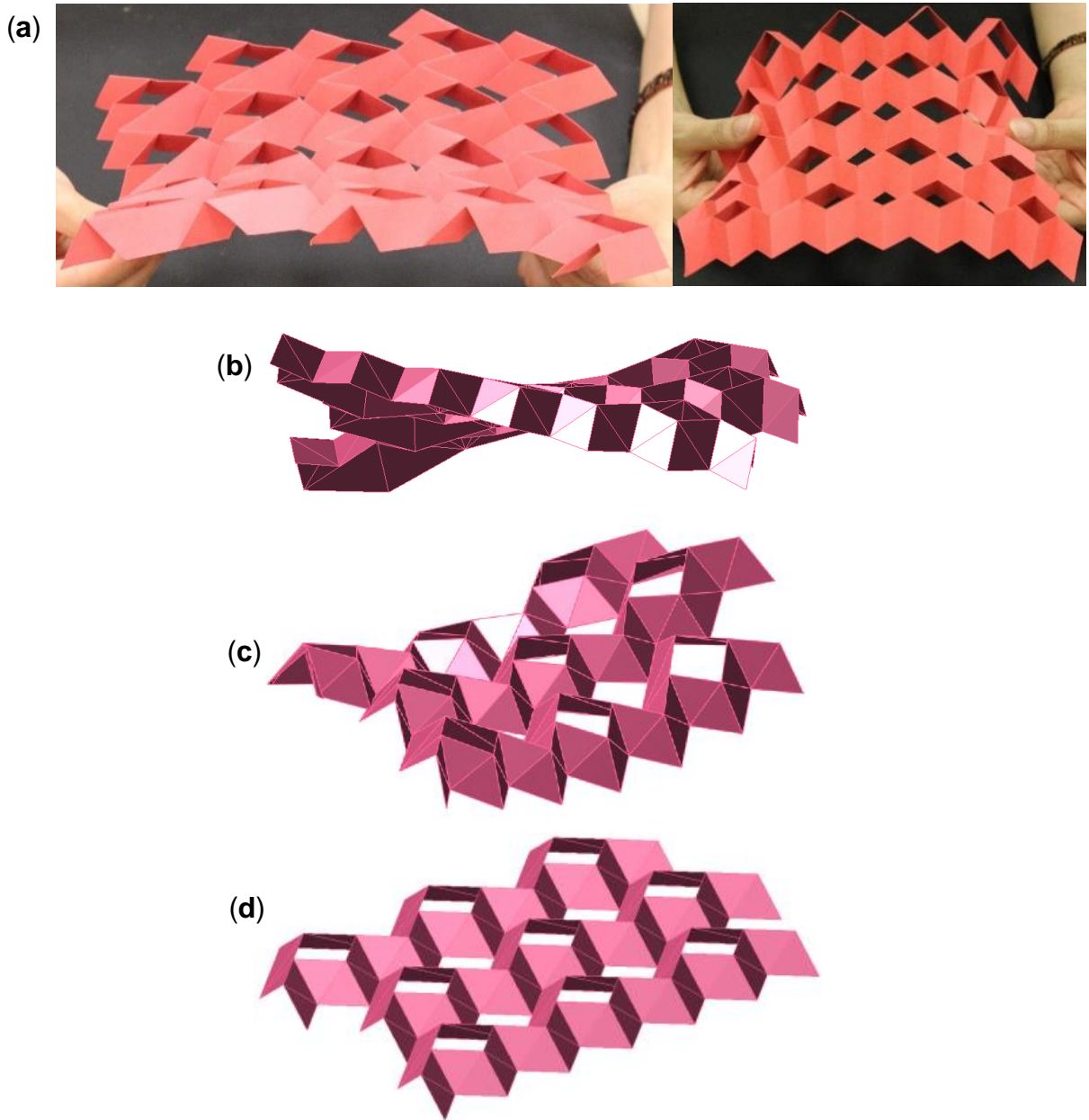
Figure 4.7: Behavior of sheet of the BCH_2 under bending and the results of the eigenvalue analysis of a 3 by 3 pattern of BCH_2. (**a**) A sheet of BCH_2 deforms into a saddle-shaped under bending (i.e., a typical behavior seen in materials with a positive out-of-plane Poisson's ratio). (**b**) Twisting, (**c**) saddle-shaped and (**d**) rigid origami behavior (planar mechanism) of a 3 by 3 pattern of BCH_2 ($a=1$; $b=2$; $\alpha = 60^\circ$). Twisting and saddle-shaped deformations are the softest modes observed for a wide range of material properties and geometries. For large values of K_{facet}/K_{fold} the rigid origami behavior (planar mechanism) is the softest deformation mode of the sheets.

4.5　Discussion

Most research on origami-inspired materials relies on known patterns, especially on the Miura-ori, i.e., a classic origami pattern with outstanding properties and a wide range of applications. In this study, we have created the BCH_2 pattern among other combined patterns and we have shown that the patterns possess properties as remarkable as those of the Miura-ori. We summarize significant outcomes of the current research in Figure 4.8 and discuss in the following.
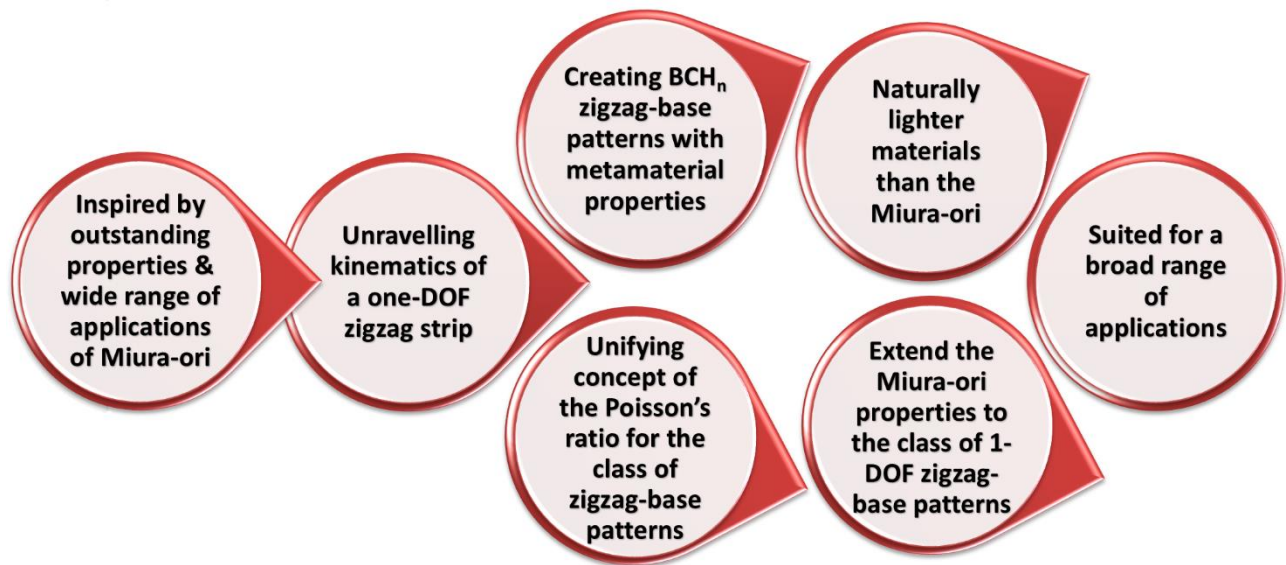
Figure 4.8: Outcomes of the current study. Inspired by the Miura-ori to create the novel BCH_n zigzag-base patterns with a broad range of applications.

We have employed the concept of the in-plane Poisson's ratio, a key material property in the present study, in two different contexts (see Table 4.1 in supplementary material):

- ***To describe the kinematics and to create a class of one-DOF zigzag-base mechanical metamaterials***: The Poisson's ratio is obtained by considering the projected lengths of the zigzag strips, v_z, and the value is always equal to $-\tan^2\phi$. The value obtained in this way is an inherent property of the class of one-DOF zigzag-base folded sheets, and is related to the foldability of the class of the metamaterials. Hence, the concept is insightful to create novel zigzag-base foldable materials. Note that to describe the stacking of the Miura-ori in the literature [10], the value (i.e., $-\tan^2\phi$) has been associated to the

Poisson's ratio of the Miura-ori sheet [10]. However, in the present work, by explicitly associating the value to that of a one-DOF zigzag strip (Figure 4.1), we have scaled down the width of one joining zigzag strip in the unit cell, and created the BCH patterns containing various scales of zigzag strips. Accordingly, the present study extends the kinematics of the Miura-ori to that of a class of one-DOF zigzag-base folded sheet metamaterials. In other words, our work shows that all one-DOF zigzag-base folded metamaterials shown in Figure 4.3 have identical kinematics, if the angle ϕ is the same.

- ***To study the size change of a folded metamaterial introduced in this work***: The Poisson's ratio is obtained by considering the end-to-end dimensions of the sheet, υ_{e-e}. Note that this definition captures the size change of a finite sheet (Figure 4.4) and that of a repeating unit cell (within an infinite configuration) for a regular sheet (e.g., regular BCH$_2$ - see Figure 4.5). Moreover, it is applicable for irregular sheets such as the one shown in Figure 4.3(f).

Because recent literature on the topic had differing expressions regarding Poisson's ratio evaluation [10, 39, 78], by introducing a class of zigzag-base folded sheet materials, this study further clarifies the issue and unifies the concepts. In this regard, for the Miura-ori sheet, the Poisson's ratio of a repeating unit cell is equal to υ_z. Hence, the value given in [10, 39] presents both the kinematics of the Miura-ori sheet and the size change of a repeating unit cell of the Miura-ori. Thus, considering the end-to-end dimensions in a finite Miura-ori sheet is to simply capture the edge effect [78] (i.e., the last term given in Equation (4.5) for the *L*). However, for the BCH$_2$ pattern, the Poisson's ratio of a repeating unit cell is not equal to υ_z, and it assumes both negative and positive Poisson's ratios due to the presence of the holes in the pattern (Figure 4.5). Therefore, our study shows that considering the end-to-end configuration for the BCH$_2$ pattern is mainly to capture the effect of the holes in the Poisson's ratio (i.e., the second term within parentheses in Equation (4.5) for the *L*).

We have also shown that BCH$_n$ and combined patterns, introduced in this work, possess metamaterial properties arising from their tunable geometrical configurations. An appealing feature of these patterns is that they display similar properties to those of the Miura-ori, however, presence of the different scales of zigzag strips in the structure of the patterns as well as

existence of the holes make the BCH_n patterns unique (e.g., see Figure 4.4(a)). In addition, the fact that the BCH_n mechanical properties differ from those of the Miura-ori (e.g., see Figure 4.6 and Figure 4.4(d)) offer avenues to explore alternative materials and structures based on these patterns for a certain performance/application of Miura-ori pattern on which there is a surge of research interest. On the other hand, present technology requires lighter and more customizable structures and materials. Combining BCH_n patterns with Miura-ori provides an augmented design space for tailored engineering design of materials and structures. Consequently, availability of large design motifs can be advantageous, for instance, in dynamic architectural façades where the place of the holes in the patterns can be controlled by combining Miura-ori with BCH_n to either allow light in the interior of the building or to promote shading when desirable.

The main assumptions in this study are highlighted as: (i) to obtain the in-plane Poisson's ratio, we have assumed a rigid origami behavior. (ii) To perform stiffness analysis and to capture the effect of the stiffness of the panels to that of the fold lines in the global behavior of the patterns, we have assumed that the panels do not stretch, and bending happens only around the fold lines (including the added fold lines).

In summary, the remarkable properties of the patterns (specifically BCH_2), such as rigid-foldability, flat-foldability, and possessing one DOF, as well as numerous possible combinations of the patterns make them potentially suited for a broad range of applications including kinetic and deployable structures (e.g., solar sails [24]), light cellular foldcore sandwich panels [68, 16], 3D tunable folded cellular metamaterials [10, 62, 63], energy absorbing devices [49], foldable robots [93] and auxetic materials [88, 89]. In all these applications, scalability is a major feature of the BCH_n or other combined patterns (due to their inherent geometric properties).

4.6 Materials and Methods

To experimentally assess mechanical behavior of the origami-inspired patterns, we fabricate samples from various types of materials including 20, 24, and 28 lb papers, 76 lb construction paper, and 110 lb cardstock. For creating holes and patterning creases, we employ an electronic cutter. We first design the patterns and then convert to a vector format appropriate for electronic

cutting. The crease lines are perforated using a dash-and-gap style. After patterning, we fold the sheets manually along the fold lines constituting the mountains and valleys of the folded sheets. We verify the observed behavior of the materials numerically using a stiffness analysis over a broad range of materials including rigid panels connected via frictionless hinges.

4.7 Supplementary Materials

4.7.1 Geometry, pattern tessellation and combination

The geometry of BCH$_n$ (Basic unit Cell with Hole) is described in the main text and is shown in Figure 4.2(a). The end-to-end dimensions of a sheet made of tessellation of the same BCH$_n$ (see Figure 4.2(b)) are given by

$$W = m_2 \left(2b\sin\phi\right) \qquad\qquad L = m_1 \left(2a\frac{\cos\alpha}{\cos\phi} + \frac{n-1}{n}b\cos\phi\right) + \frac{1}{n}b\cos\phi \qquad (4.11)$$

By combining BCH$_n$ with row/rows of small and/or large parallelograms with the same angle ϕ, we can obtain numerous unit cells. A few configurations are presented in Figure 4.9. The tessellations or/and combinations of tessellation of these cells having the same angle ϕ can result in a new metamaterial. For example, patterns shown in Figure 4.3 (c) and (d) are obtained by tessellations of the unit cells presented in Figure 4.9(d).
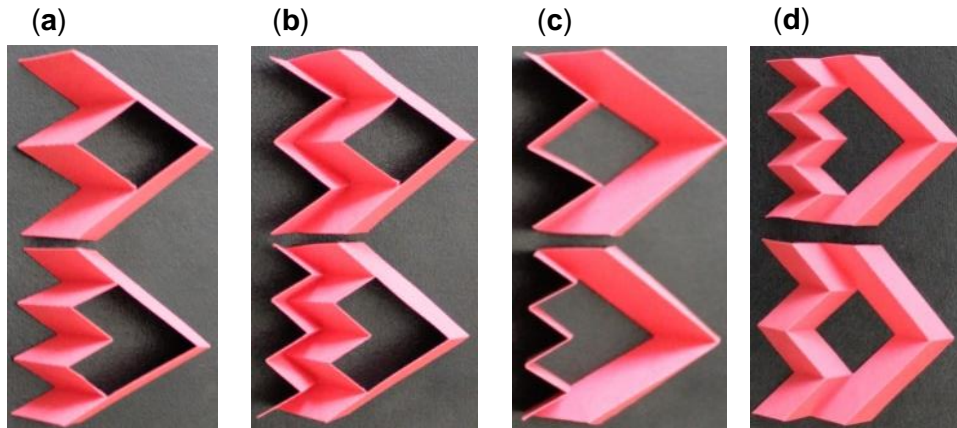
Figure 4.9: BCH$_2$ and BCH$_3$ and their combinations with row/rows of small and/or large parallelograms. (**a**) A BCH$_2$ and a BCH$_3$. (**b**) A BCH$_2$ and a BCH$_3$ combined with a row of small parallelograms with the same geometry as the one used in the corresponding BCH. (**c**) A BCH$_2$ and a BCH$_3$ combined with a row of large parallelograms with the same geometry as the one used in their corresponding BCH. (**d**) A BCH$_2$ and a BCH$_3$ combined with rows of small and large parallelograms with the same geometry as the one used in their corresponding BCH.

4.7.2 Number of degrees of freedom of the patterns

For the case of $n=2$, i.e., for the unit cell of BCH$_2$ pattern shown in Figure 4.2(a), and for a given geometry of the facet, the geometry of the unit cell implies that it can be defined based on only one fold angle (i.e., similarly to Miura-ori [10], we can write the relations between all degrees of freedom (DOFs) based on only one fold angle, e.g., the angle ϕ). Hence, the unit cell of BCH$_2$ has only one DOF. On the other hand, implicit formation of the structure of the Miura-ori unit cell with one DOF mechanism between two adjoining unit cells, as shown in Figure 4.10(a), imposes the whole pattern to have only one DOF. The conclusion is further verified using numerical calculation of the number of DOFs as described in Section 4.7.6.1.
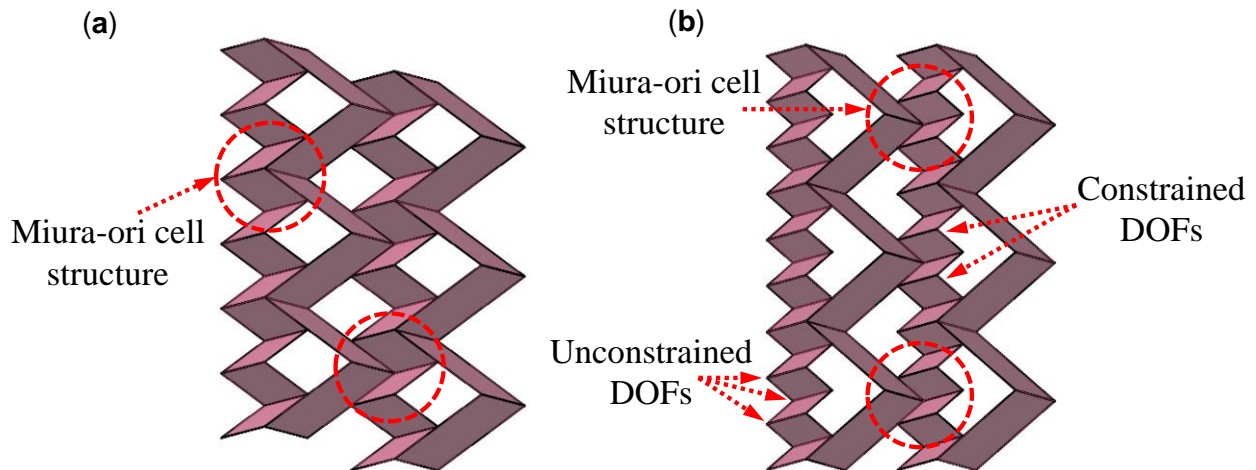
Figure 4.10: Constrained DOFs by implicit formation of the structure of the Miura-ori unit cell between adjoining unit cells of BCH$_2$ and BCH$_3$ in the pattern. (**a**) Although the unit cell of the pattern shown, BCH$_2$, does not have Miura-ori unit cell, the Miura-ori unit cell structure formed implicitly in the tessellation makes the whole BCH$_2$ pattern fold with one-DOF planar mechanism. (**b**) In the symmetric tessellation of identical BCH$_3$, except for the small parallelogram facets of the first row, all other independent DOFs in the unit cell of BCH$_3$ are constrained by the structure of the Miura-ori cell formed between two adjoining unit cells.

In general, from the numerical model described in Section 4.7.6.1 and for rigid origami behavior, the unit cell of BCH$_n$ (Figure 4.9(a)) has $2n$-3 DOFs. However, adding one row of small

parallelogram facets to the BCH$_n$ (e.g., Figure 4.9(b)), i.e., creating a complete row of Miura-ori unit cells with the small parallelogram facets, reduces the DOF of the cell to 1 irrespective of the number of n. Hence, tessellation of the unit cells shown in Figure 4.9(b) can create patterns with one DOF planar mechanism (e.g., Figure 4.3(e)).

For the symmetric tessellation of BCH$_3$, as presented in Figure 4.10(b), except for the first row of small parallelogram facets, all other independent DOFs in the unit cell of BCH$_3$ are constrained by the implicit formation of the structure of Miura-ori cell between two adjoining unit cells. Hence, the pattern of BCH$_3$, shown in Figure 4.10(b), due to existence of unconstrained DOFs in the first row of small parallelogram facets, has more than one DOF. However, adding one row of small parallelogram facets, and accordingly creating the row of Miura-ori cells with small parallelogram facts can reduce the DOF of the whole system to one (e.g., Figure 4.3(b)).

4.7.3   In-plane stretching response of BCH$_n$ sheets

4.7.3.1   Poisson's ratio

A 5x4 sheet of BCH$_2$ along with its corresponding Miura-ori sheet containing the same geometry of facets and fold angle (a, b, α and ϕ are identical in both models) is shown in Figure 4.4(a). The Poisson's ratio υ_z for both sheets can be obtained from the following relation

$$\left(\upsilon_{w\ell}\right)_z = -\frac{\varepsilon_\ell}{\varepsilon_w} = -\frac{d\ell/\ell}{dw/w} \tag{4.12}$$

in which ℓ is the projected length of the zigzag strips in the *xy*-plane and parallel to the *x*-axis (*i.e.*, the projected lengths of the strips along any arbitrary lines of *x'-x'* in the *xy* plane and parallel to the *x*-axis intersecting a complete tessellation). Hence, for a sheet with m_1 rows, ℓ is equal to m_1 times the projected lengths of the strips in the unit cell shown in Figure 4.2(a). From Figure 4.4(a), the importance of considering the end-to-end dimensions to obtain the Poisson's ratio for folded sheets is more pronounced in sheets with holes, because both sheets have the same υ_z despite having different lengths along the *x*-axis. Another example, showing the

relevance of the end-to-end dimensions to obtain Poisson's ratio of folded sheets is presented in Figure 4.11, where two identical 2x2 Miura-ori sheets are shown. Moreover, 2 rows of small Mira-ori cells with equal υ_z are also attached to the left-hand sample as shown in the figure. Therefore, from the figure, considering the end-to-end dimensions to obtain Poisson's ratio in the left system is obvious. For the limit cases of very large number of small cells, as well as very small length of a for small cells (*i.e.*, $n \to \infty$ and $a_s \to 0$. See Figure 4.12 for the geometry of Miura-ori cell), the rows of small Miura-ori cells approach the lines defining the end-to-end dimension for the 2x2 Miura-ori sheet shown on the right-hand image.

From the expression (4.6) in the main text, when $\kappa \cdot \lambda \cos \alpha < \cos^2 \phi$, υ_{e-e} is positive and for $\kappa \cdot \lambda \cos \alpha > \cos^2 \phi$, υ_{e-e} is negative.
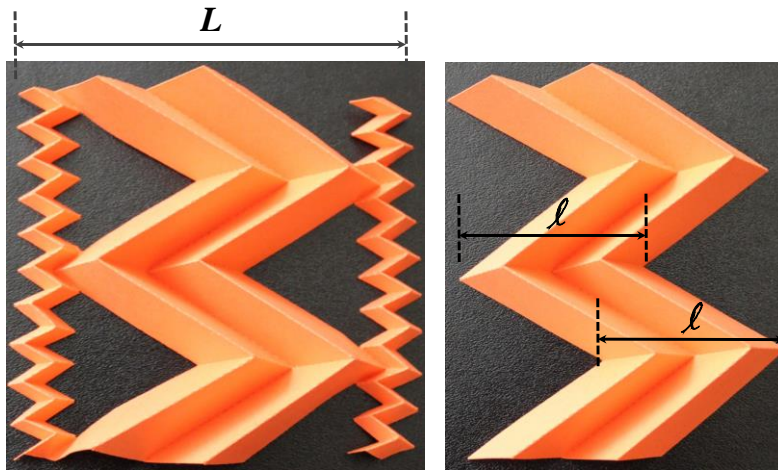
Figure 4.11: Concept of Poisson's ratio considering the end-to-end dimensions. Figure shows two identical 2x2 Miura-ori tessellations. The 2 rows of small Mira-ori cells with the same υ_z as that of the 2x2 sheet are attached to the left sample. Length b of the small cells are 1/5 of that of the large cells (*i.e.*, the number of small cells per each large cell is 5 (*n=5*)).
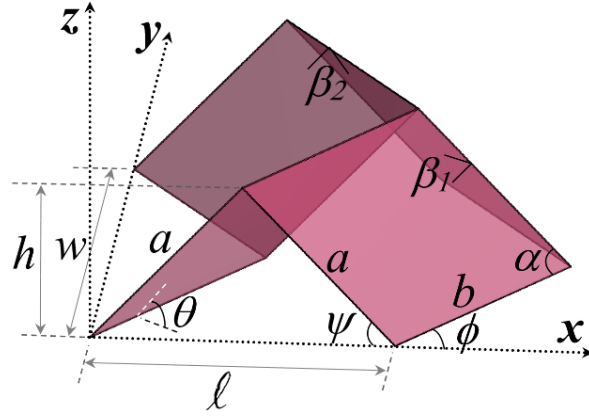
Figure 4.12: Geometry of Miura-ori cell.

For a Miura-ori ($n=1$) sheet, we have

$$\left(\upsilon_{WL}\right)_{e-e} = -\tan^2\phi \frac{2m_1\lambda\cos\alpha - \cos^2\phi}{2m_1\lambda\cos\alpha + \cos^2\phi} \tag{4.13}$$

Hence, for a Miura-ori sheet, if $m_1 \to \infty$, then υ_{e-e} approaches υ_z (*i.e.*, $-\tan^2\phi$). Notice that from the above relation, even a Miura-ori unit cell (i.e., $m_1 = 1$) can have positive Poisson's ratio for some ranges.

Also, for a sheet of BCH$_2$, we have

$$\left(\upsilon_{WL}\right)_{e-e} = -\tan^2\phi \frac{\dfrac{4m_1}{m_1+1}\lambda\cos\alpha - \cos^2\phi}{\dfrac{4m_1}{m_1+1}\lambda\cos\alpha + \cos^2\phi} \tag{4.14}$$

Note that from the above relation, for a sheet of BCH$_2$, while comparing υ_z with υ_{e-e}, the shift towards positive Poisson's ratio in υ_{e-e} is mainly the effect of the holes, and thus the difference between υ_z and υ_{e-e} does not disappear (see Figure 4.5) when the length of the sheet approaches to infinity ($m_1 \to \infty$). Table 4.1 summarizes the main points on the in-plane Poisson's ratio of the class of zigzag-base folded materials.

Table 4.1: Summary of main points on the in-plane Poisson's ratio of the class of zigzag-base folded metamaterials.

Using projected length of the zigzag strips	Using the end-to-end dimensions of a sheet
$$\upsilon_z = -\frac{d\ell/\ell}{dw/w} = -\tan^2\phi$$	$$\upsilon_{e-e} = -\frac{dL/L}{dW/W}$$
❖ By introducing BCH_n patterns, our work shows that the value is an inherent property of the class of one-DOF zigzag-base folded materials, and is always negative and is a function of the angle ϕ. ❖ Provides insight on the kinematics and thus on how to create zigzag-base foldable metamaterials. ❖ It has been used in the literature (*1*) as the Poisson's ratio of the Miura-ori, to describe the stacking of the Miura-ori sheets. ❖ By explicitly associating the value to each zigzag, and thus by changing the scale of the zigzags in the patterns, we have created the BCH_n patterns.	❖ The value captures the size change of the sheets, and is a function of the geometry of the facets, tessellation, and the angle ϕ. It can be positive depending on the geometry. ❖ For an infinite tessellation of a regular sheet, it captures the Poisson's ratio of a repeating unit cell. ❖ The in-plane Poisson's ratio of a repeating unit cell of the Miura-ori sheet, obtained in this way, is equal to υ_z. ❖ For the Miura-ori, considering the end-to-end is to simply capture the edge effect (*32*). However, for the BCH_n patterns, it is to capture the effect of the holes in the patterns.

4.7.3.2 Stretching stiffness
4.7.3.2.1 BCH$_2$

In this section, we derived the in-plane stiffness of the BCH$_2$ in the x and y directions. The results are also compared with those of the Miura-ori cell. For this purpose, an alternative parameterization for BCH$_2$ (the unit cell is shown in Figure 4.2, (a) and (b)) based on the dihedral angles between the rigid facets is used, which is similar to the equations of reference [39] for Miura-ori cell. To better compare the results, we kept the same symbols as those given for Miura-ori [39], provided that they are consistent with the symbols used in this work. Therefore,

$$\ell = 2a\zeta \qquad w = 2b\xi \qquad h = a\zeta \tan\alpha \cos(\beta_1/2) \qquad (4.15)$$

in which,

$$\xi = \sin\alpha \sin(\beta_1/2) \qquad \text{and} \qquad \zeta = \cos\alpha\left(1-\xi^2\right)^{-1/2} \qquad (4.16)$$

The potential energy of a BCH$_2$ (see Figure 4.2, (a) and (b)), subjected to uniaxial force in the x

direction, can be obtained from

$$H = U + \Omega \tag{4.17}$$

in which, U and Ω are elastic energy and potential of the applied load, respectively that are given by

$$U = \frac{1}{2}k\left(4a(\beta_1 - \beta_{1_0})^2 + b(\beta_2 - \beta_{2_0})^2\right) \tag{4.18}$$

$$\Omega = -\int_{\beta_{1_0}}^{\beta_1} f_x \frac{d\ell}{d\beta_1'} d\beta_1' \tag{4.19}$$

where k is the rotational hinge spring constant per unit length (k). Setting the condition $\partial H / \partial \beta_1 = 0$, the external force at equilibrium f_x can be obtained from

$$f_x = \frac{dU/d\beta_1}{d\ell/d\beta_1} = \frac{2k}{\cos\alpha\sin^2\alpha}\left(\frac{4(\beta_1 - \beta_{1_0})\left(1 - \xi^2\right)^{3/2} + \frac{b}{a}\cdot(\beta_2 - \beta_{2_0})\cos\alpha\left(1 - \xi^2\right)^{1/2}}{\sin\beta_1}\right) \tag{4.20}$$

Notice that K_x is obtained from the following expression

$$K_x(\alpha, \beta_{1_0}) = \frac{df_x}{d\ell}\bigg|_{\beta_{1_0}} = \frac{df_x}{d\beta_1}\cdot\frac{d\beta_1}{d\ell}\bigg|_{\beta_{1_0}} \tag{4.21}$$

$$K_x(\alpha, \beta_{1_0}) = \left(2k\cdot\frac{4a(1-\xi_0^2)^2 + b\cos^2\alpha}{a(1-\xi_0^2)^{1/2}\cos\alpha\sin^2\alpha\sin\beta_{1_0}}\right)\left(\frac{8a^2\cos\alpha}{\ell^3\sqrt{1 - \frac{4a^2\cos^2\alpha}{\ell^2}}\sqrt{\frac{4a^2}{\ell^2} - 1}}\right) \tag{4.22}$$

where, $\xi_0 = \xi(\alpha, \beta_{1_0})$. The contour plot of the stiffness ratio in the x direction (K_x/k) is shown Figure 4.13(a) for a unit cell with $a=b=1$, in terms of the facet angle α and fold angle β_1.

Similarly, for the y direction:

66

$$f_y = \frac{dU/d\beta_1}{dw/d\beta_1} = \frac{k}{b\sin\alpha} \cdot \frac{4a(\beta_1 - \beta_{1_0}) + b(\beta_2 - \beta_{2_0})\left(\dfrac{\cos\alpha}{1-\xi^2}\right)}{\cos(\beta_1/2)} \tag{A.23}$$

$$K_y(\alpha, \beta_{1_0}) = \frac{df_y}{dw}\bigg|_{\beta_{1_0}} = \frac{df_y}{d\beta_1} \cdot \frac{d\beta_1}{dw}\bigg|_{\beta_{1_0}} \tag{4.24}$$

$$K_y(\alpha, \beta_{1_0}) = \frac{k}{b}\left(\frac{4a(1-\xi_0^2)^2 + b\cos^2\alpha}{(1-\xi_0^2)^2 \sin\alpha\cos(\beta_{1_0}/2)}\right)\left(\frac{2}{\sqrt{4b^2\sin^2\alpha - w^2}}\right) \tag{4.25}$$

The contour plot of the stiffness in the *y* direction is shown in Figure 4.13(b) for a unit cell with $a=b=1$ in terms of the facet and fold angles, α and β_1, respectively.
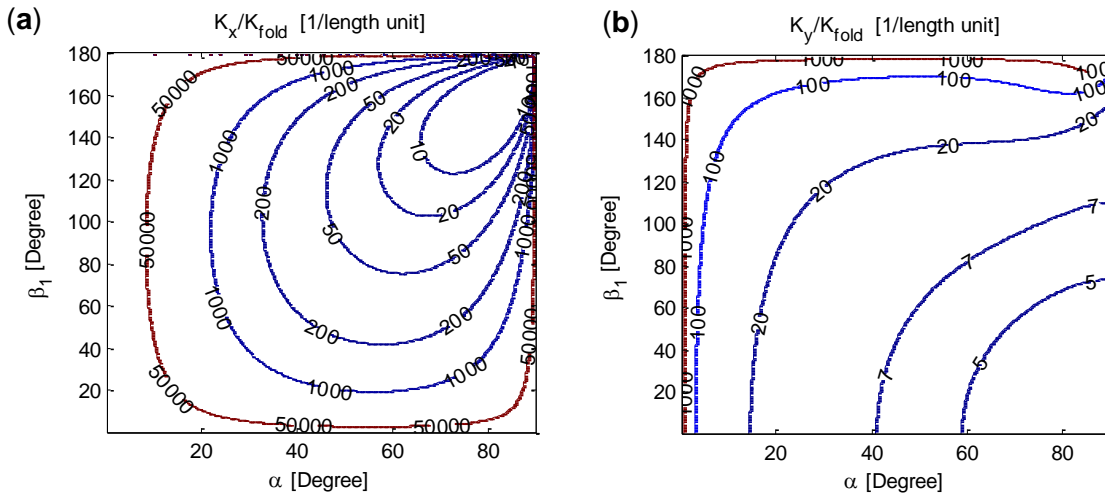
Figure 4.13: In-plane stiffness for the BCH₂ with *a=b=1*. (**a**) K_x/k. (**b**) K_y/k.

Note that to compare the in-plane stiffness results with those of the Miura-ori, we considered a measure of the in-plane stiffness which is equivalent to the load making the unit displacement in the zigzag strips of the unit cells (i.e., the length of the zigzag strips are used in the derivations).

4.7.3.2.2 Classical Miura-ori

The in-plane stretching stiffness in the x direction for Miura-ori cell is obtained by Equation (4.21), which results in

$$K_x(\alpha, \beta_{l_0}) = \left(4k \frac{a(1-\xi_0^2)^2 + b\cos^2\alpha}{a(1-\xi_0^2)^{1/2}\cos\alpha\sin^2\alpha\sin\beta_{l_0}} \right) \left(\frac{8a^2\cos\alpha}{\ell^3\sqrt{1-\dfrac{4a^2\cos^2\alpha}{\ell^2}}\sqrt{\dfrac{4a^2}{\ell^2}-1}} \right) \quad (4.26)$$

The second term within brackets is missing in Ref. [39]. Similarly, the stretching stiffness in the y direction is obtained by Equation (4.24), which results in

$$K_y(\alpha, \beta_{l_0}) = \left(2k \frac{a(1-\xi_0^2)^2 + b\cos^2\alpha}{b(1-\xi_0^2)^2\sin\alpha\cos(\beta_{l_0}/2)} \right) \left(\frac{2}{\sqrt{4b^2\sin^2\alpha - w^2}} \right) \quad (4.27)$$

Notice that K_x/k and K_y/k are not dimensionless, and thus K_x and K_y have dimension of the in-plane stretching stiffness [83]. See Section 3.3.1.2 in Chapter 3 for more information.

4.7.3.2.3 In-plane Stiffness of BCH$_2$ compared with its corresponding Miura-ori cell

Figure 4.6 shows the ratio of the in-plane stiffness of Miura-ori cell in the x and y directions to those of the BCH$_2$, for various ratios of a/b. The ratio is equal for both x and y directions because only the numerators of the first term in the planar stiffness relations change from BCH$_2$ to Miura-ori cell, and the numerators are equal in both planar rigidities of x and y directions for a specific unit cell.

4.7.4 Cellular folded metamaterial

Similar sheets with different heights, while possessing the same v_z, can be stacked and attached together along joining fold lines to make a cellular folded metamaterials (see Figure 4.3 (g) and (h) Figure 4.14). The fold geometry can change from layer to layer, but assuming stacking of the patterns using 2 layers of A and B [10], and by equating the external dimensions as well as v_z for

both layers of A and B, respectively, we have

$$b_B = b_A \qquad a_B = a_A \frac{\cos \alpha_A}{\cos \alpha_B} \tag{4.28}$$

$$\theta_B = \arccos\left(\cos \theta_A \frac{\tan \alpha_A}{\tan \alpha_B} \right) \tag{4.29}$$

where, the geometry of the layer B can be obtained based on that of the layer A. It is worth noting that meeting the above equations for the stacking of the layers results in the sheets possessing identical υ_{e-e} as well. This result further emphasizes the relevance of defining the end-to-end Poisson's ratio for the folded sheet metamaterials. Studies similar to the one given in [10] can be done on stacked folded cellular materials developed from the patterns introduced in this work.

The angle θ for the stacked samples shown in Figure 4.3(g) and Figure 4.14 is positive for both sheets, *i.e.* $\theta_A, \theta_B \in [0, \pi/2]$. This form of stacking may be applied as impact absorbing devices [49].

Considering the angle θ for one alternating layer being negative, *i.e.* $\theta_A \in [-\pi/2, 0]$ results in a new metamaterial in which the layers can be connected along joining fold lines using adhesive (Figure 4.3(h)). In this way of stacking, the heights for two successive layers can be identical.
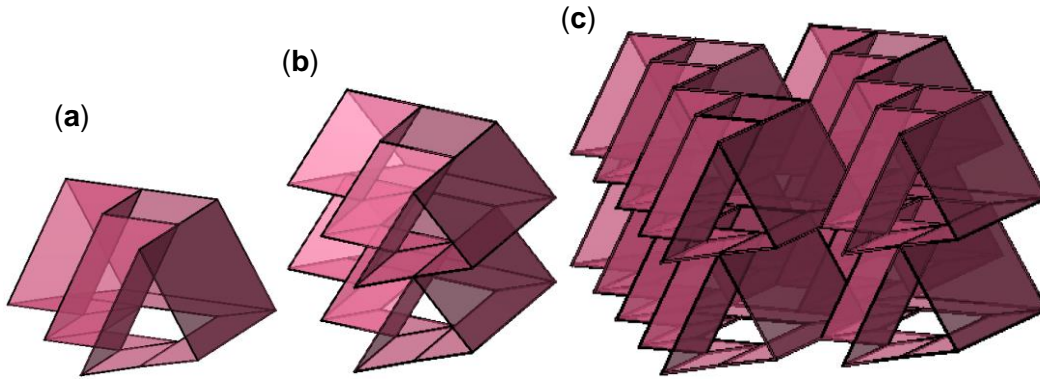
Figure 4.14: Sample stacked cellular folded metamaterials. The samples include layers of BCH_2 with two different geometries tailored for stacking. One alternating layer is almost unfolded ($\theta = 5°$) in these samples. (**a**) Two BCH_2 with different heights are attached along the joining fold lines. (**b**) 4 layers of BCH_2 with two different heights are attached along the joining fold lines. (**c**) 4 layers of 2x2 BCH_2 with two different heights are attached along the joining fold lines.

4.7.5 Experimental responses of the patterns

4.7.5.1 In-plane behavior

Under in-plane extension, the patterns, for large geometric ranges (see the analytical model in the main text), exhibit negative Poisson's ratios. Simple in-plane experimental tests show that, for most geometric ranges, the patterns exhibit negative Poisson's ratio.

4.7.5.2 Out-of-plane behavior

Under bending, this class of patterns folded from various types of papers exhibit anticlastic (saddle-shaped) curvature (see Figure 4.7(a), Figure 4.15(a), Figure 4.16(a) and Figure 4.17(a)) which is an adopted curvature by conventional materials with positive Poisson's ratio [24].

4.7.6 Numerical investigation of patterns behavior

To capture the effect of geometry and material properties on the global behavior of a folded shell system, a stiffness analysis can be carried out and the structure can be simulated using a Finite Element Analysis (FEA). Depending on the application, either a constrained bar-framework origami modeling approach [10, 23] or a modeling scheme using nonlinear shell elements can be used at this stage. In the current study, to model folded shell structures, we used the pin-jointed bar framework approach proposed by Schenk and Guest [10, 23]. In this modeling scheme, fold lines and vertices are modeled with bars and frictionless joints, respectively. To stabilize each facet and to model the bending of the facets for stiffness analysis, the facets are triangulated, and additional members are added to each facet. Placing of additional members is based on observations from physical models, stabilization of the facets, and energetic consideration in facet bending [10]. In that way, this model considers the bending of the facets and the effect of out-of-plane kinematics of the sheets, and therefore is not restricted to rigid origami.

By varying the ratio of the bending stiffness of the facets and fold lines (K_{facet}/K_{fold}), we performed stiffness analysis for 3x3 patterns of BCH_2 and BCH_3, and 2x3 patterns of the unit cells shown in Figure 4.9(d) with $\alpha=60$ degrees, $a=1$ and $b=2$. The stiffness analysis of the patterns reveals that twisting and bending modes are predominant behavior of the patterns over a large range of K_{facet}/K_{fold} and geometries (Figure 4.15-Figure 4.17, (a) and (b)). The modal shapes corresponding to the lowest eigen-value of the sheets show that for large values of K_{facet}/K_{fold}, the first softest deformation mode is representing a rigid origami behavior (Figure 4.15-Figure 4.17, (c)).

4.7.6.1 Numerical calculation of the number of DOFs of the patterns

In the bar-framework analysis, *compatibility* equation is to relate the nodal displacements $\boldsymbol{d}$ to the bar extensions $\boldsymbol{e}$ via compatibility matrix $\boldsymbol{C}$ as follows

$$\boldsymbol{Cd} = \boldsymbol{e} \tag{4.30}$$

From the above equation, the nullspace of the compatibility matrix provides the solution in which the bars do not extend. To model rigid origami behavior, we need to add an angular

constraint to the compatibility matrix whose nullspace can provide the nodal displacements $\boldsymbol{d}$ for which the facets do not bend either. The angular constraint can be written in terms of the dihedral fold angles between triangulated facets connected by added fold lines [10, 23]. Hence,

$$\boldsymbol{J}_{facet}\,\boldsymbol{d} = d\rho \tag{4.31}$$

where ρ is the dihedral fold angle between two adjoining triangulated facets and $\boldsymbol{J}_{facet}$ is the Jacobian of the angular constraint considered for the triangulated facets intersecting by added fold lines. Therefore, the augmented compatibility matrix is as follows

$$\bar{\boldsymbol{C}} = \begin{bmatrix} \boldsymbol{C} \\ \boldsymbol{J}_{facet} \end{bmatrix} \tag{4.32}$$

Accordingly, the number of internal infinitesimal mechanisms (*i.e.*, the number of independent DOFs) can be obtained from the expression

$$m = 3j - rank(\bar{\boldsymbol{C}}) - 6 \tag{4.33}$$

in which j is the number of joints (*i.e.*, the number of vertices). In the above relation, the 6 DOFs related to the rigid-body motions of 3D structures are excluded.

We used the above relation to obtain the number of DOFs for the patterns considering rigid origami behavior. The results are justified based on the geometry of the patterns as well as existence of the implicit formation of the structure of the Miura-ori cells with one-DOF mechanism as described in Section 4.7.2.
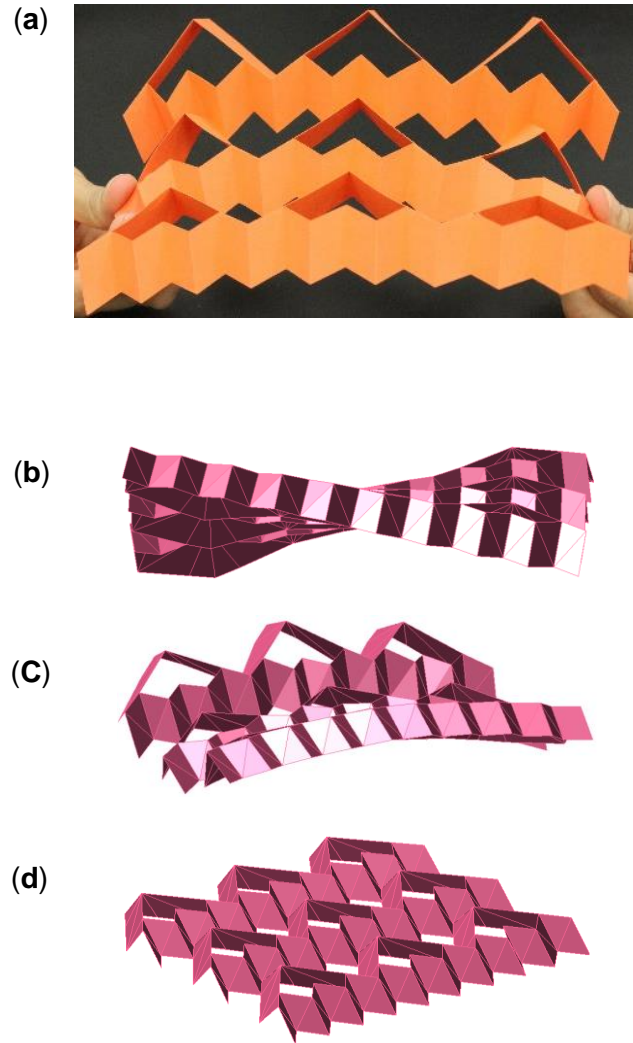
Figure 4.15: Behavior of the sheet of BCH_3 under bending and the results of eigen-value analysis of a 3 by 3 pattern of BCH_3. (**a**) Sheet of BCH_3 deforms into a saddle-shaped under bending which is typical behavior for materials having a positive Poisson's ratio. (**b**) Twisting, (**c**) saddle-shaped and (**d**) rigid origami behavior (planar mechanism) of a 3 by 3 pattern of BCH_3 (with $a=1$; $b=2$; $\alpha = 60°$).
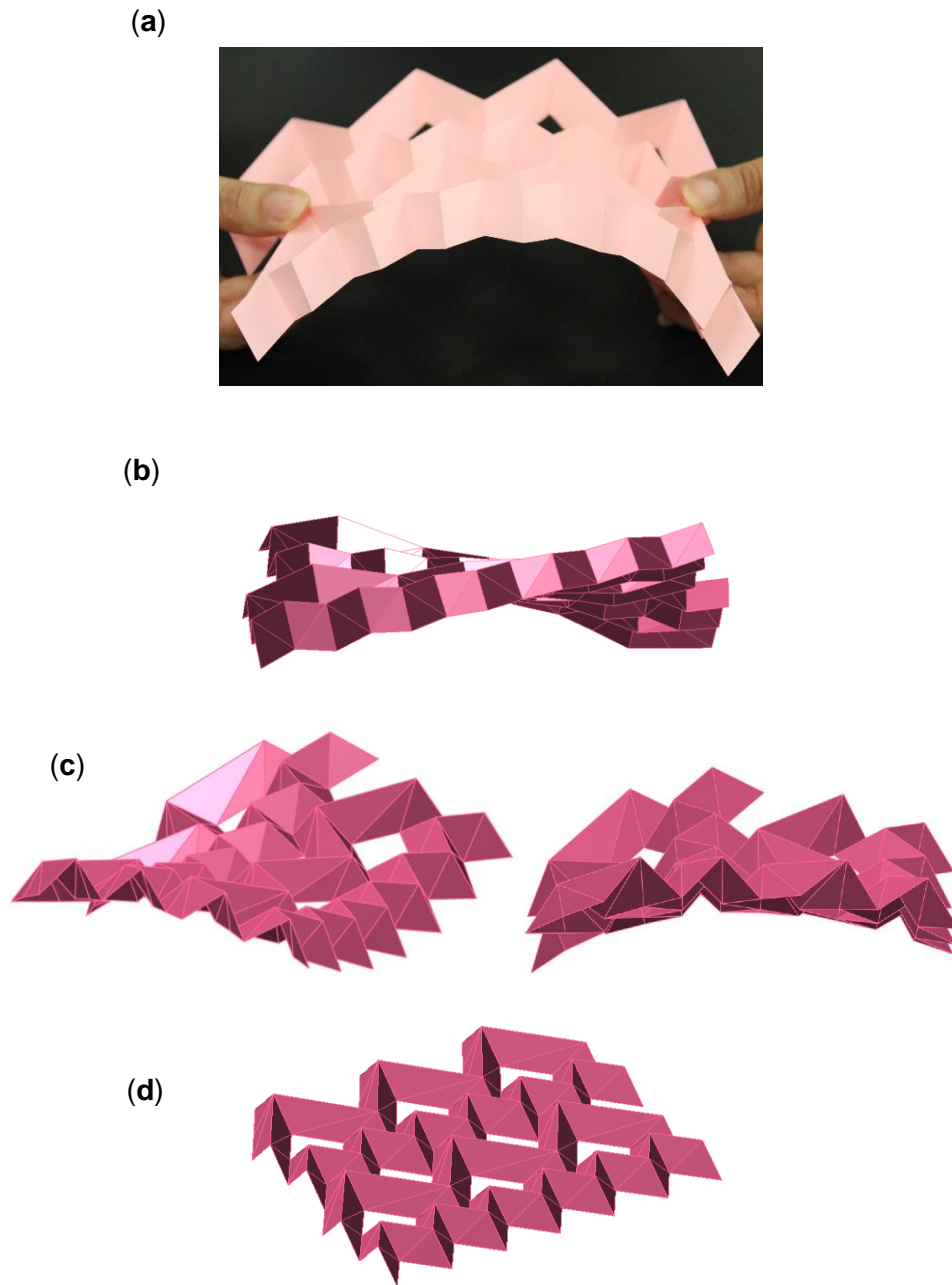
Figure 4.16: Behavior of a sheet of the pattern shown in Figure 4.3(c) under bending and results of eigen-value analysis of a 2 by 3 sheet of the pattern. (**a**) The sheet deforms into a saddle-shaped under bending (*i.e.*, typical behavior seen in materials having a positive Poisson's ratio). (**b**) Twisting, (**c**) saddle-shaped from two different views and (**d**) rigid origami behavior (planar mechanism) of a 2 by 3 pattern shown in Figure 4.3(c) (with $a=1$; $b=2$; $\alpha = 60°$).
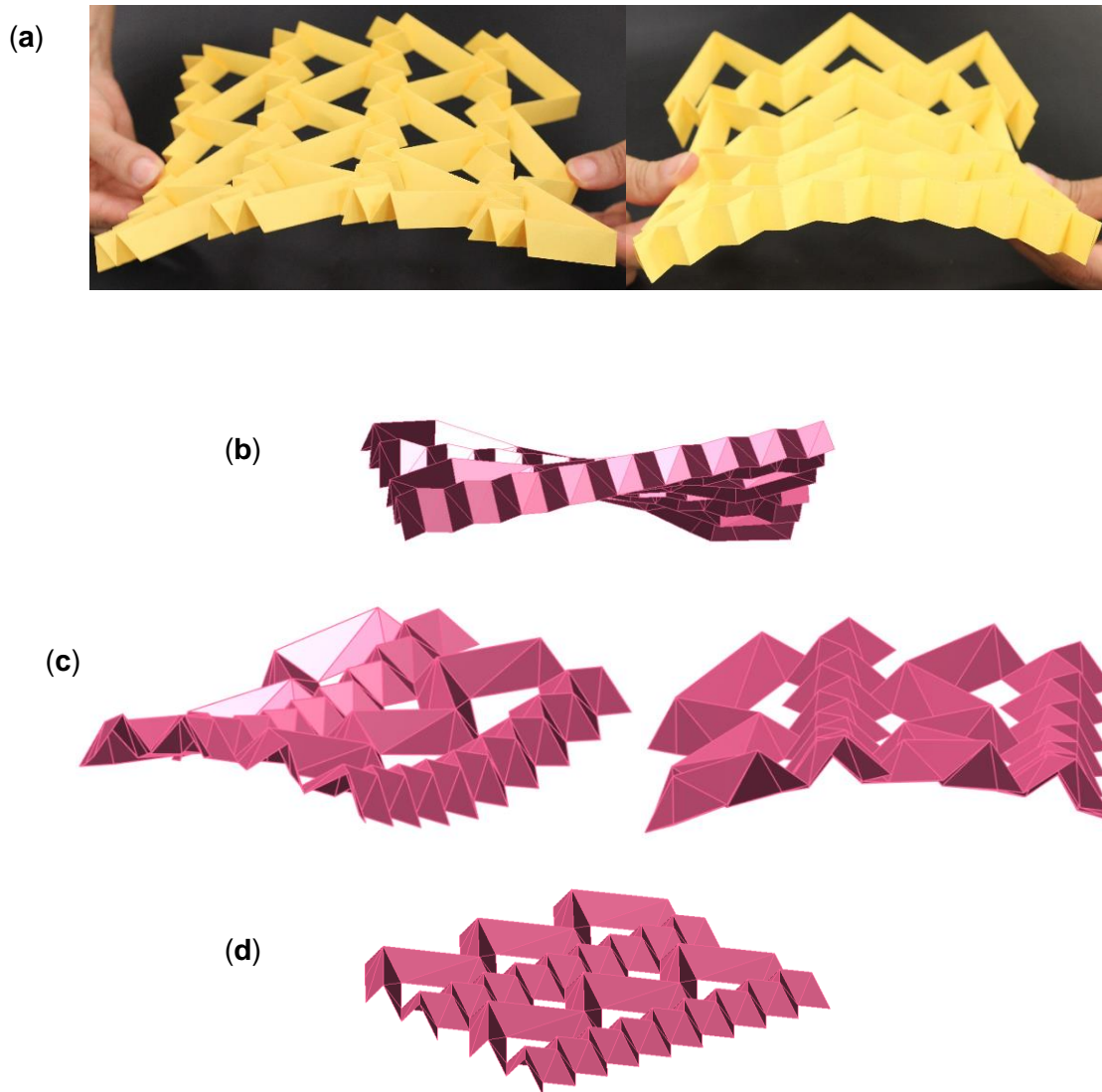
Figure 4.17: Behavior of a sheet of the pattern shown in Figure 4.3(d) under bending and the results of eigen-value analysis of a 2 by 3 sheet of the pattern. (**a**) The sheet deforms into a saddle-shaped under bending, *i.e.* a typical behavior seen in materials having a positive Poisson's ratio. (**b**) Twisting, (**c**) saddle-shaped from two different views and (**d**) rigid origami behavior (planar mechanism) of a 2 by 3 pattern shown in Figure 4.3(d) (with $a=1$; $b=2$; $\alpha = 60°$).

5

Tuning the Miura-ori Properties by Dislocating the Zigzag Strips

This chapter is adapted from an article authored by Maryam Eidini, in review [94].

Abstract

The Japanese art of turning flat sheets into three dimensional intricate structures, origami, has inspired design of mechanical metamaterials. Mechanical metamaterials are artificially engineered materials with uncommon properties. Miura-ori is a remarkable origami folding pattern with metamaterial properties and a wide range of applications. In this study, by dislocating the zigzag strips of a Miura-ori pattern along the joining ridges, we create a class of one-degree of freedom (DOF) cellular mechanical metamaterials. The resulting configurations are based on a unit cell in which two zigzag strips surround a hole with a parallelogram cross section. We show that dislocating zigzag strips of the Miura-ori along the joining ridges preserves and/or tunes the outstanding properties of the Miura-ori. The introduced materials are lighter than their corresponding Miura-ori sheets due to the presence of holes in the patterns. Moreover, they are amenable to similar modifications available for Miura-ori which make them appropriate for a wide range of applications across the length scales.

Keywords: Miura-ori; Poisson's ratio; auxetic; metamaterial; origami; kirigami; zigzag; herringbone.

5.1   Introduction

Miura-ori, a zigzag/herringbone-base origami folding pattern, has attracted substantial attention

in science and engineering for its remarkable properties [71, 95, 96, 97, 98]. The exceptional mechanical properties of the Miura-ori [97, 39], the ability to produce its morphology as a self-organized buckling pattern [71, 95] and its geometric adaptability [99, 100] has made the pattern suited for applications spanning from metamaterials [97] to fold-core sandwich panels [101]. Moreover, Miura-ori is a mechanical metamaterial with negative Poisson's ratio for a wide range of its geometric parameters [65, 78]. Mechanical metamaterials are artificially engineered materials with unusual material properties arising from their geometry and structural layout. In-plane Poisson's ratio is defined as the negative ratio of transverse to axial strains. Poisson's ratios of many common isotropic elastic materials are positive, i.e., they expand transversely when compressed in a given direction. Conversely, when compressed, materials with negative Poisson's ratio or auxetics contract in the directions perpendicular to the applied load. Discovery and creating of auxetic materials has been of interest due to improving the material properties of auxetics [89, 102, 103, 104]. Auxetic behavior may be exploited through rotating rigid and semi-rigid units [105, 106], chiral structures [107, 108], reentrant structures [109, 110, 111], elastic instabilities in switchable auxetics [112, 113], creating cuts in materials [114], and in folded sheet materials [97, 65]. The latter is the concentration of the current research.

Research studies have shown that the herringbone geometry leads to auxetic properties in folded sheet materials [97, 65] and textiles [115, 116], and its morphology arises in biological systems [75, 76, 117]. Due to possessing unprecedented deformability, the herringbone structure fabricated by bi-axial compression, has been also used in deformable batteries and electronics [118, 98, 119].

Kirigami, the art of paper cutting, has been applied in science and engineering as three dimensional (3D) core cellular structures and solar cells among others [64, 120, 121]. The current research expands on a recent study by Eidini and Paulino [65] where origami folding has been combined with cutting patterns to create a class of cellular metamaterials. In the present study, we use the concept of the Poisson's ratio of a one-DOF zigzag strip (i.e., $\upsilon_z = -tan^2\phi$) [65] which provides inspiration to tune and/or preserve the properties of the Miura-ori. In this regard, by dislocating the zigzag strips of the Miura-ori pattern along the joining fold lines, we create a novel class of metamaterials. The resulting configurations are based on a one-DOF unit cell in which two zigzag strips surround a hole with a parallelogram cross section.

5.2 Geometry of the Patterns

As shown in Figure 5.1, the arrangement of zigzag strips with offsets creates the parallelogram holes in the patterns.
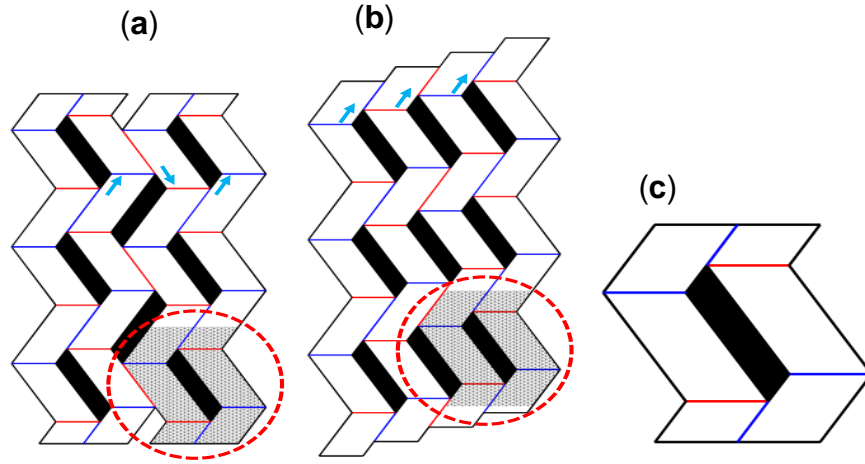
Figure 5.1: Crease patterns of sample zigzag-base folded materials introduced in the current work and their unit cell. (**a**) Changing the direction of the offset from a zigzag strip to the next adjoining one results in a pattern with holes oriented in different directions - the direction of the offsets are shown with blue arrows. (**b**) Arranging the offsets all to one side, results in zigzag strips with the holes all oriented with the same direction. (**c**) Crease pattern of the unit cell. In the figures, the blue and red lines show mountain and valley folds, respectively, and hatched black areas represent the places of the cuts.

The *Zigzag unit Cell with Hole* (ZCH) of the patterns is shown in Figure 5.1(c) and is parametrized Figure 5.2(a). The equations defining the geometry of the ZCH are given by

$$w = 2b\sin\phi \qquad \ell = 2a\frac{\cos\alpha}{\cos\phi} \qquad h = a\sin\alpha\sin\theta \qquad b_0 = (b - b_h)/2 \qquad (5.1)$$

The expression relating the angle ϕ and the fold angle θ is as follows

$$\tan\phi = \cos\theta\tan\alpha \qquad (5.2)$$

The outer dimensions of a regular sheet of ZCH (Figure 5.2(b)) are given by

$$W = m_2 \left(2b \sin \phi \right) \tag{5.3}$$

$$L_{ZCH} = m_1 \left(2a \frac{\cos \alpha}{\cos \phi} + 2 b_h \cos \phi \right) + \left(b - b_h \right) \cos \phi \tag{5.4}$$

If considered in the context of rigid origami, the ZCH is a one-DOF mechanism system. Sample patterns containing ZCH unit cells are presented in Figure 5.3, and the patterns have one DOF. We obtain the DOF of the patterns in this work using the approach mentioned in [65].
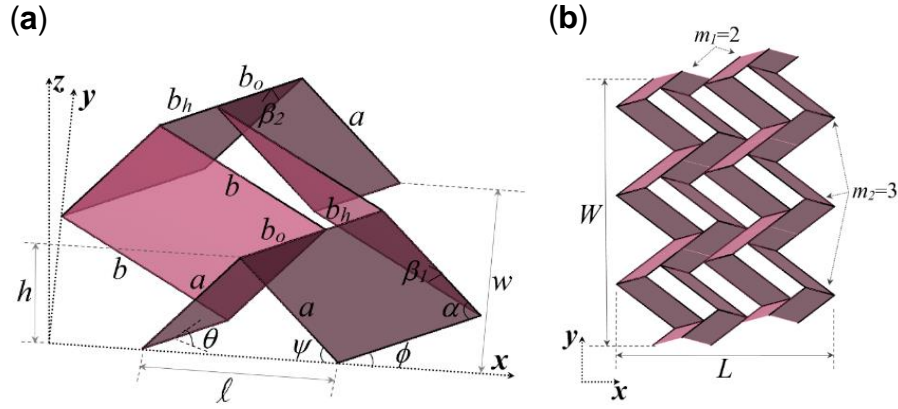
Figure 5.2: Geometry of ZCH pattern. (**a**) Geometry of the unit cell. The geometry of a ZCH sheet can be parameterized by the geometry of a parallelogram facet, hole width b_h, and fold angle $\phi \in [0, \alpha]$ which is the angle between the edges b_0 (and b) and the x-axis in the xy-plane. Other important angles in the figure are fold angle between the facets and the xy-plane, i.e., $\theta \in [0, \pi/2]$; angle between the fold lines a and the x-axis, i.e., $\psi \in [0, \alpha]$; Dihedral fold angles between parallelogram facets $\beta_1 \in [0, \pi]$ and $\beta_2 \in [0, \pi]$, joining along fold lines a and b_0, respectively. (**b**) A ZCH sheet with $m_1=2$ and $m_2=3$ and outer dimensions L and W.

5.3   Key Mechanical Behaviors of the Patterns

Being in the class of zigzag-base patterns with one-DOF planar mechanism, the patterns of ZCH shown in Figure 5.3 all have υ_z equal to $-tan^2 \phi$ [65]. Using the outer dimensions of the sheet, the Poisson's ratio of a regular ZCH sheet (for example, sample patterns shown in Figure 5.2(b) and Figure 5.3(a)) is given by

$$\left(\upsilon_{WL}\right)_{e-e} = -\frac{\varepsilon_L}{\varepsilon_W} = -\frac{dL/L}{dW/W} = -\tan^2\phi \frac{\eta\cos\alpha - \cos^2\phi}{\eta\cos\alpha + \cos^2\phi} \tag{5.5}$$

in which

$$\eta = \frac{m_1 a}{m_1 b_h + b_0} \tag{5.6}$$

In Equation (5.4), the dimensions of a repeating unit cell of the sheet are as follows

$$w = 2b\sin\phi \tag{5.7}$$

$$L_r = 2a\frac{\cos\alpha}{\cos\phi} + 2b_h\cos\phi \tag{5.8}$$

Hence, the Poisson's ratio of a repeating unit cell (in an infinite tessellation) is given by

$$\left(\upsilon_\infty\right)_{e-e} = \left(\upsilon_{L_r w}\right)_{repeating\,unit\,cell} = -\frac{\varepsilon_{L_r}}{\varepsilon_w} = -\frac{dL_r/L_r}{dw/w} = -\tan^2\phi\frac{a\cos\alpha - b_h\cos^2\phi}{a\cos\alpha + b_h\cos^2\phi} \tag{5.9}$$

The value given in the relation above presents the Poisson's ratio of a regular ZCH sheet for an infinite configuration as well (see Figure 4.4(a)). The value is positive if $a\cos\alpha < b_h\cos^2\phi$. The value is negative if $a\cos\alpha > b_h\cos^2\phi$. If $a/b_h \to \infty$, the Poisson's ratio of a repeating unit cell approaches υ_z. If $b/a \to \infty$, the Poisson's ratio of a repeating unit cell of the Miura-ori remains as $-tan^2\phi$, i.e., the υ_z (Figure 4.4(b)), but the Poisson's ratio of a repeating unit cell of ZCH approaches $tan^2\phi$. This phenomenon happens due to the existence of the holes in the ZCH patterns.

Upon bending, a ZCH sheet exhibits a saddle-shaped deformation (see Figure 5.6) which is a property for materials with positive Poisson's ratio [104]. Using the bar-framework numerical approach [97], the results of eigen-value analysis of sample ZCH patterns reveal similar behavior to those observed in Miura-ori and BCH$_n$ [97, 65] (see Figure 5.5 and Section 5.5 for more details).
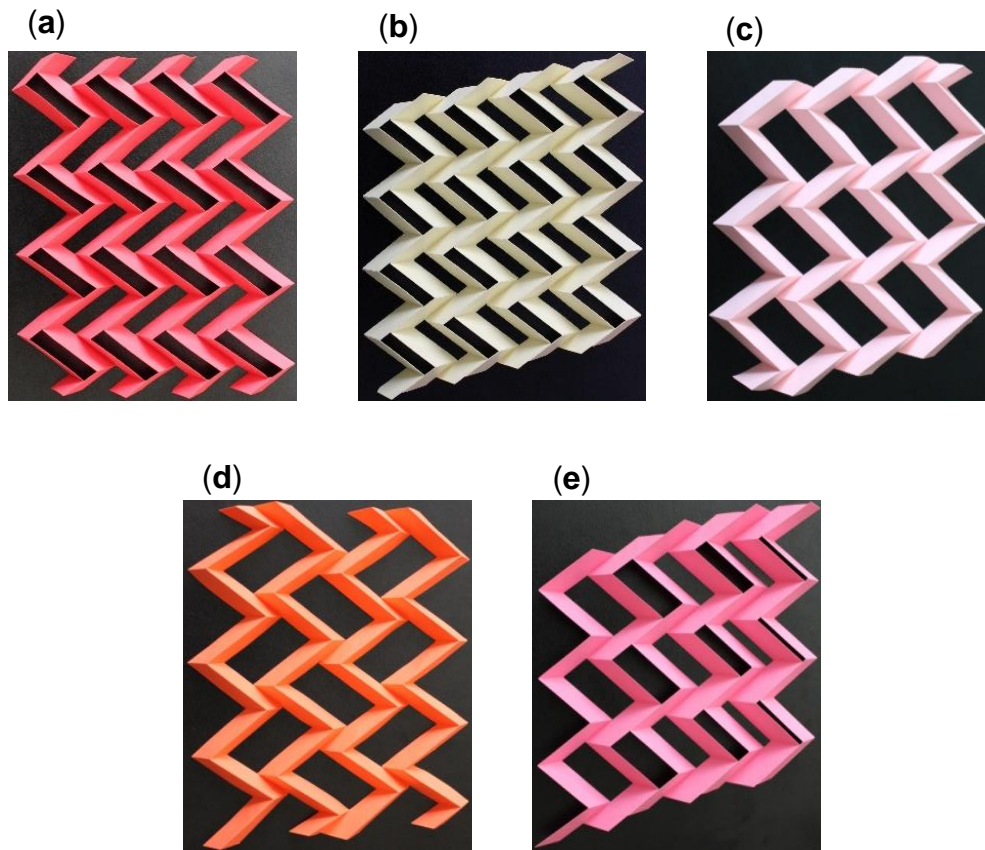
Figure 5.3: Sample patterns of ZCH. (**a**-**e**) Sample ZCH sheets created by changing the direction and/or the amount of the offsets, in placement of one zigzag with respect to its neighboring one, in the patterns. Note that by changing the height *h*, the length and width of the parallelogram facets, the hole width (pattern (e)) and other changes (e.g., similarly to the Miura-ori, changing the geometry of the facets to get the curved version and others) we can produce numerous graded and/or shape morphing materials/structures.
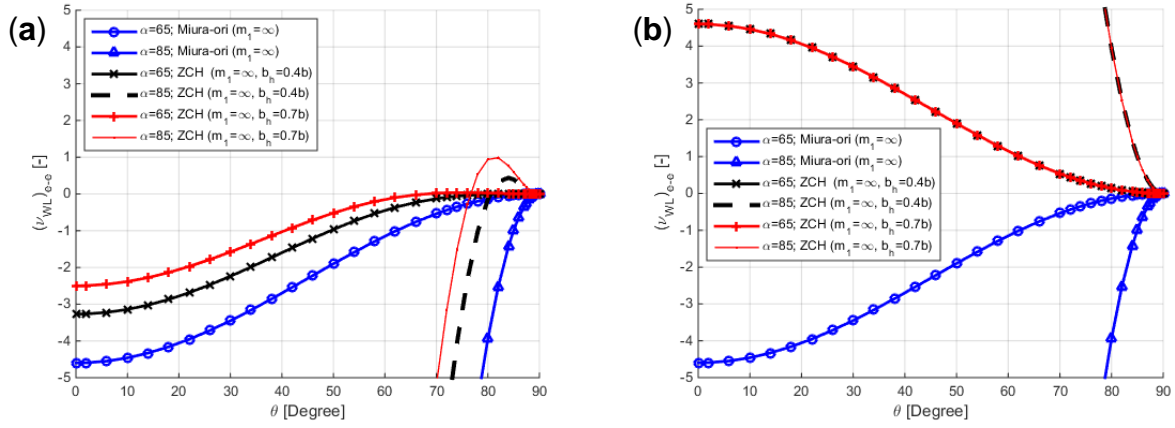
Figure 5.4: In-plane Poisson's ratio of metamaterials introduced in this work with infinite configurations. (**a**) Poisson's ratio of Miura-ori and ZCH sheets for ($m_1 = \infty$) and $a=b$, and two different hole widths - the values correspond to the Poisson's ratios of the repeating unit cells of sheets as well. (**b**) Poisson's ratio of repeating unit cells of ZCH and Miura-ori sheets if $b/a \rightarrow \infty$.
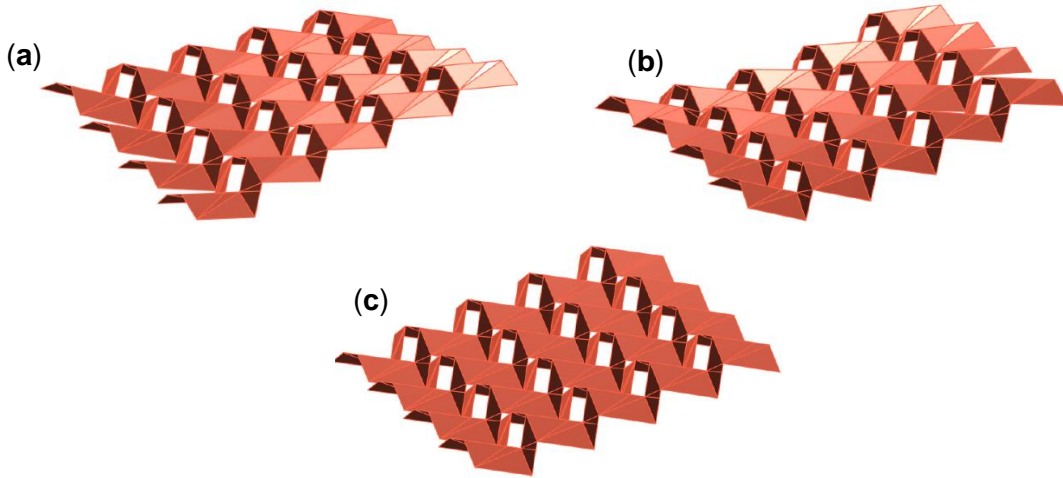
Figure 5.5: Results of the eigenvalue analysis of a sample ZCH sheet. (**a**) Twisting, (**b**) saddle-shaped and (**c**) rigid origami behavior (planar mechanism) of a 4x4 and a 4x3 patterns of ZCH with the holes located on various directions ($a=1$; $b=2$; $\alpha=60°$).

5.4 Concluding Remarks

In this study, we have presented a method to tune and/or keep the properties of the Miura-ori, i.e., the most remarkable origami folding pattern. The resulting configurations are zigzag-base

patterns which are flat-foldable, developable and 1-DOF systems. The main advantages of the patterns are highlighted as follows: (i) the patterns are amenable to similar modifications and/or applications available for the Miura-ori (e.g., [97, 63, 100, 122, 49] - see Figure 5.7 to Figure 5.9). (ii) Due to possessing holes in their configurations, they are less dense than their corresponding Miura-ori patterns (see Figure 5.10 to Figure 5.12). (iii) They extend geometrical and mechanical design space of the prior known zigzag-base patterns such as Miura-ori and BCH_2 (for example, see Figure 5.4). (iv) Despite existence of the holes, they are all single-degree of freedom (SDOF) systems for the rigid origami behavior. SDOF rigid mechanisms are appropriate for low energy, efficient and controllable deployable structures. (v) Compared with BCH_n patterns [65] whose unit cell includes two large and $2n$ small parallelogram facets, the unit cell of the patterns introduced in this work has identical number of facets on each side of the hole. Hence, they can be more appropriate than their corresponding BCH_n patterns when considering the thickness of the facets (e.g., when separate thick panels are connected with frictionless hinges [123]). (vi) For applications such as sandwich folded-cores, unlike *Zeta core* [68], the patterns remain developable by adding surfaces at the top and bottom of the patterns to increase the bonding areas (see Figure 5.7) - developable sheets are well-suited for continuous manufacturing techniques available for folded core structures. (vii) Dislocating the zigzag strips along the joining ridges makes the ZCH patterns appropriate for design of programmable materials and structures in which the directions and values (b_h) of the offsets can be adjusted depending on the external excitations.

In summary, the characteristics of the introduced patterns make them suitable for a broad range of applications from folded-core sandwich panels and morphing structures to metamaterials at various length scales.

5.5 Supplementary Materials

5.5.1 Out-of-plane behavior of the patterns

Upon bending, ZCH sheets exhibit saddle-shaped curvatures (Figure 5.6). The behavior is typically observed in materials with positive Poisson's ratio [104].
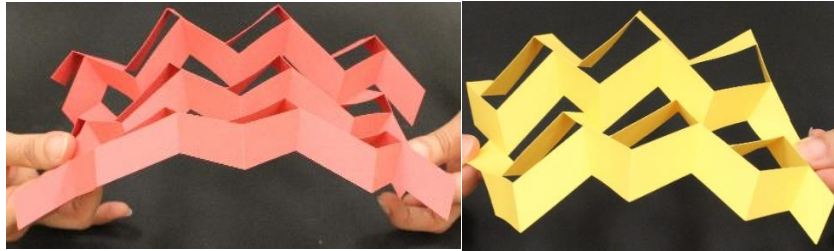
Figure 5.6: Behavior of sheets of the ZCH patterns under bending. ZCH Sheets deform into saddle-shaped curvatures under bending.

5.5.2 Other variations of ZCH and their assemblages

The variation of the ZCH pattern shown in Figure 5.7 provides additional bonding areas on the crests of the corrugation for applications as folded-core sandwich panels. Furthermore, by changing the geometry of the facets similarly to the curved version of the Miura-ori [122], we can create a curved version shown in Figure 5.8. In addition to the variations available for the Miura-ori (e.g., reference [99, 122]) which are applicable to these patterns, changing the hole width b_h (Figure 5.3(f)) and the width of the bonding areas at the crests (shown in Figure 5.7) combined with other changes can provide extensive versatility to create various variations/shapes from the patterns.

Figure 5.7: A developable ZCH pattern with augmented bonding areas.

Figure 5.8: A curved ZCH pattern.

Sample one-DOF cellular materials designed based on the ZCH patterns are shown in Figure 5.9. The stacked materials shown in Figure 5.9 (a) and (b) are appropriate for applications such as impact absorbing devices [49]. The interleaved ZCH tubular material shown in Figure 5.9(c) is similar to the one made from the Miura-ori pattern [63], which is a bi-directionally flat-foldable material. Its geometry results in a material which is soft in two directions and relatively stiff in the third direction. The samples shown in Figure 5.9(d) to Figure 5.9(f) are bi-directionally flat-foldable materials made from different assemblages of the ZCH tubes.
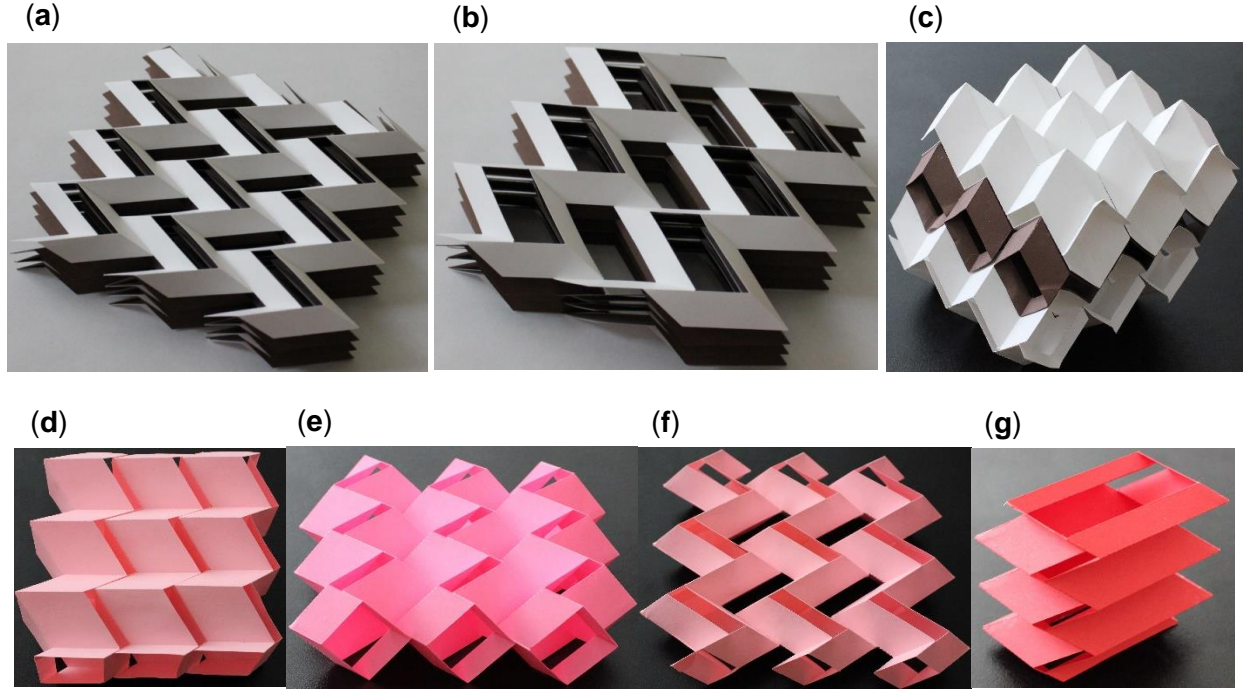
Figure 5.9: Cellular foldable metamaterials. (**a, b**) Stacked cellular metamaterials made from 7 layers of folded ZCH sheets. Each material includes two different geometries of similar sheets. (**c**) Interleaved ZCH tubular materials. (**d**-**f**) Materials made from various assemblages of ZCH tubes. (**g**) Sample ZCH tube with a parallelogram cross section.

5.5.3 Comparison of ZCH with Miura-ori and BCH2 for the same amount of mass

In this section, we compare the density of the ZCH with its corresponding Miura-ori and BCH$_2$ sheets (see Figure 5.10 for sample sheets). Knowing that widths and heights of the corresponding sheets are identical, the ratio of the density of the Miura-ori to that of the ZCH is given by

$$\rho_{Miura/ZCH} = \frac{V_{ZCH}}{V_{Miura}} = \frac{L_{ZCH}}{L_{Miura}} \tag{5.10}$$

Equation (5.4) in the main text gives the length of the ZCH sheet. Note that considering $b_h = 0$ in that relation, gives the length of the Miura-ori. Hence, the ratio of the length of the ZCH to that of the Miura-ori, i.e. $\rho_{M/Z}$, is equal to

$$\rho_{Miura/ZCH} = \frac{L_{ZCH}}{L_{Miura}} = \frac{m_1\left(2a\dfrac{\cos\alpha}{\cos\phi} + 2b_h\cos\phi\right) + (b - b_h)\cos\phi}{m_1\left(2a\dfrac{\cos\alpha}{\cos\phi}\right) + b\cos\phi} \tag{5.11}$$

Therefore, the relation above is equal to the ratio of the Miura-ori density to that of its corresponding ZCH sheet and is shown in Figure 5.11. Similarly, for BCH$_2$ we have (see Figure 5.12)

$$\rho_{BCH_2/ZCH} = \frac{L_{ZCH}}{L_{BCH_2}} = \frac{m_1\left(2a\dfrac{\cos\alpha}{\cos\phi} + 2b_h\cos\phi\right) + (b - b_h)\cos\phi}{m_1\left(2a\dfrac{\cos\alpha}{\cos\phi} + \dfrac{1}{2}b\cos\phi\right) + \dfrac{1}{2}b\cos\phi} \tag{5.12}$$

Working with the relation above, the length of the hole, $i.e.\ b_h$, at which the density of the ZCH is equal to that of the BCH$_2$ is given in the following.

$$b_h = \frac{b(m_1 - 1)}{2(2m_1 - 1)} \tag{5.13}$$

For the infinite configuration of the sheets ($i.e.$, $m_1 \to \infty$), the length of the hole at which the density of ZCH is equivalent to that of the BCH$_2$ is given by

$$b_h = \frac{1}{4}b \tag{5.14}$$

Consequently, for $b_h > 0.25b$, the ZCH is less dense than its corresponding BCH$_2$ sheet and for $b_h < 0.25b$, BCH$_2$ is less dense than its corresponding ZCH sheet.
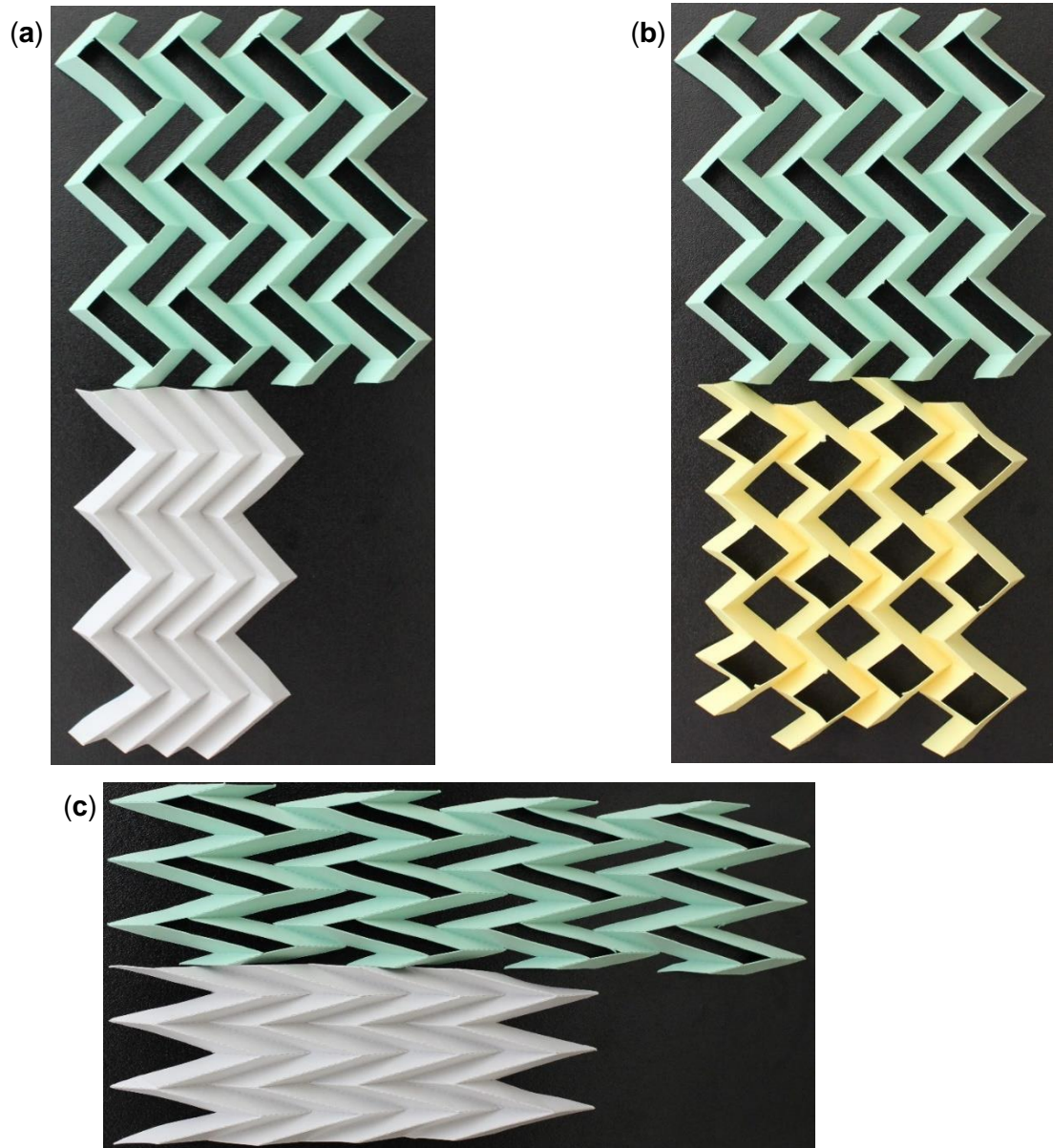
Figure 5.10: Sample ZCH with its corresponding Miura-ori and BCH$_2$ sheets. (**a**) A 4x3 ZCH sheet with its corresponding Miura-ori with $b=2a$, $\alpha=70°$ and $b_h= 0.3b$. (**b**) A 4x3 ZCH sheet with its corresponding BCH$_2$ sheet with $b=2a$, $\alpha=70°$ and $b_h= 0.3b$. (**c**) A 4x3 ZCH sheet with its corresponding Miura-ori with $b=2a$, $\alpha=30°$ and $b_h= 0.3b$.
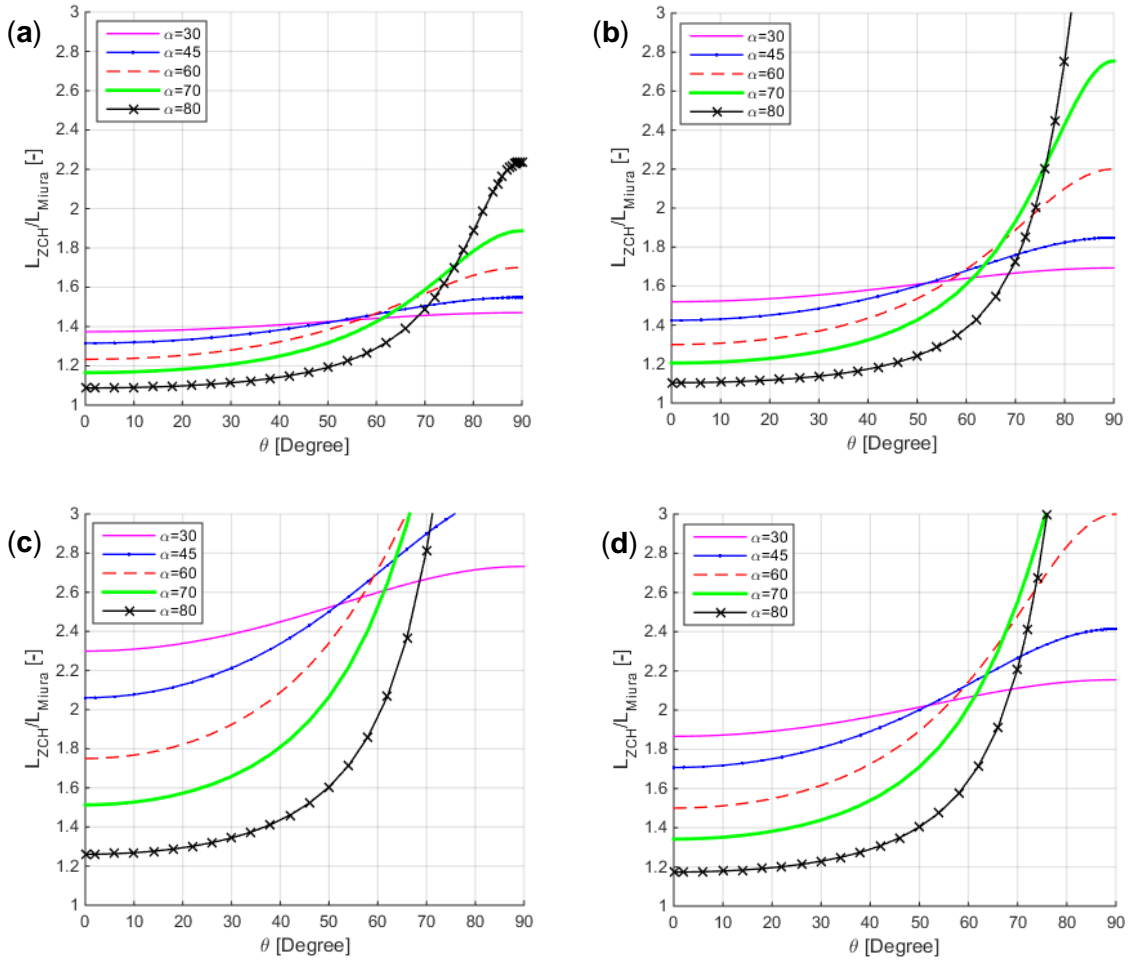
Figure 5.11: Density of ZCH compared with that of its corresponding Miura-ori. (**a**) m_1=4, b/a=2 and b_h=0.3b. (**b**) m_1=∞, b/a=2 and b_h=0.3b. (**c**) m_1=∞, b/a=5 and b_h=0.3b. (**d**) m_1=∞, b/a=2 and b_h=0.5b.
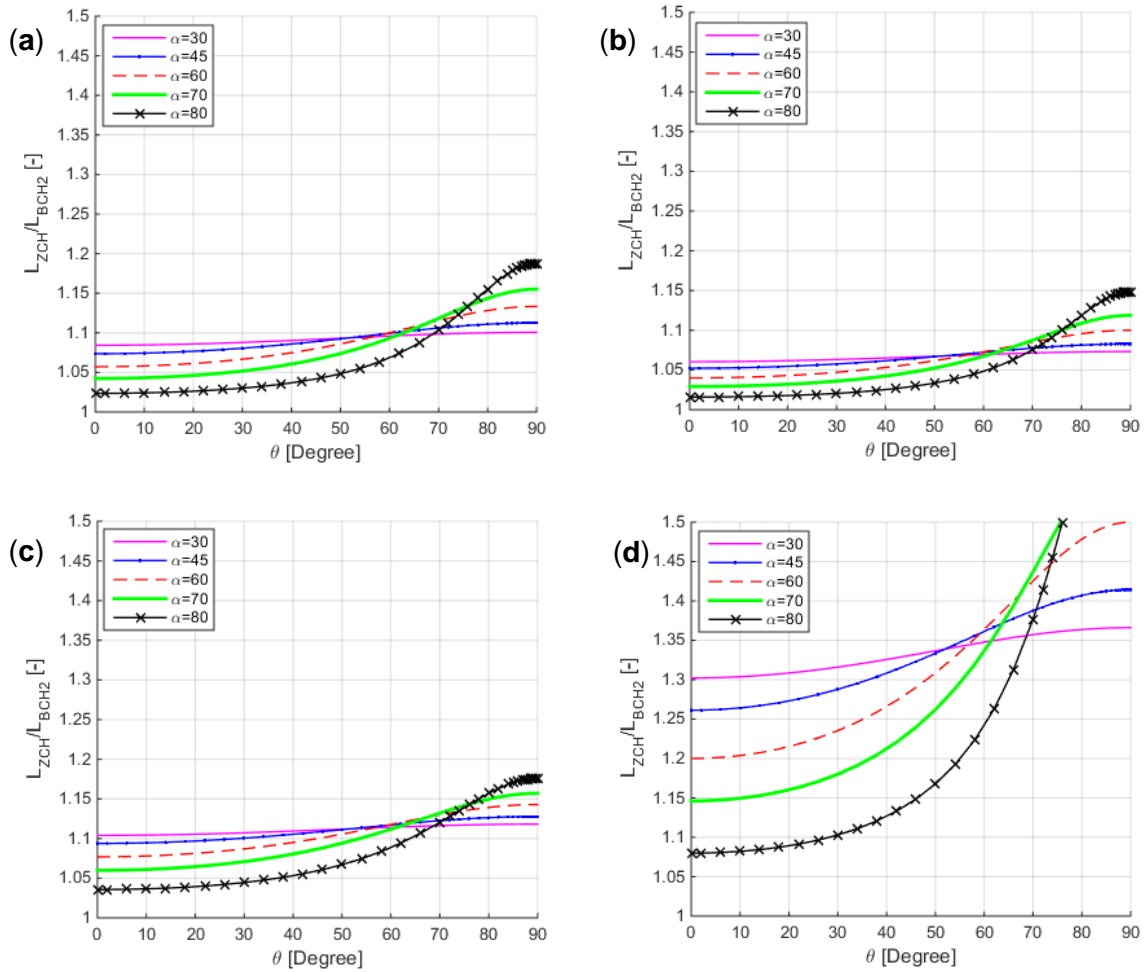
Figure 5.12: Density of ZCH compared with that of its corresponding BCH$_2$ sheet. (**a**) $m_1=4$, $b/a=2$ and $b_h=0.3b$. (**b**) $m_1=\infty$, $b/a=2$ and $b_h=0.3$b. (**c**) $m_1=\infty$, $b/a=5$ and $b_h=0.3b$. (**d**) $m_1=\infty$, b/a=2 and $b_h=0.5b$.

5.5.4 Global behavior of the patterns studied numerically

Using the bar-framework numerical approach [10], we perform eigen-value analyses of sample patterns shown in Figure 5.3 (a) and (b), by changing the ratio of the stiffness of the facet (K_{facet}) to that of the fold line (K_{fold}). We observe that, similarly to Miura-ori and BCH$_n$ zigzag-base patterns [10, 65], for small values of K_{facet}/K_{fold}, which cover a wide range of material properties, the twisting and saddle-shaped modes are the first and the second softest modes, respectively (Figure 5.5 (a) and (b)). That the second softest bending mode is a saddle-shaped deformation further shows that the material, constructed from a ZCH sheet, has a positive out-of-plane

Poisson's ratio (see Figure 5.5(b) and Figure 5.13). Moreover, the patterns exhibit rigid origami behavior (Figure 5.5(c)) for large values of K_{facet}/K_{fold} which is in accordance with our expectation.
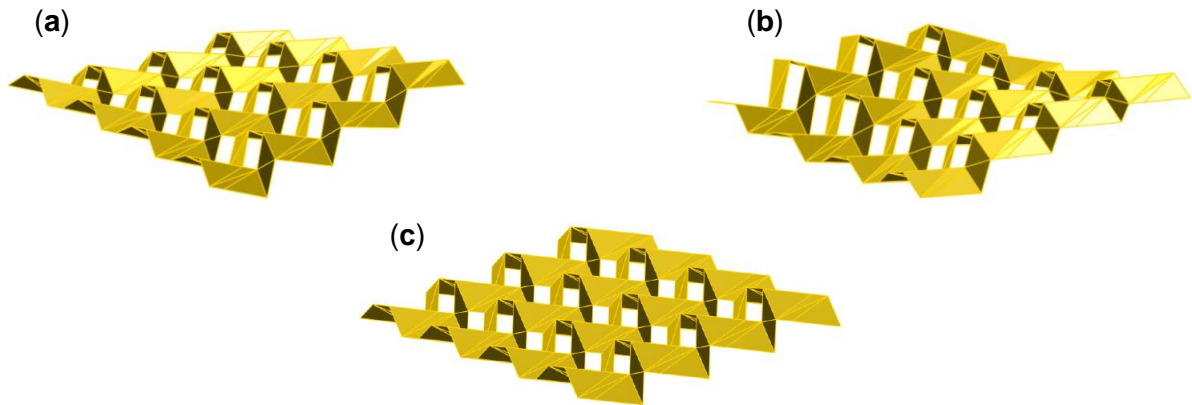
Figure 5.13: Results of the eigenvalue analysis of a sample ZCH sheet. (**a**) Twisting, (**b**) saddle-shaped and (**c**) rigid origami behavior (planar mechanism) of a 4x4 and a 4x3 patterns of ZCH with the holes located on the same directions (a=1; b=2; α=60°).

6 Lateral Force Distributions for Various Types of Hybrid Masonry Panels

This chapter is adapted from a 2011 article by Eidini and Abrams, published in *Proceedings of 11 NAMC conference* [124].

Abstract

This chapter summarizes computational analysis results carried out to study the distribution of lateral forces between a wall and a surrounding frame in hybrid masonry structural systems. Computational results of several multi-story, one-bay steel frames employing different types of hybrid masonry panels are presented. We use computational results to demonstrate differences in lateral-force distributions in hybrid masonry systems with different boundary conditions and with various panel aspect ratios as well as with different stiffness of the wall to that of the frame. This study is based on structural analyses using the hybrid masonry interfaces incorporated in the Bentley RAM Elements software. Findings presented in this study will help enhance understanding of the hybrid masonry behavior, and set the stage for large-scale experiments.

Keywords: Hybrid masonry, lateral force, aspect ratio, computational modeling, seismic.

6.1   Introduction

Hybrid masonry is a new technology for seismic design of structures, and was first proposed in 2007 [125]. Contrary to conventional masonry infilled frames which are usually treated as non-structural elements in design, the innovative hybrid masonry technology is based on the structural action of reinforced concrete masonry panels in combination with bounding steel frames as well as novel steel connectors where the panels including masonry wall, steel frame

and steel connectors are designed to resist lateral seismic forces. Depending on the boundary conditions between a masonry panel and a surrounding frame, hybrid masonry panels are categorized into three major groups namely hybrid Types I, II, and III. There are two more sub classifications for hybrid Types II and III. If a panel is resisting overturning moments by tensile force in vertical reinforcement, it is considered as Type IIa or IIIa. If it is resisting the overturning moments by bearing contact at the top and bottom of the panel and strut action, it is categorized as Type IIb or IIIb [126].

In this chapter, the effect of aspect ratio and wall stiffness on distribution of lateral load between a panel and a frame in various types of hybrid masonry panels is studied. Furthermore, the effect of story level on lateral load distribution is taken into account. Additionally, the effect of lateral load pattern using two different load patterns of inverse triangular and rectangular on the results is compared for the prototype frame described in the following section. This study was part of the NSF NEESR-CR: Hybrid Masonry Seismic Structural Systems research project [127].

6.2   Example Structure Considered in the Analyses

A four-story one-bay steel frame shown in Figure 6.1 under inverse triangular lateral load is considered for exploratory studies. The columns are W12x65, and the beams cross sections are W16x40. The thickness of the wall is 12 inches (30.48 cm). The frame employing five different types of hybrid panels including Type I, IIa, IIb, IIIa, and IIIb has been considered for one set of analyses. They are modelled using hybrid masonry interfaces of RAM Elements software [128] to study the effect of aspect ratio, and various boundary conditions on lateral load distribution. To evaluate the effect of wall thickness, one more set of analyses using the aforementioned hybrid panels, but with a thickness of wall equal to 6 inches (15.28 cm) has been carried out. All column heights (h) are 10 ft (3.048 m), and to generate the different aspect ratios only the frame bay width (L) has been changed in the models.
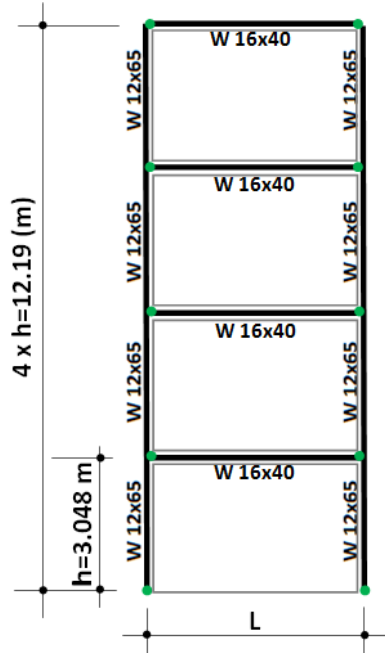
Figure 6.1: Four-story one-bay steel frame used in the analyses.

6.3 Lateral Load Transfer Mechanism in Hybrid Masonry Panels

The various interfacial conditions in hybrid masonry panels explicitly constitute the type of interaction between the frame and the masonry panel. This interaction is the main part in understanding the load transfer mechanism as well as in assessing the behavior of the panels. Pook and Dawe among others tested several large-scale infill panel specimens, and studied the influence of boundary conditions between a wall and a frame on behavior of infill systems. It was concluded that interface conditions significantly affected the initial stiffness and strength of the infill, and that the best overall performance was the case in which a panel is constructed in close contact with the moment-resistant frame without having either ties between the wall and the frame or separating them, for example using interfacial membrane [129, 130].

What presented in the following are the theoretical backgrounds and results aim at improving our understanding of the behavior of various types of hybrid masonry panels, with unknown structural behavior to us at the beginning of the present research. Furthermore, the results would be tempered through the course of the project and after having the results of the tests on several large-scale specimens as well as on steel connector plates [127].

6.3.1 Hybrid Type I

In hybrid Type-I, among all the actions, only shear force transfers to the wall, and there is no axial load transmission due to existence of gaps between the masonry wall and the frame as well as presence of slotted holes in the steel connectors. The transfer of story shear is through the steel links connecting the beam to the masonry wall. To have a continuous lateral load path there should be shear connectors at the interface of the wall and the beam below. In this kind of hybrid panel, steel connectors are acting in series with the masonry panel and the system of these two is performing in parallel with the bounding frame (see Figure 6.2). According to Figure 6.2, and considering that each connector plate is behaving like a cantilever beam, we have:

Lateral stiffness of each steel connector $= 3EI_{connectors} / h_{connectors}^3$

Lateral stiffness of wall $\approx 3EI_{wall} / h_{wall}^3$ (considering the wall base is fixed)

Therefore, the ratio of the lateral stiffness of the connectors to that of the wall is proportional to $(h_{wall} / h_{connector})^3$ which provides a large lateral stiffness ratio of the connectors to that of the wall even for small ratios of $(I_{connectors} / I_{wall})$.

Since the wall is connected to the steel connector plates in series (Figure 6.2(b)), and considering the large lateral stiffness ratio of the connectors to that of the wall, the stiffness of the system of the wall and connectors will be governed by the smaller lateral stiffness, i.e. lateral stiffness of the wall. Thus,

$$\frac{1}{K_{CW}} = \frac{1}{K_C} + \frac{1}{K_W} \tag{6.1}$$

For rigid connectors: $\qquad\qquad\qquad K_{CW} = K_W \tag{6.2}$

in which, K_{CW} is the lateral stiffness of the connectors and the wall acting in series; K_W is the lateral stiffness of the wall; K_C is the lateral stiffness of the connectors. Since K_W is much larger than K_{frame}, almost all lateral shear is attracted by the wall at each story level.

Based on the above-mentioned mechanism, the value of the shear at the story level i, V_i, and the

value of the axial load in each column at story level i, P_i, can be calculated by the following formula:

$$V_i = \sum_{j=i}^{n} F_j \qquad (6.3)$$

$$P_i = P_{i+1} + \left(\sum_{j=i+1}^{n} F_j \right) \frac{h_{i+1}}{L} \qquad (6.4)$$

where i is the story level index; n is the total number of stories; P_i is axial force due to lateral load in each column at level i; F_j is the lateral force at level j; h_{i+1} is the story height for the story level $i+1$; L is the bay width.

By substituting corresponding values for P_{i+2}, P_{i+3}, …, P_n in the above formula, one can get:

$$P_i = \sum_{k=i+1}^{n} \frac{V_k h_k}{L} \qquad (6.5)$$

where, V_k is the story shear in story level k, and h_k is the story height for the same story level. Hence, the overturning moment of the frame at level i is equal to:

$$\left(M_{Frame} \right)_i = \sum_{k=i+1}^{n} V_k h_k \qquad (6.6)$$
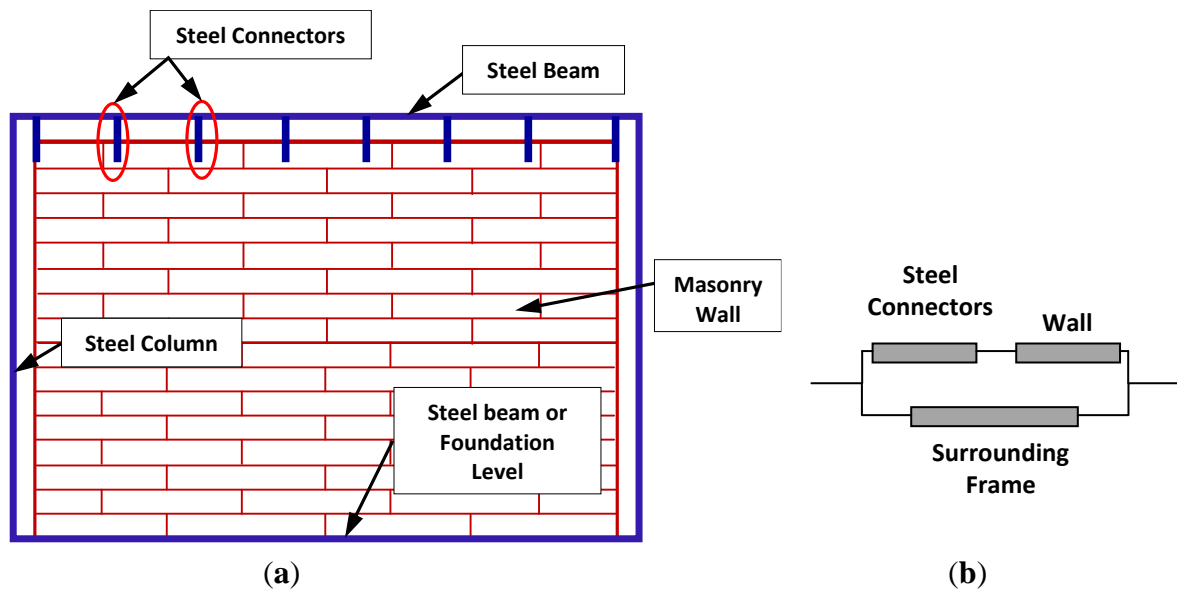
Figure 6.2: (**a**) Hybrid masonry panel Type I; (**b**) Schematic connection of elements in a hybrid masonry panel Type I.

A sample vertical stress distribution for hybrid Type I is shown in Figure 6.3(a). Flexural action of a masonry panel along a story height is evident by the pattern of vertical normal stresses. Type I hybrid panels, due to presence of slotted holes in the steel connector plates, do not transfer vertical forces from the top story to the bottom one. Hence, the vertical stresses are not continuous from one panel to another, as shown in Figure 6.3(a).

6.3.2 Hybrid Types II and III

In hybrid Type II, the wall is in contact with the beams, but there are gaps at the sides which prevent interaction of the wall with the surrounding frame. Also, in hybrid Type III similar to traditional infill panels, there is no gap between the wall and the frame, and the walls are constructed tight at the columns and the top of the wall. Moreover, Types a and b are sub categories for hybrid Types II and III. In hybrid Types IIa, and IIIa similar to hybrid Type I the reinforcing bars of the wall are welded to the beam below. Therefore, the contribution of the wall to the story overturning moment is through flexure of the reinforced section. However, in hybrid

Types IIb, and IIIb the contribution of the wall to the story overturning moment is a result of bearing and strut action of the panel. Sample contours of vertical stresses developed in the wall for the example structure employing hybrid panels Types IIa, and IIIa under a triangular lateral load pattern are shown in Figure 6.3 (b) and (c), respectively.

(**a**) Type I   (**b**) Type IIa   (**c**) Type IIIa
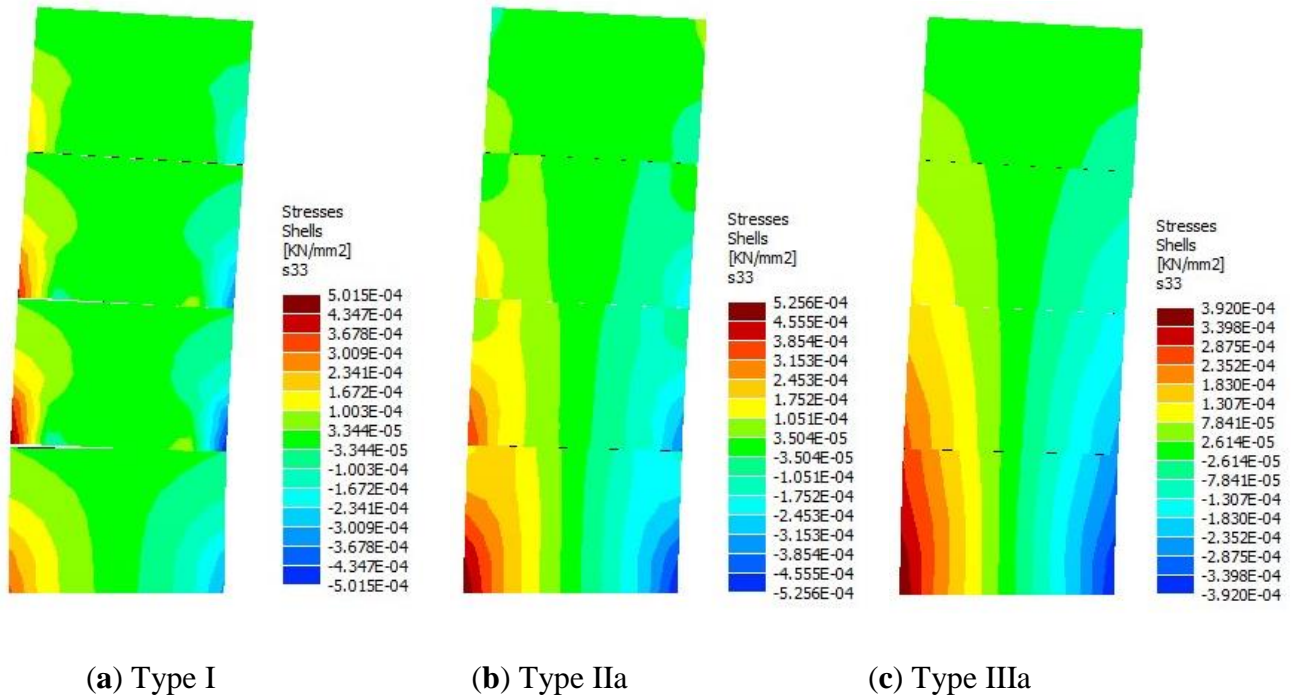
Figure 6.3: Sample vertical stress distribution for hybrid Types I, IIa and IIIa for the example frame with aspect ratio 1.5 under triangular lateral load pattern.

(**a**)   (**b**)
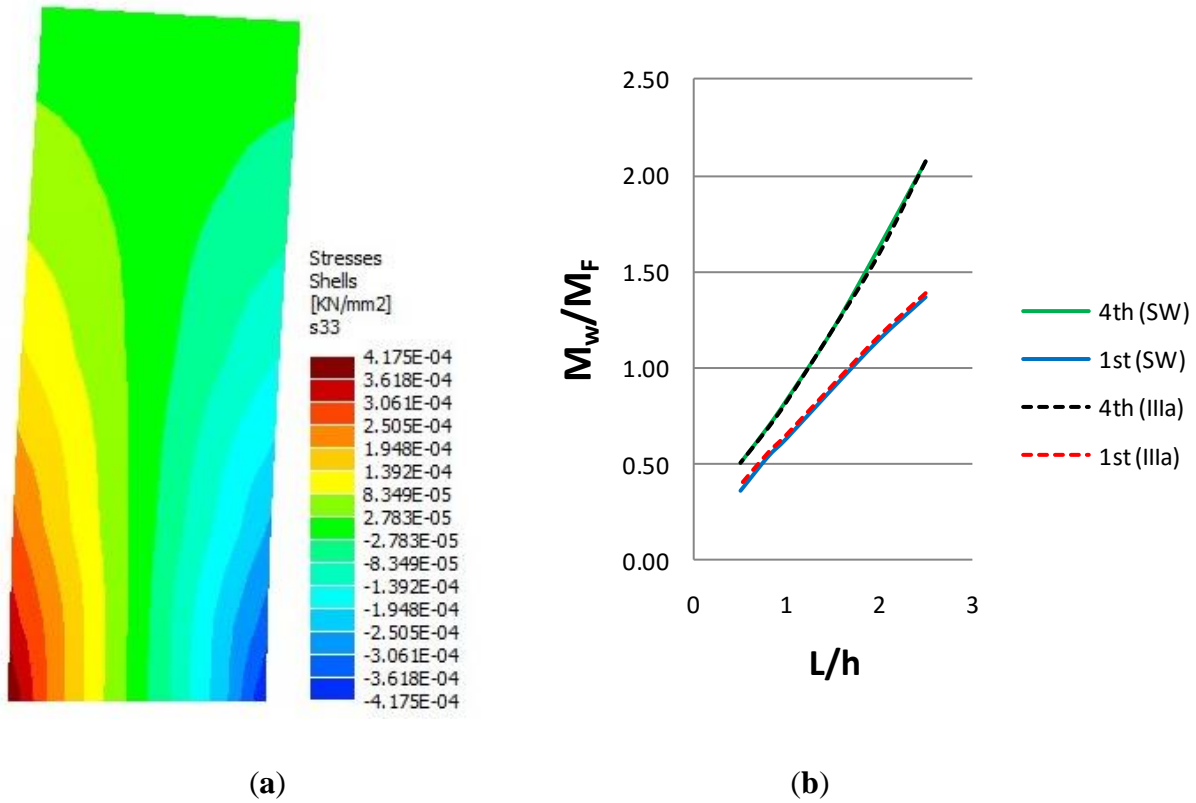
Figure 6.4: (**a**) Sample vertical stress distribution in shear wall system for the example frame with aspect ratio 1.5 under triangular lateral load pattern. (**b**) Ratio of overturning moment in the wall to that of the frame in the 1st and 4th stories for shear wall system and hybrid Type IIIa.

Figure 6.3(c) shows an essentially continuous vertical stress distribution in hybrid Type IIIa. Comparison of the vertical stress distribution in hybrid Type IIIa (Figure 6.3(c)), and shear wall (Figure 6.4) reveals the similarity of the behavior of these two lateral load resisting systems. Figure 6.4(b) illustrates the ratio of overturning moment in the wall to that of the frame in the 1st and 4th stories for both shear wall system and hybrid masonry Type IIIa. The results of both systems are well-matched, as shown in Figure 6.4(b).

6.4 Effect of Aspect Ratio and Wall Stiffness on Distribution of Lateral Force between Wall and Frame

To study the lateral load distribution in various types of hybrid masonry panels, several four-story one-bay frames employing hybrid masonry panels described in previous sections have been modeled using RAM Elements software [128]. The graphs presented in Figure 6.5 and Figure 6.6 are obtained from 54 such models. They show the effect of aspect ratio (frame bay to the story height), and wall thickness on contribution of the wall overturning moment to the story overturning moment as well as on the ratio of the wall overturning moment to that of the frame, respectively. In these studies, the structures are subjected to an inverse triangular lateral load pattern with the lateral load equal to 8.82 Kips (39.23 KN) at the top. Decreasing the wall thickness while keeping all other parameters unchanged has resulted in reduction of the wall contribution to the overturning moment which is in accordance with the expectations (see Figure 6.5 and Figure 6.6). Moreover, for the panels having the walls with thickness of 6 inches, similar behavior to those of the walls with thickness of 12 inches is observed (Figure 6.5 and Figure 6.6). For example, for hybrid panels Type II-a, III-a, and III-b for both thicknesses of 6 and 12 inches overturning moment in the wall increases by increasing the aspect ratio. Because, by increasing the aspect ratio, the axial load in columns decreases which will result in reduction of overturning moment in the frame and accordingly increasing the overturning moment in the wall.

For hybrid Type I, overturning moment in the frame at each story level is constant, and depends on both the story shear and geometry of the frame, as Equation (6.6) shows. Therefore, based on the formula overturning moment in the wall is constant as well. The results presented in Figure 5 obtained from RAM Elements also show that the overturning moment in the wall is constant for a wide range of aspect ratios. As discussed under "Hybrid Type I", the effect of K_{frame} has been disregarded. However, for small aspect ratios the assumption is not necessarily true. Therefore, some parts of the story shear will be resisted by the frame, resulting in a smaller shear in the wall, and consequently smaller overturning moment in the frame than that discussed earlier. Hence, in hybrid Type I, for small aspect ratios, the wall overturning moment is slightly greater than the value for large aspect ratios, as Figure 6.5 presents.

In hybrid Type IIIa, contrary to hybrid Type IIa, the masonry wall is in contact with the columns as well. Therefore, part of axial loads in the wall will transfer to the columns through the contact

length. For the same aspect ratio, maximum value of axial load in the columns of hybrid Type IIIa is greater than that of the corresponding columns of hybrid Type IIa. If all properties are the same, the relation between the maximum values of axial loads in columns of hybrid panels Type IIa and IIIa under lateral loading is as follows:

$$(P_{Col})_{III\,a} > (P_{Col})_{II\,a} \tag{6.7}$$

Hence,

$$(M_{Wall})_{III\,a} < (M_{Wall})_{II\,a} \tag{6.8}$$

The above relation shows that the wall contribution of overturning moment in hybrid Type IIa is greater than that of hybrid Type IIIa (See Figure 6.5 and Figure 6.6).
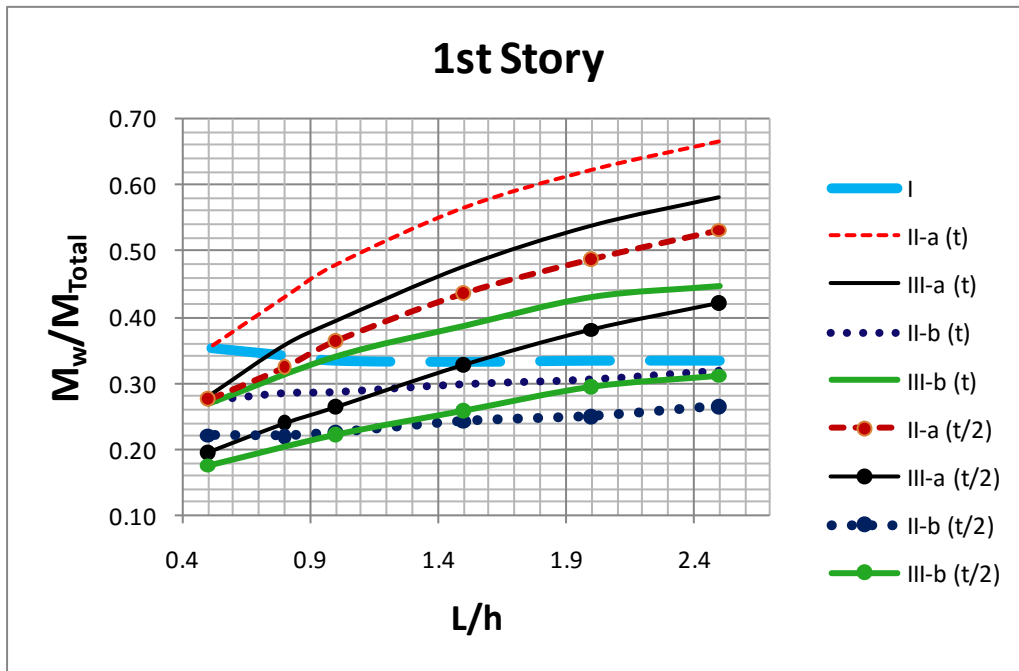
Figure 6.5: Wall contribution of story overturning moment in the first story for the frames with different aspect ratios in various types of hybrid panels for two different wall thicknesses.
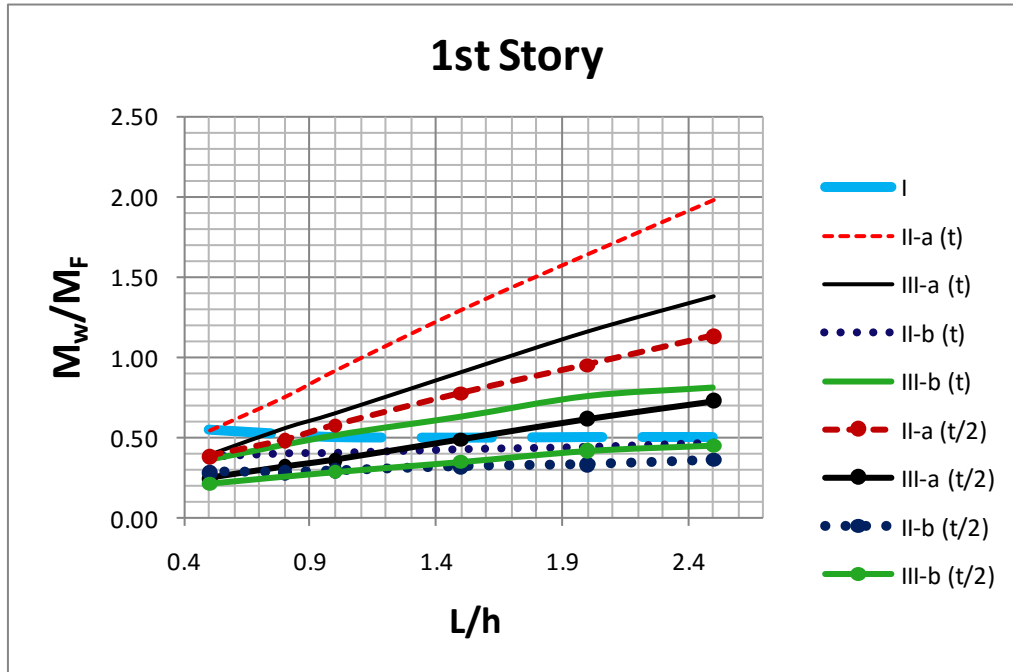
Figure 6.6: Ratio of wall contribution of story overturning moment to that of the frame contribution in the first story for the frames with different aspect ratio in various types of hybrid panels for two different wall thicknesses.

6.5 Effect of Story Level on Distribution of Lateral Force between Wall and Frame

In this section, the distribution of lateral load between the wall and the frame of hybrid masonry Types I, IIa, and IIIa at different stories are studied. The results are summarized in Figure 6.7-Figure 6.9. As illustrated in the figures, the ratio of the wall contribution of the overturning moment to that of the frame is increasing in upper stories. This trend is similar to that found in a shear wall. Specifically, the results obtained in hybrid Type IIIa (Figure 6.9) are in very close agreement with the results obtained from the shear wall system (Figure 6.4(b)). This similarity is due to the continuity of the lateral load path between the wall above and the one below a beam in hybrid Type IIIa systems.
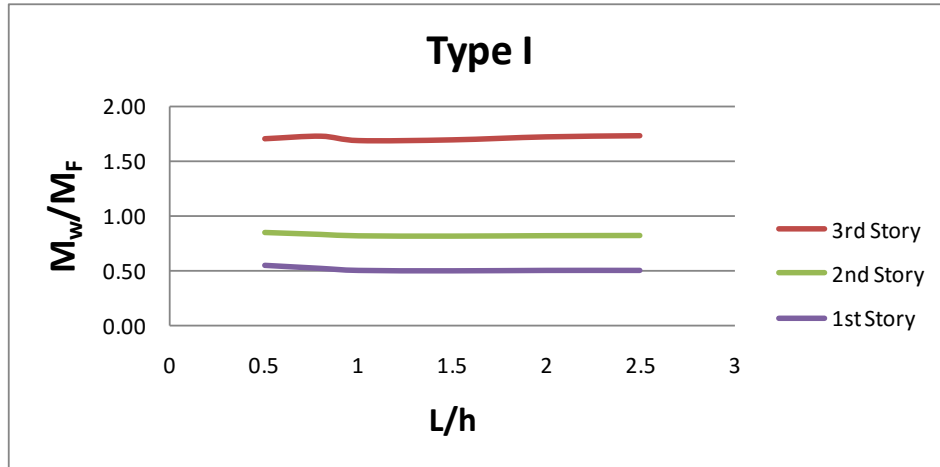
Figure 6.7: Wall contribution to story overturning moment in different stories for the frames with different aspect ratio in hybrid Type I.
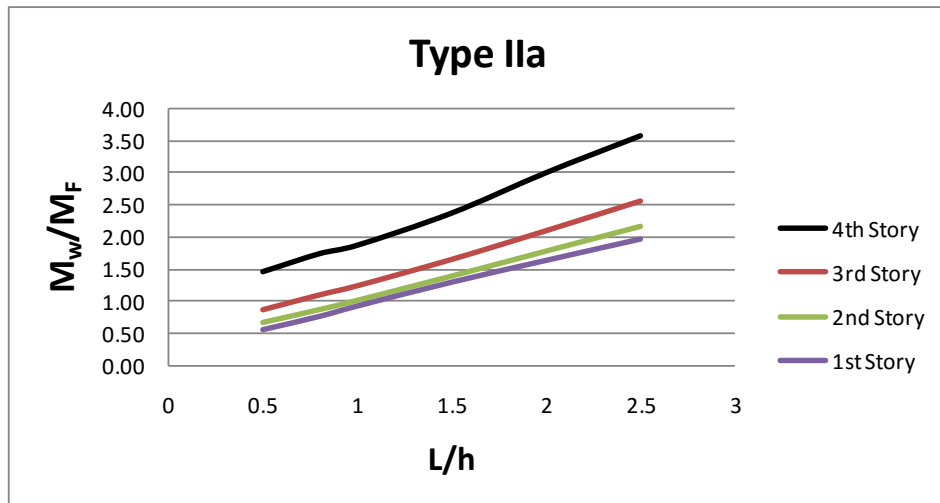
Figure 6.8: Wall contribution to story overturning moment in different stories for the frames with different aspect ratio in hybrid Type IIa.
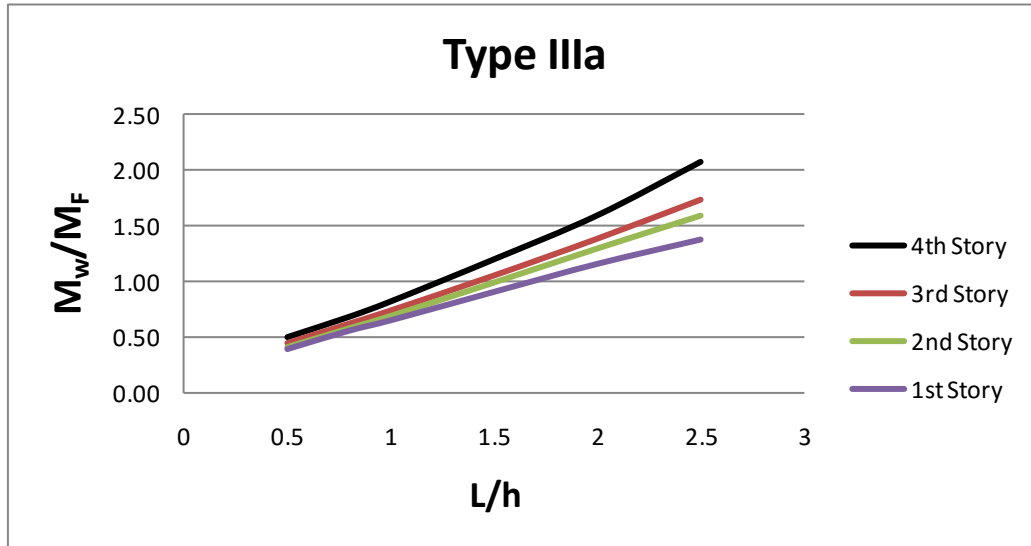
Figure 6.9: Wall contribution to story overturning moment in different stories for the frames with different aspect ratio in hybrid Type IIIa.

For hybrid Types IIa and IIIa, the ratio of the wall overturning moment to that of the frame at all stories increases, as the aspect ratio increases (see Figure 6.8 and Figure 6.9). This fact is due to the reduction of axial load in columns as discussed earlier.

6.6   Effect of the Lateral Load Patterns on Distribution of the Lateral Forces between Wall and Frame

To evaluate the effect of lateral load distribution pattern on distribution of lateral forces between a frame and a wall in hybrid masonry systems, the response of the example frame employing different types of hybrid panels with various aspect ratios subjected to a rectangular lateral load pattern is compared in Figure 6.10 with the behavior of the corresponding hybrid systems subjected to an inverse triangular lateral load. To have a rational comparison on the effect of lateral load patterns, the rectangular load pattern has been chosen so that the sum of lateral loads is equal to that of the triangular load pattern. Additionally, the comparison has been made for the first story for which the story shear is the same in both lateral load patterns. The value of the lateral load in rectangular load pattern at all levels is equal to 5.51 Kips (24.52 KN).

For rectangular load pattern, the ratio of overturning moment in the wall to that of the frame (M_w/M_f), at the first story is greater in hybrid masonry panels Types I and IIa than their corresponding values for the triangular load pattern, as presented in Figure 6.10. However, the ratio of M_w/M_f at the first story is essentially identical, in hybrid masonry panels Types IIb, IIIa, and IIIb, for both lateral load distribution patterns. Nevertheless, to generalize these results more studies need to be done considering the effects of other parameters such as relative stiffness of the frame to that of the wall, effect of story level and so on. Moreover, similar to the results found in previous sections, the wall participation to the overturning moment in hybrid Types IIa, IIIa, and IIIb subjected to a rectangular lateral load pattern increases as the aspect ratio increases.
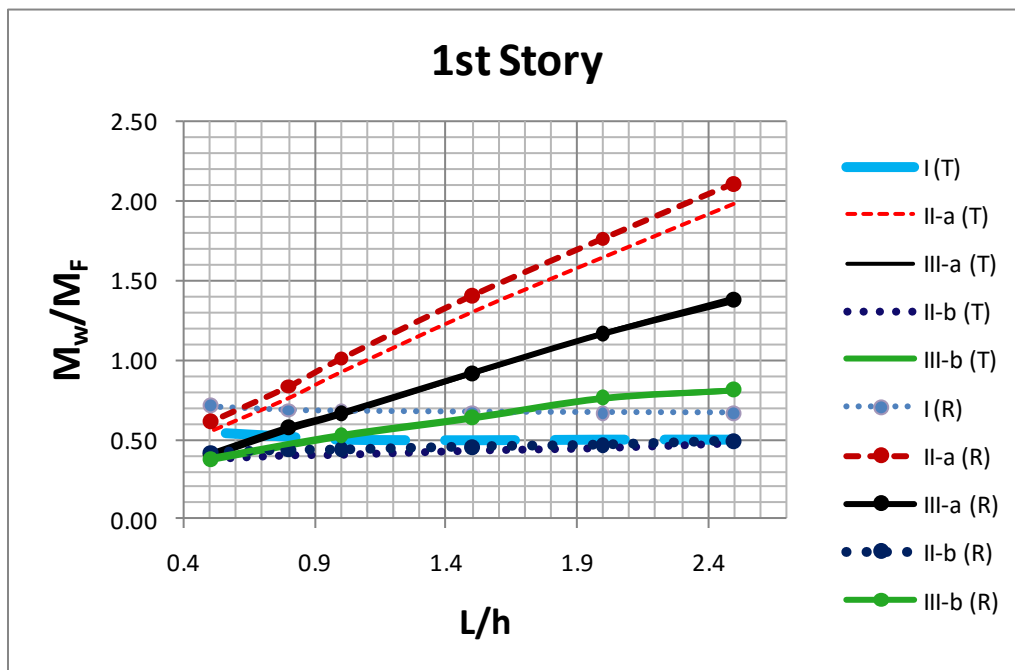
Figure 6.10: Effect of Triangular (T), and Rectangular (R) lateral load pattern on distribution of lateral forces between the wall and frame in hybrid masonry panels.

6.7   Concluding Remarks

Hybrid masonry technology includes the structural action of reinforced concrete masonry panels

in combination with surrounding steel frames as well as novel steel connectors. One of the advantages of the system includes: the bracing of a steel frame by the use of reinforced masonry panels will lead to an integrated, efficient application of both materials. This research summarizes the results of exploratory studies performed to improve understanding of the behavior of various types of hybrid masonry panels. Particularly, the chapter's focus is to understand the effect of aspect ratio and relative stiffness of the wall to that of the frame as well as the effect of lateral load pattern on lateral load distribution in various types of hybrid masonry panels. The main results obtained through this study are listed as follows:

- For hybrid Type I, overturning moment in both the wall and the frame is constant for various aspect ratios, and the ratio of the wall to the frame contribution is dependent on the system geometry and applied lateral load pattern.

- Comparison of the vertical stress distribution in hybrid Type IIIa, and shear wall reveals very close similarity of the behavior of these two lateral load resisting systems. In addition, the study of contribution of the overturning moment in the wall and the frame in both shear wall and hybrid masonry Type IIIa systems shows that the behavior of these two lateral load resisting systems are very close to each other.

- In hybrid Types IIa, IIIa, and IIIb at all story levels, wall contribution of overturning moment increases with increasing aspect ratio, and having all other parameters unchanged. Frame contribution to overturning moment decreases with increasing aspect ratio. Axial load in columns decreases with increasing aspect ratio in all three aforementioned hybrid panels.

- In hybrid panels Type I, IIa, and IIIa wall contribution to story overturning moment increases at higher story levels. This behavior is similar to the behavior of the shear walls.

- The wall contribution to overturning moment in hybrid panel Type IIa is greater than that in hybrid panel Type IIIa, if all the properties and lateral loading in both panels are the same. This is mainly due to the fact that the axial load is smaller in columns of hybrid Type IIa which will accordingly lead to a greater overturning moment in the wall of hybrid panel Type IIa.

- To understand the behavior of the panels in hybrid Types IIb and IIIb, and rationalize the

findings in this chapter for these types of hybrid panels more research needs to be performed.

7   Seismic Design and Viability of Hybrid Masonry Building Systems

This chapter is adapted from a 2013 article by Eidini et al., published in *ASCE Journal of Structural Engineering* [131].

Abstract

Hybrid masonry is an innovative technology for seismic design of buildings. The system utilizes reinforced masonry panels within a steel-framed structure, where steel connector plates link the steel frame to the masonry panels. The system has been used for construction of low-rise buildings in the low-seismic regions of the eastern and mid-western United States, but has not been implemented in regions of moderate or high seismicity yet. Current research is underway to extend the application of hybrid masonry for use in high-seismic regions. In this chapter, the overall approach for seismic design of one type of hybrid masonry systems is studied and the steps of a capacity design process are presented, where two favorable ductile modes of behavior may be exploited: steel connector plates behaving as fuses or flexural yielding of the masonry panels. Moreover, this research applies the two design options for three, six, and nine-story prototype buildings located in a high seismic region, and evaluates viability of hybrid masonry as a new seismic lateral-load resisting system. Based on this design framework and the exploratory studies, both approaches are shown to be feasible for developing realistic system configurations. Nevertheless, for the case of flexural yielding of the masonry panels, the steel connector plates must carry significant shear force demands. The structural system then requires more hybrid panels compared with corresponding systems when plasticity is concentrated in the steel connector plates.

7.1 Introduction

Hybrid masonry, which was first proposed in 2007 [125], is an innovative lateral-load resisting system that synergistically combines masonry panels and a steel frame. As mentioned by Bertero and Broken [132], the key principle for seismic resistant design is to use the necessary mass in the system to resist seismic forces. Hybrid masonry takes advantage of masonry walls present in most buildings as non-structural elements (*i.e.*, the necessary mass) and uses special details to make them part of the lateral-load resisting system. Unlike common masonry infill panels, the innovative aspect of hybrid masonry panels is the intentional detailing of the connections between the masonry panels and the steel frame such that predictable, robust and ductile behavior is ensured. Additionally, reinforced masonry panels are used in the system, rather than unreinforced as are commonly used in masonry infill walls.

The presence of masonry panels in hybrid masonry systems changes the lateral-load transfer mechanism of the structure from predominantly frame or truss action, depending on whether the steel frame is unbraced or braced, to a combined truss-shear wall action. Since most low-rise steel buildings are braced frames, the masonry panels can be viewed as surrogate bracing elements. Based on the boundary conditions between masonry panels and the surrounding steel frame, hybrid masonry systems are categorized into three major groups: Types I, II, and III (NCMA TEK 14-9A 2009) [126]. This research focuses on hybrid masonry Type I, which will be discussed in more detail below.

Hybrid masonry construction has been introduced to the eastern United States for low-rise office and commercial buildings, and it has been found to reduce cost and expedite construction since structural and architectural components can be integrated. However, it has not been used in regions of high seismicity yet. The research described in this chapter is part of a comprehensive effort to characterize the inelastic behavior of hybrid masonry and develop design methods so that it can be implemented in high seismic regions.

Since the system is new, research on hybrid masonry is in its infancy. Sample construction details of hybrid masonry panels are provided by the National Concrete Masonry Association (NCMA TEK 3-3B 2009) [133]. An overview of current research on hybrid masonry panels is given in [127]. Eidini and Abrams [124] performed an exploratory study on distribution of lateral

forces between a masonry panel and a frame using models of four-story, one-bay steel frames employing different types of hybrid masonry panels. The effects of various parameters such as panel aspect ratio and lateral-load distribution pattern were taken into account. Johnson et al. [134] performed an experimental study to establish the strength and hysteretic behavior of connector plates, and to develop ductile energy dissipating fuse connector plates for use in hybrid masonry Type I systems. They tested the connector plates under cyclic lateral loading, and developed steel connectors and ductile fuses with various geometric configurations. Further research on development and design of steel connector plates for use in hybrid masonry structural systems can be found in Goodnight et al. [135] and Ozaki-Train and Robertson [136].

The purpose of this research is to establish a framework for the application of hybrid masonry to construction in areas of moderate and high seismicity. The main contribution of this study is to present simplified formulas for lateral-load analysis of hybrid masonry Type I, as well as to provide systematic approaches for seismic design of hybrid masonry as efficient lateral-load resisting systems. The design methodologies presented in the chapter are based on the widely accepted capacity design approach [137].

In addition, application of the proposed approaches is used in an exploratory parametric study, which is done to evaluate the viability of hybrid masonry Type I. The current study precedes a large-scale experimental program and computational studies as discussed in [127]. There are no provisions in current codes that define seismic response factors [138], such as the response modification coefficient (R) and the system over-strength factor (Ω_0) for hybrid masonry systems. Hence, in the portion of this study on evaluating feasibility of these systems, the demands on the structural elements are calculated assuming a range of likely values for these currently-undefined seismic design parameters. The values for these parameters are assumed based on the current code provisions [138] for systems with similar behavior.

This chapter focuses on hybrid masonry Type I and is organized as follows. Hybrid masonry Type I and its lateral-load transfer paths are discussed in the next section. Seismic design procedures are then presented for buildings incorporating hybrid masonry Type I. Using the proposed design methodologies, viability of hybrid masonry building systems is investigated for use in high seismic regions. The last section provides some concluding remarks and areas for

further research.

7.2 Hybrid Masonry Type I

7.2.1 Force transfer mechanisms

In general for hybrid masonry systems, a reinforced concrete masonry panel is attached to a structural steel frame such that gravity forces, story shears and overturning moments can be transferred to the masonry. Type I is the simplest form of hybrid masonry since only horizontal shear force transfers from the steel frame to the top of each panel. As shown in Figure 7.1(a), there is no axial load transmission due to gaps between the top of the masonry panel and the frame and vertically slotted holes in the steel connectors. A steel connector comprises two steel connector plates, one on each side of the masonry panel, and a through bolt. Hence, a masonry panel at a level functions as an isolated shear wall and vertical stresses in the masonry are not continuous over the height. The transfer of story shear is through the steel connectors attaching the beam to the masonry panel. The structural masonry panel acts as a lateral bracing member and can be reinforced both vertically and horizontally to resist lateral forces and to develop the deformation capacity of a well-detailed reinforced masonry shear wall. To prevent sliding of the masonry panel and to provide a continuous lateral-load path there must be adequate connections at the interface of the masonry panel and the supporting beam below.

In hybrid masonry Type I, steel connectors are acting in series with the masonry panel and the system of these two elements is acting in parallel with the surrounding frame (see Figure 7.1). Steel connectors are shown schematically in this figure, but realistic details are achieved by attaching to both flanges of the beam above with a combination of welds and bolts. The robustness of this configuration permits the connection between a connector and the beam to be idealized as fixed. Therefore, each connector plate is behaving like a cantilever beam, and the lateral stiffness of a steel connector with constant cross section is $K_{CP}=3\ E_SI_{CP}/L_{CP}{}^3$, where, E_s is the modulus of elasticity of steel; I_{CP} is the moment of inertia of a steel connector; L_{CP} is the length of a connector. In addition, the lateral stiffness of a cantilever panel is [139] $K_{pa}{\approx}bE_m/[4(h_{panel}/L_{panel})^3+3(h_{panel}/L_{panel})]$ where E_m is the modulus of elasticity of masonry; h_{panel} is the height of the panel; b is the net thickness of the panel; L_{panel} is the length of the panel.

Therefore, since the panel is connected to the steel connectors in series (Figure 7.1(b)), the stiffness of the system of the panel and connectors will be:

$$K_{CPa} = K_C K_{Pa} / (K_C + K_{Pa}) \qquad (7.1)$$

where K_C is the lateral stiffness of the steel connectors (equal to the lateral stiffness of each steel connector, K_{CP}, multiplied by the number of connectors per panel, N_{CP_panel}) and K_{Pa} is the lateral stiffness of the panel. Since the total stiffness in such a series system is dominated by the more flexible element, the connector plates in hybrid masonry Type I, which are much more flexible than the masonry panels, play an important role.
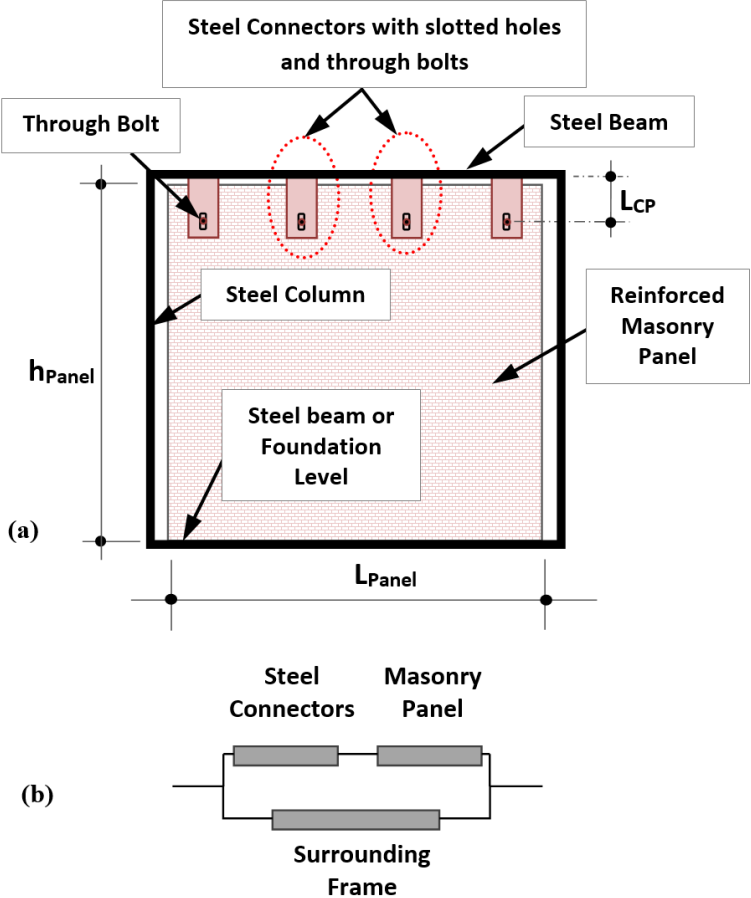
Figure 7.1: (**a**) Hybrid masonry Type I; (**b**) Schematic connection of elements in hybrid masonry Type I building systems.

In hybrid masonry systems, the steel beams are connected using details that transfer limited moment, so the steel frame is not considered to contribute lateral stiffness. K_{CPa} is then much greater than lateral stiffness of the surrounding frame, K_{Frame}. Hence, almost all the lateral shear is attracted by the masonry panel and steel connector system at each story level. For taller structures, steel column axial flexibility reduces the overall system stiffness and should be considered in design.

Based on the assumptions that the steel beams have pinned ends and only horizontal shear is transferred into the top of the masonry panel at floor level, the value of the shear in story i, V_i, and the value of axial force due to lateral-load in each column in story i, P_i, can be calculated by the following expressions:

$$V_i = \sum_{j=i}^{n} F_j \tag{7.2}$$

$$P_i = P_{i+1} + \left(\sum_{j=i+1}^{n} F_j \right) \frac{h_{i+1}}{L} + F_i \frac{(h_{CP})_i}{L} \tag{7.3}$$

where i is the story index; n is the total number of stories; F_j is the applied lateral force at level j; h_{i+1} is the story height for story $i+1$; L is the bay width; h_{cp} is the vertical distance from the through bolts to the point of application of the story force (see Figure 7.2).

Assuming h_{cp} is the same in all stories, and by substituting corresponding values for P_{i+1}, P_{i+2}, …, P_n in Equation (7.3), one can get:

$$P_i = \frac{\sum_{j=i+1}^{n} V_j h_j + V_i h_{CP}}{L} \tag{7.4}$$

where V_j is the story shear in story j and h_j is the story height for the same story. For short connectors, the last terms in the above equation is small and can be ignored. However, in realistic situations the length of the connectors cannot be neglected.
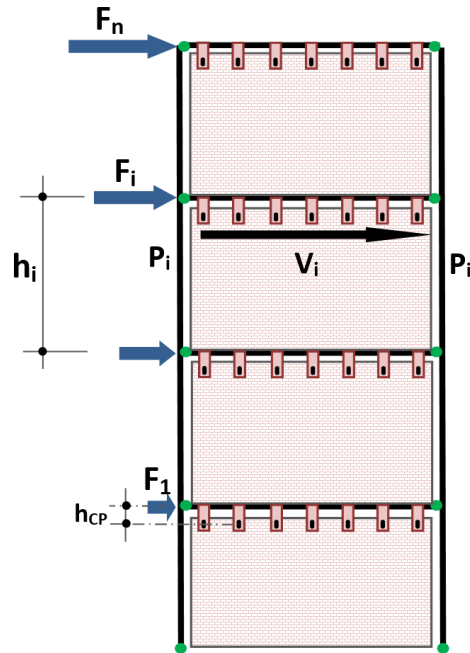
Figure 7.2: Parameters used in lateral load analysis of hybrid masonry Type I.

7.2.2 Ductile limit states

Under in-plane lateral-loads, a hybrid masonry panel can reach a desirable ductile limit state and sustain inelastic demands through two mechanisms: yielding of the steel connector plates or yielding of the vertical steel reinforcement in the masonry panels. Non-ductile limit states, such as break-out/bearing failure where the steel connector plates are bolted to the masonry panel (discussed below), column buckling, beam hinging and connection failure, are undesirable and must be prevented through capacity-design procedures. The behavior of a reinforced masonry panel in the hybrid masonry system is similar to that of a conventional reinforced masonry shear wall. In a reinforced masonry shear wall under lateral load, the controlling limit state is either flexure or shear. In a well-designed flexural-controlled wall, horizontal cracks appear at the wall heel, the vertical reinforcing bars yield before toe crushing of the masonry such that inelastic deformation can be sustained prior to strength degradation. In this case, toe crushing or rupture of the extreme tensile bars causes the final failure. Increasing the amount of vertical reinforcement or the length-to-height ratio of the wall increases the likelihood of shear failure

[140]. The flexural failure mode of steel connector plates is shown in Figure 7.3(a), and the flexural failure mode of a masonry panel is presented in Figure 7.3 (b).

(a)   **(b)**
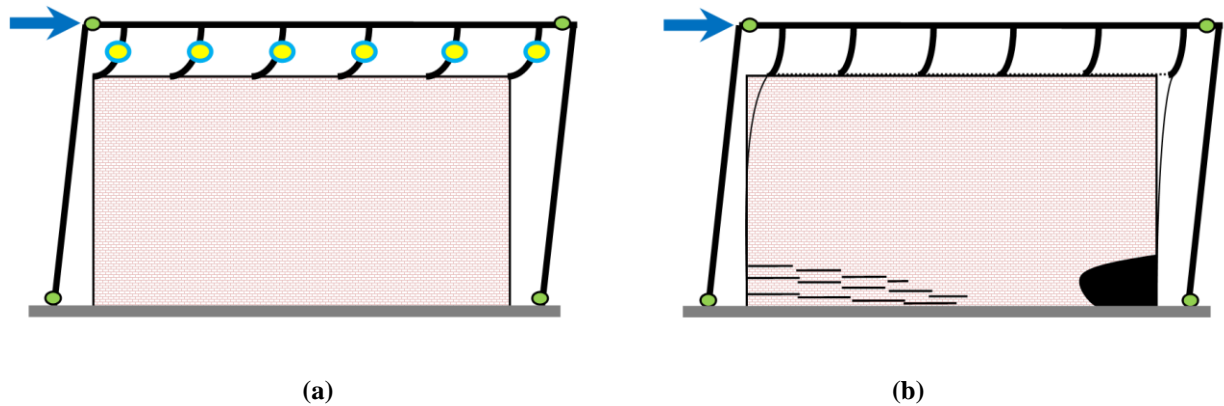
Figure 7.3: Flexural failure modes in hybrid masonry Type I. (**a**) Flexural yielding of connector plates. Yielding of connector plates are shown in circles. (**b**) Flexural yielding of masonry panels. Flexural cracks at the heel and toe crushing are shown on the bottom left and right sides of the panel, respectively. To make the deformed shapes more illustrative, the gaps are shown wider than their normal sizes in a scaled picture.

Whereas the limit states discussed above are desirable for seismic response due to their ductile character, an undesirable non-ductile failure mode for hybrid masonry Type I is break-out/bearing failure of the masonry panel at the points where steel connector plates are attached. Break-out/bearing is a brittle failure mode, and is due to the stress concentrations at the connections of the bolts with the masonry panels. To prevent this failure mode, the portion of the story shear force transferred from a pair of connector plates to a masonry panel is required to be smaller than the shear break-out/bearing strength of a masonry panel. Shear break-out/bearing strength is defined in the next section.

7.2.3 Non-ductile break-out/bearing strength

The Building Code Requirements for Masonry Structures [141] provides guidelines for anchor

bolts embedded in masonry, but thru-bolts are not addressed. To determine the nominal shear strength of anchor bolts, the MSJC [141] addresses the possible failure mechanisms as follows: masonry break-out, masonry crushing, anchor bolt pry-out, and steel yielding. Although the MSJC provisions do not address the thru-bolt connection that is used in hybrid masonry panels, Goodnight et al. [135] used them to provide an estimate for the nominal shear strength to assess the performance of the connections. Furthermore, to establish the break-out strength of the connections, they performed push out tests on embedded thru-bolts in masonry wall specimens. They tested four specimens loaded in displacement control. Most specimens were also loaded in two directions until failure occurred. The specimens showed a masonry break-out strength at least equal to 89kN (20kips) [136].

7.3 Seismic Design Methodologies for Hybrid Masonry Building Systems

Code-based seismic design is most commonly conducted using the equivalent lateral force procedure [138], and the objective is to prevent structural collapse by dictating favorable limit states in the structure. A favorable limit state corresponds to the ductile behavior of the structure as a whole. Seismic design provisions are based on the capacity design approach through which certain structural components are designated as the "dissipative components" or "fuses" and are specially detailed for high energy absorption during a major seismic event. Inelastic response in the "dissipative components" should not impair the gravity load-carrying capacity and the global stability of the system. All other structural components including connections are proportioned in accordance with the capacity design concept [137], and this is typically done by considering adequate over-strength factors to ensure nearly elastic behavior [142, 143].

For hybrid masonry panels, two design approaches are considered for detailing of components. The major considerations of each approach are listed in Table 7.1. The goal is to guarantee a favorable response of the hybrid masonry structural system through utilizing a combination of "dissipative components" with high inelastic deformation capacity, as well as elastic elements with high load capacity. The approaches are described in the following.

Table 7.1: Main considerations in capacity design of hybrid masonry panels.

	Favorable Failure Mode	**Potential** [(*)] Ω_0	**Modes required to be prevented**
Case a	Flexural plastic hinges in connector plates	2	Failure of columns, beams, masonry panels, connections
Case b	Flexural yielding of vertical reinforcing bars in masonry	2.5	Failure of connector plates, columns, beams, connections, shear failure of masonry panels, break-out failure of panels

[*] Note: These values are used in an exploratory study on viability of hybrid masonry panels. To be included in future code provisions, further research is required on seismic response factors for hybrid masonry systems, including R, C_d and Ω_0.

7.3.1 Case a) Inelasticity concentrated in connector plates

For this case, the design strategy is to have the plastic hinges form only in the connector plates. Furthermore, other elements including masonry panels, beams and columns are designed considering appropriate over-strength factors so that they remain elastic during a seismic event. Since the plasticity will be concentrated in the steel connector plates, the over-strength factor equal to 2 is considered for this case.

7.3.2 Case b) Inelasticity concentrated in vertical bars of reinforced masonry panels

The design strategy for this case is to proportion the structural elements so that the inelasticity will be concentrated in the vertical bars in the masonry panels to provide favorable flexural ductility. Accordingly, all steel members including connector plates, beams and columns, and horizontal reinforcement of the masonry panels are designed considering appropriate over-strength factors to remain elastic. In ASCE 7-10 [138], the over-strength factor for all types of reinforced masonry shear walls is 2.5. In view of the fact that the behavior of the masonry panels in hybrid masonry Type I is similar to the behavior of non-load bearing masonry shear walls, a rational assumption is to consider the over-strength factor equal to 2.5 for this case as well. To obtain the seismic shear demands on steel connectors, the shear demands on masonry panels are

multiplied by this over-strength factor. The connector plates then are expected to experience larger shear demands than those of Case a.

7.4 Major Parameters Affecting Shear Demand on Lateral-Load Resisting Elements of a Hybrid Masonry System

Generally speaking, the shear demand on a given hybrid masonry panel is directly related to the design base shear, which in turn is dependent on all the parameters affecting the equivalent lateral-load (e.g. building weight and seismic hazard). To assess the capability of the hybrid masonry system to efficiently resist seismic loads, prototype buildings are considered for a high seismic hazard region. Other significant parameters influencing the shear demands on the lateral-load resisting elements of hybrid masonry systems are discussed in this section. If the system is appropriate for the high seismic hazard region considered in this study, it can be used for moderate and low seismic hazard regions as well.

7.4.1 Response modification coefficient (R)

The response modification coefficient R (commonly called the "R factor") is used in the equivalent lateral force procedure to determine the design base shear [138]. The R factor depends on the energy dissipation capacity of the system, where a larger R factor indicates greater energy dissipation capacity and produces a smaller design base shear. Using connector plates with special detailing to dissipate the input seismic energy is expected to permit a higher R factor. Tests on connector plates and fuses are being performed at the University of Hawaii [134]. In the present study, shear demands have been calculated for R factors equal to 3, 4, 5, and 6. For the case where inelasticity is concentrated in the connector plates (Case a), the steel connectors are detailed to behave as energy dissipating fuses [134]. Hence, R factors equal to 5 and 6 are considered to be appropriate values for the feasibility studies considering Case a. For the case where inelasticity is concentrated in the vertical bars of the masonry panels (Case b), a range of R factors from 3 to 6 have been assumed. The considered range covers the possible R factors from ordinary reinforced masonry walls to specially reinforced ones.

7.4.2 Number of hybrid masonry panels

Increasing the number of hybrid masonry panels decreases the shear demand per panel and connector. Generally, non-structural masonry walls and partitions in a building with a steel frame can be adapted into hybrid masonry panels. However, similar to any other structural walls in a building system, the placement of the panels should avoid causing any significant seismic irregularities.

7.4.3 Number of steel connectors per panel (N_{CP_panel})

As mentioned earlier a steel connector comprises a pair of steel connector plates and a through bolt. In calculation of the force demands per connector, one significant assumption is that all connectors per panel have the same geometry and material properties. There is a limit on the number of connectors per panel, which is dependent on the minimum practical spacing. In this study, it is assumed that only one connector per concrete masonry unit (CMU) can be used. Therefore, N_{CP_panel} cannot exceed the number of CMUs per course at each frame bay. Considering the length of each CMU equal to 0.41m (16 inches):

$$N_{CP\_panel} \leq L_{panel} / 0.41 \tag{7.5}$$

where L_{panel} is the panel length in meters.

Furthermore, for both Cases a and b, the shear per connector (from lateral-load analysis) multiplied by the over-strength factor, $(V_{CP})_u \, \Omega_0$, is required to be equal or smaller than the shear break-out strength of the panel per connector, V_{BO_panel}:

$$\Omega_0 \left(V_{CP} \right)_u = \Omega_0 \left(\left(V_{panel} \right)_u / N_{CP\_panel} \right) \leq V_{BO\_panel} \tag{7.6}$$

in which $(V_{panel})_u$ is the shear per panel from lateral-load analysis. Hence,

$$\left(\Omega_0 \left(V_{panel} \right)_u \right) / V_{BO\_panel} \leq N_{CP\_panel} \tag{7.7}$$

Equation (7.7) provides the minimum N_{CP_panel}. N_{CP_panel} must be sufficient to tolerate the

demands from out-of-plane loads as well. This check can be done after the design of connector plates for seismic demands. In summary, the number of steel connectors per panel is dependent on the shear demand per panel, the shear break-out capacity of the panel per connector, and the number of CMUs used per course at each frame bay.

7.5   Seismic Design Process

In a hybrid masonry Type I system, steel connectors and the masonry panels carry only the lateral seismic loads. Beams and columns are part of the lateral-load resisting system, but also carry the gravity loads. Hence, seismic demands on beams and columns are required to be combined with gravity loads considering appropriate load combinations [138]. Furthermore, for both design options (*i.e.,* Cases a and b), the beams and columns must remain elastic during a seismic event. Therefore, the seismic demands on these elements are required to be multiplied by appropriate over-strength factors or be estimated considering the maximum demands transferred to these elements. The seismic design processes for Cases a and b are summarized in Figure 7.4 and Figure 7.5, respectively, and described below.

7.5.1   Case a) Inelasticity concentrated in steel connector plates

1) Determine the placement of hybrid masonry panels in the system, and the number of such panels in each direction. A larger number of hybrid masonry bays in plan provides higher redundancy for the system and lower shear demand per panel.

2) Estimate the number of connectors per panel (N_{CP_Panel}), based on Equations (7.5) and (7.7). If the maximum possible number of connectors per panel is smaller than the required number of connectors per panel, the number of hybrid masonry bays in the system must be increased.

3) Estimate the seismic shear demand per connector from the lateral-load analysis (($V_{panel})_u/N_{CP\_panel}$), and design the connectors as fuses.

4) Design the masonry panels, beams, and columns considering the appropriate over-strength factor. The shear demand on the panels can be calculated from the following equation:

$$\left(V_{panel}\right)_D = \Omega_0 \left(V_{panel}\right)_u = \Omega_0 \left(V_{CP}\right)_D N_{CP\_panel} \qquad (7.8)$$

The demands on columns including the seismic axial load component, and the concentrated moments on the beams generated from the shear demand on the connector plates, must be multiplied by the over-strength factor or be designed for the maximum load transferred to these members from the connector plates. After estimating the demands on beams and columns, the current code criteria [144, 145] can be used for design of these members.

7.5.2   Case b) Inelasticity concentrated in vertical bars of reinforced masonry panels

1) Determine the placement of hybrid masonry panels in the system, and the number of such panels in each direction. A larger number of hybrid masonry bays in plan provides higher redundancy for the system and lower shear demand per panel.

2) Estimate the shear demand per panel at each story of the building $(V_{panel})_u$ from lateral-load analysis.

3) Estimate the number of connectors per panel (N_{CP_Panel}), based on Equations (7.5) and (7.7). If the maximum possible number of steel connectors per panel is smaller than the required number of steel connectors per panel, the number of hybrid masonry bays in the system must be increased.

4) Design the panels according to the next section for the following demands. For flexural design and shear design, respectively:

$$\left(V_{panel}\right)_{DF} = \left(V_{panel}\right)_u \qquad (7.9)$$

$$\left(V_{panel}\right)_{DV} = \Omega_0 \left(V_{panel}\right)_u \qquad (7.10)$$

5) Design the connector plates, beams, and columns considering the appropriate over-strength factor or the maximum load transferred from the panel to these members. The shear demand on a pair of connector plates can be calculated as:

$$\left(V_{CP}\right)_D = \left(\Omega_0 \left(V_{panel}\right)_u\right) / N_{CP\_panel} \qquad (7.11)$$

The maximum moment on a pair of connector plate can be calculated as:

$$(M_{CP})_D = (V_{CP})_D \cdot L_{CP} \tag{7.12}$$

where L_{CP} is the length of steel connectors from the through bolts to the support of the connector plates on the beam (Figure 7.1(a)). For design of beams and columns, the demands from gravity loads need to be added as well using appropriate load combinations [138].

7.5.3 Design of hybrid masonry structural panels

7.5.3.1 Case a) Inelasticity concentrated in steel connector plates

The story shear that can be carried by a hybrid masonry panel for Type I is the minimum of the panel shear strength V_{Shear}, the shear force corresponding to the flexural strength V_{Flex}, and the shear break-out strength of the panel per steel connector multiplied by the number of connectors per panel (Equation (6.13)). Shear strength and flexural strength of hybrid masonry panels can be calculated per MSJC provisions for masonry shear walls [141]. Further research is required on break-out strength of masonry panels with through bolts.

$$(V_{panel})_C = min(V_{Shear}, V_{Flex.}, (V_{BO\_panel} \times N_{CP\_panel})) \tag{7.13}$$
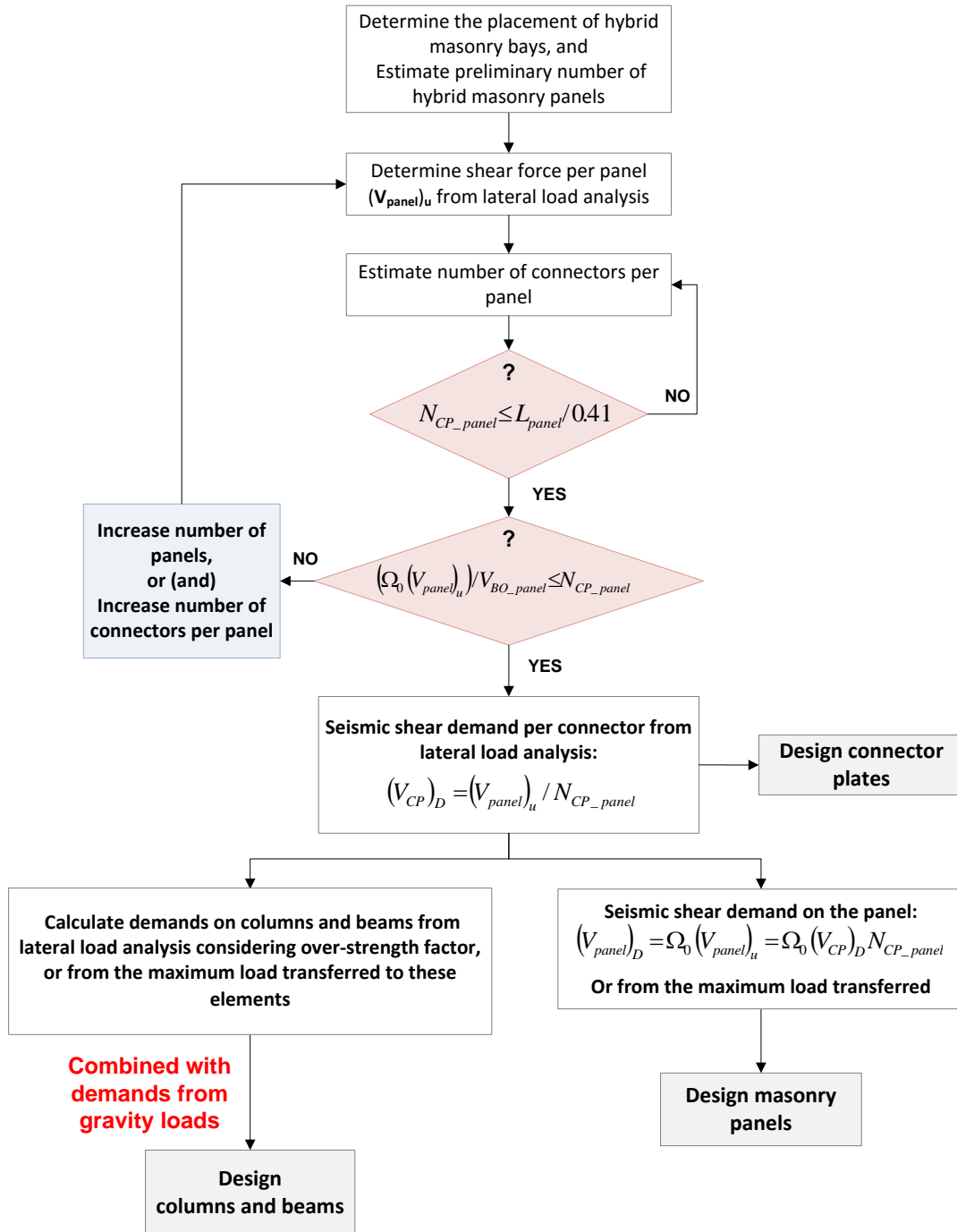
Figure 7.4: Seismic design process for hybrid masonry building systems considering connector plates with fuse behavior (Case a).

Determine the placement of hybrid masonry bays, and Estimate preliminary number of hybrid masonry panels

Estimate shear force per panel $(V_{panel})_u$ from lateral load analysis

Estimate number of connectors per panel

?
$$N_{CP\_panel} \leq L_{panel}/0.41$$
NO

YES

?
$$\left(\Omega_0\left(V_{panel}\right)_u\right)/V_{BO\_panel} \leq N_{CP\_panel}$$
NO

Increase number of panels, or (and) Increase number of connectors per panel

YES

Seismic shear demand on panels:
Flexural design: $\left(V_{panel}\right)_{DF} = \left(V_{panel}\right)_u$
Shear design: $\left(V_{panel}\right)_{DV} = \Omega_0\left(V_{panel}\right)_u$

Design masonry panels

Calculate demands on columns and beams from lateral load analysis considering over-strength factor, or from the maximum load transferred to these elements

Combined with demands from gravity loads

Design columns and beams

Seismic shear demand per connector from lateral load analysis:
$$\left(V_{CP}\right)_D = \left(\Omega_0\left(V_{panel}\right)_u\right)/N_{CP\_panel}$$
Or from the maximum load transferred

Design connector plates

Figure 7.5: Seismic design process for hybrid masonry building systems considering yielding of vertical reinforcing bars in reinforced masonry panels (Case b).

7.5.3.2 Case b) Inelasticity concentrated in vertical bars of reinforced masonry panels

The required shear strength of a hybrid masonry panel for Type I to develop the flexural strength, $(V_{panel})_{CF}$, is obtained from Equation (7.14), and the shear strength of a hybrid masonry panel Type I, $(V_{panel})_{CV}$, is the minimum of the panel shear strength V_{Shear}, and the break-out strength of the panel per connector times the number of connectors per panel Equation (7.15).

$$(V_{panel})_{CF} = M_{C\_Panel} / h_{panel} \tag{7.14}$$

$$(V_{panel})_{CV} = \min(V_{Shear}, (V_{BO\_panel} \times N_{CP\_panel})) \tag{7.15}$$

M_{C_Panel}, is the flexural strength of a masonry panel.

7.6 Viability of Hybrid Masonry as a Lateral-Load Resisting System

Based on the procedures described above, the feasibility of hybrid masonry panels as practical lateral-load resisting systems is studied by calculating seismic demands on lateral-load resisting elements of prototype buildings and designing them. The system design results are presented for the first story, which has the maximum shear demand on the lateral-load resisting elements.

7.6.1 Description of Prototype Buildings

The prototypes studied in this research are office buildings located in Los Angeles, California, which is a high seismic hazard region. Three, six and nine story office buildings of rectangular plan configuration, which are 51.1 m long in the E-W direction and 36.5 m wide in the N-S direction, are considered (Figure 7.6). Each story height is 3.7 m and 7.3 m bays are used in each direction. Floors consist of 8.3 cm lightweight concrete placed on corrugated metal deck. Structural steel members are wide-flange shapes comprised of A992 steel and the beams are pin-ended. The nominal loading magnitudes are adopted from the design examples in FEMA 451 [146]: 3.0 kN/m^2 for floor dead load (deck, slab, beams, girders, fireproofing, ceiling, partitions, mechanical and electrical systems); 2.6 kN/m^2 for roof dead load (roofing, insulation, deck, beams, girders, fireproofing, ceiling, mechanical and electrical systems); 2.4 kN/m^2 for office live load; 1.2 kN/m^2 for roof live load; 1.2 kN/m^2 for exterior wall cladding loads (evenly

distributed over the exterior wall area of the buildings, including a 1.1 m high parapet wall above the roof level); weight of the hybrid masonry panels: 4.0 kN/m².

The design response spectrum parameters considered in the seismic design calculations are: site class D, S_S=1.5 g, S_1=0.6 g, F_a=1.0, F_v=1.5, S_{MS}=1.5 g, S_{M1}=0.9 g, S_{DS}=1.0, S_{D1}=0.6, occupancy category II (I=1.0), and redundancy factor ρ =1. The approximate equation of the code is used to estimate the period of the prototype buildings [138].
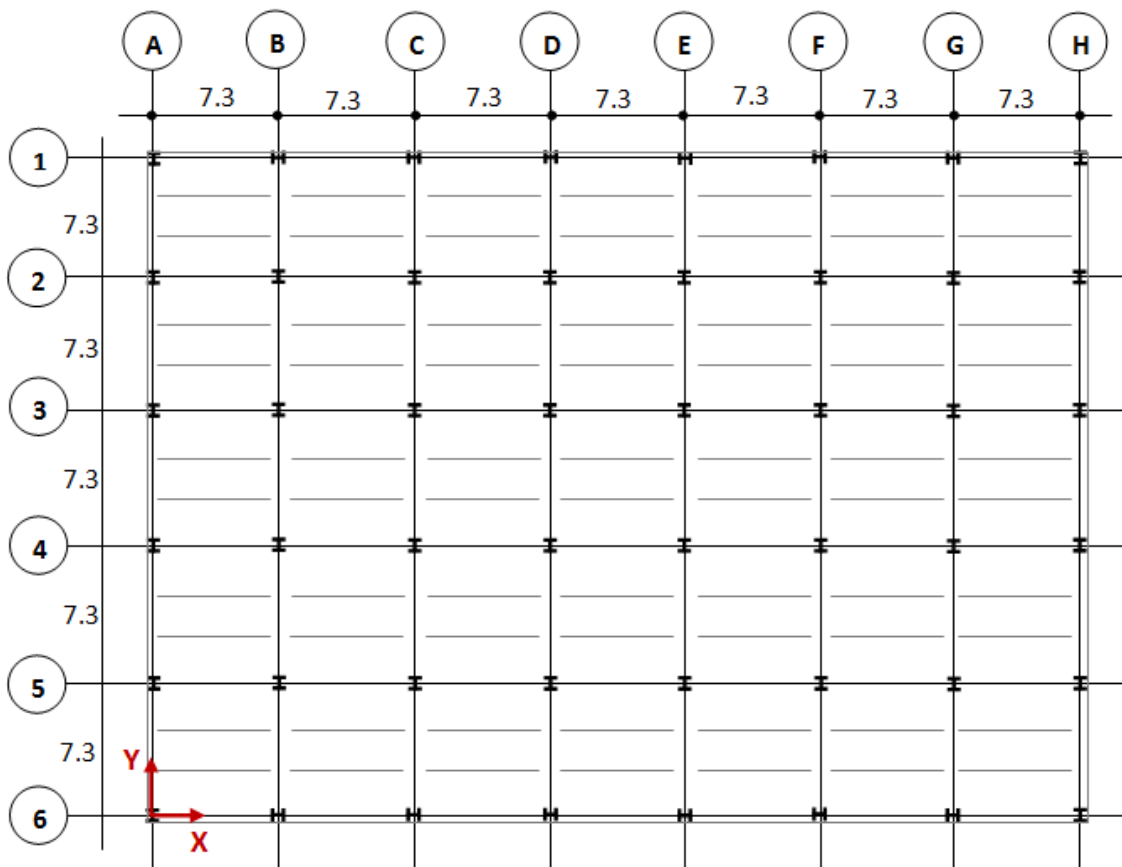
Figure 7.6: Typical floor framing plan (dimensions in meters).

7.6.2 Design of Prototype Buildings

7.6.2.1 Case a) Inelasticity concentrated in steel connector plates
The demands on the lateral-load resisting elements are calculated considering two possible

values of the response modification coefficient, R = 5 and 6. The break-out strength of a panel at one connector location is considered to be 89 kN (20 kips), based on preliminary experimental studies by Goodnight et al. [135]. Considering W14 column section and a 64 mm (2.5 in) gap at each side of the panel, the length of the masonry panel is 6.8 m. For this length of the panel, from Equation (7.5), the maximum number of connectors per panel is equal to 16. The connector plates utilized in the design are similar to the tapered fuses, detailed and tested at the University of Hawaii [134]. The steel design is based on AISC 360-10 [144], and AISC 341-10 [145]. The fuse illustrated in Figure 7.7(a) is designed similar to a cantilever beam subjected to a transverse concentrated load at the tip, and is detailed so that the cross sections at the top and bottom of the fuse reach their maximum moment capacity at the same time. Moreover, the design is based on the provisions of Section F11 in AISC 360-10. It is assumed that the fuse is made up of steel plates with F_y =250 MPA (36 ksi), and that the fuse length (L_f) is equal to 20 cm. The values of the panel shear forces from lateral-load analysis are shown for 3, 6, and 9 story prototype buildings in Table 7.2. In Table 7.2, W_r is the ratio of required number of panels to the possible number of structural panels in each direction. The possible number of panels is equal to the number of bays in each frame times the number of frames in each direction. Regarding the prototype buildings considered in this study, the possible number of hybrid masonry panels in the N-S direction is equal to 40 (see Figure 7.6). However, this number is impractical since the building would not be functional. The parameters considered for design of the masonry panels are listed in Table 7.3. In designing the panels, it is assumed that the vertical bars are distributed evenly across the panel width. The shear strength of the panel can be calculated from Equation (7.13). Other calculations are summarized in Table 7.5 to Table 7.9. The results indicate that the system is potentially viable for the 9-story prototype office building located in a high seismic hazard region.

Table 7.2: Panel shear forces from lateral-load analysis (Case a).

R	Base shear (kN)			No. of panels in each direction			$(V_{panel})_u$ (kN)		
	3 Story	6 Story	9 Story	3 Story	6 Story	9 Story	3 Story	6 Story	9 Story
5	4517	10084	14461	7	15	21	645	672	689
6	3731	8183	11643	6	12	17	622	682	685

Note:

W_r = Ratio of required No. of panels to the possible number of panels in the system

$W_r \leq 0.4$

$0.4 < W_r \leq 0.55$

Table 7.3: Parameters considered for design of reinforced masonry panels.

d' (mm)	50	End cover over bars
f'_m (MPa)	10	Compressive strength of the masonry
f_y (MPa)	414	Yield strength of the reinforcement
L (m)	6.83	Length of the panel
b (mm)	194	Thickness of the panel (8" CMU fully grouted)
h (m)	2.90	Height of the panel
E_m (GPa)	9	Modulus of elasticity of masonry (900 f'_m)
E_S (GPa)	200	Modulus of elasticity of the reinforcement
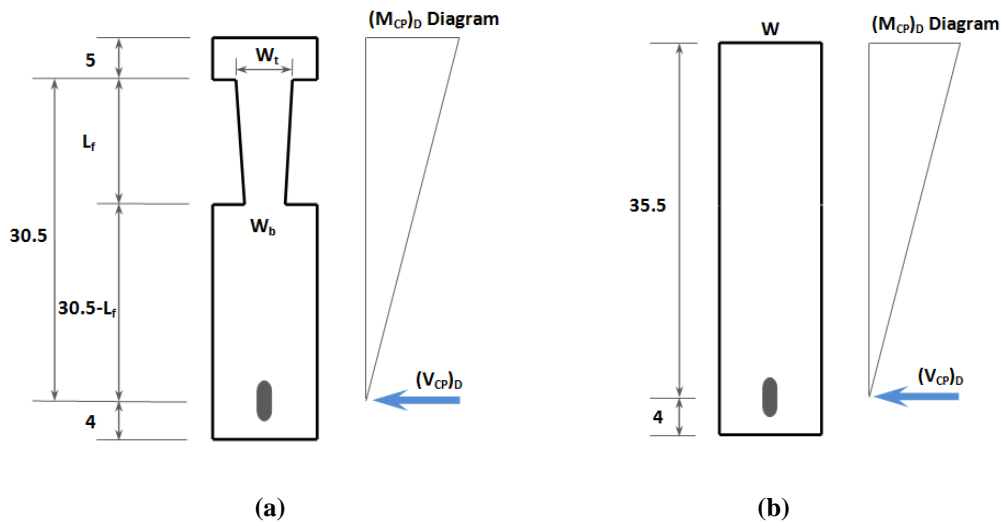
Figure 7.7: (a) Fuse geometry. (b) Connector plate geometry (dimensions in centimeters).

7.6.2.2 Case b) Inelasticity concentrated in vertical bars of reinforced masonry panels

The demands on the lateral-load resisting elements are calculated considering four possible values of response modification coefficient, R 3, 4, 5 and 6. Break-out strength of the panel per connector and the length of the panels are similar to those of Case a. It is assumed that steel connectors are made up of plates with F_y =250 MPA (36 ksi), and that the connector length, from the center of the slotted holes to their support, is equal to 35.5 mm (Figure 7.7(b)). Results of calculations based on the process described in the previous sections are summarized in Table 7.4 and in Section 7.8. According to the results presented in Table 7.4, for high seismic hazard regions, using Case b is suitable for the low-rise (around 3 stories) prototype buildings.

Table 7.4: Panel shear forces from lateral-load analysis (Case b).

R	Base shear (kN)			No. of panels in each direction			$(V_{panel})_u$ (kN)		
	3 Story	6 Story	9 Story	3 Story	6 Story	9 Story	3 Story	6 Story	9 Story
3	8063	19750	27971	15	35	N.F.	538	564	---
4	5847	13598	20367	11	24	36	532	567	566
5	4677	10437	15194	11	19	27	425	549	563
6	3898	8403	12152	11	15	22	354	560	552

Note:

W_r = Ratio of required No. of panels to the possible number of panels in the system

	$W_r \leq 0.4$		$0.55 < W_r \leq 0.75$
	$0.4 < W_r \leq 0.55$		$0.75 < W_r < 1$
	$1.0 \leq W_r$ Not Feasible (N.F.)	

7.7 Summary, Conclusions and Future Research

Hybrid masonry is a new system for seismic-resistant building construction. The system takes advantage of masonry walls present in most buildings as non-structural elements, and by using special details, makes them part of the lateral-load resisting system. A hybrid masonry system consists of reinforced masonry panels within a steel framed structure, where steel connectors are used to tie the surrounding steel frame to the masonry panels. To date, the system has been used for construction of low-rise buildings in the eastern and mid-western United States. The current research provides a framework for using one type of hybrid masonry in areas of moderate and high seismicity. The main contributions of this study are summarized as follows:

- Simplified lateral-load analysis of hybrid masonry Type I is presented. The results show that the lateral-load path is straightforward and thus the system is well suited to hand calculations.

- Employing the widely-accepted capacity design concept, this study establishes the basis for seismic design of hybrid masonry building systems, specifically those employing hybrid masonry Type I. Seismic design methodologies for buildings incorporating hybrid masonry Type I are discussed for two cases: inelasticity concentrated in the steel connector plates and inelasticity concentrated in the vertical steel bars of the masonry panels.

- The viability of hybrid masonry as a new seismic lateral-load resisting system was considered and the results of seismic demand calculations for the basic lateral-load resisting elements show that it is a promising system. Nevertheless, there will be significant demands on the steel connector plates for the case where plasticity is concentrated in flexural yielding of steel vertical bars in the masonry panels. The structural system then requires more hybrid masonry bays compared with corresponding systems when plasticity is concentrated in steel connector plates.

- When inelasticity is concentrated in the steel connector plates, mid-rise prototype office buildings (around 9 stories) appear to be feasible. However, when inelasticity is concentrated in the masonry panels, only low-rise buildings (around 3 stories) appear to be feasible.

- The results presented in this chapter are for prototype office buildings located on Site Class D in a high seismic hazard region. The seismic demands on the system are smaller for buildings located on sites with better soil conditions and in moderate seismic hazard regions. Therefore, hybrid masonry Type I can potentially be used for taller prototype buildings than those considered in this study.

- The sample design of prototype buildings presented in this study can be used as a practical design guide for engineers considering hybrid masonry for seismic design.

Before hybrid masonry can be effectively used as a seismic structural system, large-scale experimental validation of the system behavior is required. This testing is planned as part of an ongoing research project on hybrid masonry systems [127]. All hybrid masonry configurations

will be studied (Types I, II and III) and the critical force transfer mechanisms at the steel-masonry interfaces will be explored. These mechanisms include masonry through-bolts (as used for steel connectors), contact and bearing, and headed steel connectors. Validation of robust steel-masonry interface behavior and global system performance is a critical step for implementing hybrid masonry seismic systems.

7.8 Supplementary Materials

7.8.1 Summary of calculations for Case a)

The number of steel connectors per panel, and the shear demands per connector for the prototype buildings are presented in Table 7.5. Table 7.6 includes moment demands and the cross-section geometry at the top of the fuses. Moment demands and the cross-section geometry at the bottom of fuses are presented in Table 7.7. Checks for the panel break-out strength and the shear demands on the panels are presented in Table 7.8. A summary of shear strength for the masonry panels using various configurations of bars is presented in Table 7.9. Since the shear break-out strength has been checked in Table 7.8, Table 7.9 then includes the shear strength calculations governed by flexural and shear action of the reinforced masonry panel.

Table 7.5: Number of steel connectors per panel and shear demand per connector (Case a).

R	$(N_{CP\_panel})_{min}$			$(N_{CP\_panel})_{used}$			$(V_{CP})_D$ (kN)		
	3 Story	6 Story	9 Story	3 Story	6 Story	9 Story	3 Story	6 Story	9 Story
5	15	16	16	16	16	16	40	42	43
6	14	16	16	16	16	16	39	43	43

Table 7.6: Moment demands and cross-section geometry at the top of fuses (Case a).

R	$(M_{CP})_D$ at the top of fuse (kN-m)			Top of fuse cross section (for a single plate)					
				3 Story		6 Story		9 Story	
	3 Story	6 Story	9 Story	W_t (mm)	t (mm)	W_t (mm)	t (mm)	W_t (mm)	t (mm)
5	12.3	12.8	13.1	100	12	100	12	100	12
6	11.8	13.0	13.0	95	12	100	12	100	12

Table 7.7: Moment demands and cross-section geometry at the bottom of fuses (Case a).

R	$(M_{CP})_D$ at the bottom of fuse (kN-m)			Bottom of fuse cross section (for a single plate)					
				3 Story		6 Story		9 Story	
	3 Story	6 Story	9 Story	W_b (mm)	t (mm)	W_b (mm)	t (mm)	W_b (mm)	t (mm)
5	4.1	4.3	4.4	55	12	60	12	60	12
6	3.9	4.3	4.3	55	12	60	12	60	12

Table 7.8: Check of panel break-out strength and shear demands on panels (Case a).

R	$\Omega_0 (V_{panel})_u / N_{CP\_panel}$ [1] (kN)			V_{BO_panel} x N_{CP_panel} [2] (kN)			$(V_{panel})_D = \Omega_0 (V_{panel})_u$ [3] (kN)		
	3 Story	6 Story	9 Story	3 Story	6 Story	9 Story	3 Story	6 Story	9 Story
5	81	84	86	1423	1423	1423	1291	1345	1377
6	78	85	86	1423	1423	1423	1244	1364	1370

Note:

(1) The values calculated must be smaller than the break-out strength of the panel considered in the design (See Equation (7.6)).

(2) The values calculated in this column must be greater than the shear demand on the panel (See section "*Design of hybrid masonry structural panels*").

(3) The shear demand on the panel.

Table 7.9: Summary of shear strength calculations of masonry panels for various configurations of bars per MSJC 2008 Strength method.

c [1] (cm)	Vertical Bars	V_{Flex} [2] (kN)	V_m [3] (kN)	$(V_n)_{max}$ [4] (kN)	$(V_{Flex \& Shear})_C$ [5] (kN)	$(V_s)_{Req.}$ [6] (kN)
41	11 # 4 (D13)	365	1149	1953	365	NA
82	11 # 6 (D19)	772	1149	1953	772	NA
105	11 # 7 (D22)	1011	1149	1953	1011	NA
128	11 # 8 (D25)	1262	1149	1953	1262	113
153	11 # 9 (D29)	1525	1149	1953	1525	376

Note:

Shear break-out strength has been checked in other Tables, this Table then includes the shear strength calculations governed by flexural and shear action of the reinforced masonry panel.

(1) Length of compression zone.

(2) Flexural shear strength of the masonry panel.

(3) Shear strength provided by the masonry.

(4) Upper bound limit on the nominal shear strength of the masonry panel per MSJC 2008 [141].

(5) Shear capacity provided by flexural and shear action of the masonry panel. Comparison of these values with shear demands per panel from Table 7.4 shows the feasibility of design of the panels for seismic lateral-load demands.

(6) Required shear capacity of horizontal steel bars.

7.8.2 Summary of calculations for Case b)

Calculations for Case b are summarized in Table 7.10 to Table 7.12.

Table 7.10: Number of steel connectors per panel and shear demand per connector (Case b).

R	$(N_{CP\_panel})_{min}$			$(N_{CP\_panel})_{used}$			$(V_{CP})_D$ (kN)		
	3 Story	6 Story	9 Story	3 Story	6 Story	9 Story	3 Story	6 Story	9 Story
3	16	16	---	16	16	---	84	88	---
4	15	16	16	16	16	16	83	89	88
5	12	16	16	16	16	16	66	86	88
6	10	16	16	16	16	16	55	88	86

Table 7.11: Moment demands and cross sections geometry (Case b).

| | $(M_{CP})_D$ at connector support (kN-m) | | | Connectors cross section (for a single plate) | | | | | |
| | | | | 3 Story | | 6 Story | | 9 Story | |
R	3 Story	6 Story	9 Story	W (mm)	t (mm)	W (mm)	t (mm)	W (mm)	t (mm)
3	29.9	31.4	---	160	12	160	12	---	---
4	29.5	31.5	31.4	155	12	160	12	160	12
5	23.6	30.5	31.3	140	12	160	12	160	12
6	19.7	31.1	30.7	125	12	160	12	160	12

Table 7.12: Check of panel break-out strength and shear demands on panels (Case b).

| | $\Omega_0 (V_{panel})_u / N_{CP\_panel}$ [1] (kN) | | | V_{BO_panel} x N_{CP_panel} [2] (kN) | | | $(V_{panel})_D = (V_{panel})_u$ [3] (kN) | | |
R	3 Story	6 Story	9 Story	3 Story	6 Story	9 Story	3 Story	6 Story	9 Story
3	84	88	---	1423	1423	---	538	564	---
4	83	89	88	1423	1423	1423	532	567	566
5	66	86	88	1423	1423	1423	425	549	563
6	55	88	86	1423	1423	1423	354	560	552

Note:

(1) The values calculated must be smaller than the break-out strength of the panel considered in the design (See Equation (7.6)).

(2) The values calculated in this column must be greater than the shear demand on the panel (See section "*Design of hybrid masonry structural panels*").

(3) The shear demand on the panel.

8 Capacity Spectrum-Based Seismic Design of Type I Hybrid Masonry Structural Systems with Fuse Connectors

Abstract

Applying the force-based seismic design procedures of the current codes to hybrid masonry structural systems requires availability of the seismic response factors. Whereas, hybrid masonry is a relatively new lateral-load resisting system for which seismic response factors, including the response modification coefficient (R), are not defined in the current codes. In this study, an integrated simple approach for performance-based seismic analysis and design of hybrid masonry Type I systems employing fuse connector plates is presented. The procedure used in this study is based on the Capacity Spectrum Method. In this study, we apply the method for design of a sample hybrid masonry building system.

8.1 Introduction

Masonry infill walls are primarily used in buildings as architectural partitions worldwide, and their function as structural elements is usually ignored. Contrary to masonry infill panels, hybrid masonry is a relatively new technology for earthquake resistant design of buildings, and was first

proposed in 2007 [125]. The system has been introduced to the eastern United States for low-rise office and commercial buildings, but it has not been used in high-seismic regions yet.

The innovative hybrid masonry technology is based on the structural action of reinforced masonry panels connected to a surrounding steel frame via novel steel connectors. The connector plates if detailed appropriately can accommodate a large dissipation of energy through yielding of the steel plates. Depending on the interfacial conditions between a masonry panel and a surrounding frame, hybrid masonry panels are categorized into 3 major groups designated as Types I, II, and III [126].

An overview of the current research on hybrid masonry panels is given in Abrams et al. [147]. Employing capacity design concept, seismic design methodologies for buildings incorporating hybrid masonry panels Type I are discussed in Eidini et al. [131] (see Chapter 7) for two cases of plasticity concentrated in steel connectors or in vertical steel bars of the masonry panels.

Seismic response factors (e.g., response modification coefficient, R) are not proposed in the current codes for hybrid masonry systems. One advantage of performance-based design procedures is that they are not dependent on the current codes' seismic response factors, but on the actual performance of the structures. To estimate the base shear of the hybrid masonry Type I systems employing connector fuses, the current study employs a performance-based design procedure which does not require the code-based response modification factors. The approach in this study is an iterative process implemented in the framework of the Capacity Spectrum Method (CSM). CSM has been widely accepted and extensively improved [148, 149, 150, 151, 152] since its recommendation in ATC-40 [153]. The steps of the approach are described in this study. The proposed method includes an iterative process through which a hybrid masonry structural system with fuse connector plates is designed depending on its energy dissipation capacity. In the proposed design approach, the value of the system R factor is regulated in the process, depending on the energy absorption capacity of the system.

8.1.1 Major Advantages of Hybrid Masonry

Hybrid masonry uses masonry walls present in most buildings as non-structural elements and by

employing special details makes them as parts of the lateral-load resisting system. This merit is in accordance with a key principle of seismic resistant design of buildings as noted by Bertero and Brokken [132]. The main advantages of hybrid masonry systems are listed as follows.

- Bracing steel frames using reinforced masonry panels leads to an integrated efficient application of both materials.

- In a hybrid masonry system, moment-resisting connections or steel bracings in steel frames are not required. Hence, making the installation of both the masonry and the structural steel simpler, for instance by eliminating the construction difficulty in trying to fit masonry around the braces.

- Introducing the technology to engineering and research society as a new lateral load resisting structural system rather than non-structural partitions as are in the case of infill panels.

- Removing the interaction between a masonry panel and columns, and therefore preventing from unfavorable brittle shear failure modes of columns (e.g., reported in [154] for the case of bounding concrete frames) by introducing gaps between a frame and masonry panels in hybrid masonry Types I and II.

- The panels can be designed to reduce the extent of the damage in the masonry, for example via introducing the novel steel connector plates as fuses for dissipating seismic energy [131].

- Presence of the gaps both at the sides and at the top of the wall as well presence of slotted holes in the connector plates in hybrid Type I, makes lateral-load analysis of the system straightforward. Therefore, the system is well-suited for hand calculation [131].

- The system is well-suited for a performance-based design approach, particularly for a design philosophy in which the plasticity is concentrated in the connector plates. Focusing on this point, the current study introduces a performance-based approach for seismic design and analysis of hybrid masonry Type I structural systems.

Incomplete codes and lack of recommendations for seismic design of hybrid masonry systems are among the main barriers to implement the system [147]. The current study addresses this issue by introducing a seismic design approach which is not dependent on the code-based seismic response factors.

8.2 Hybrid Masonry Type I

The paper by Eidini et al. [131] describes the force transfer mechanism in hybrid masonry Type I. In this study, we employ an alternative approach based on the free-body diagram of a masonry panel in Type I hybrid masonry to explain the force transfer mechanism. As described in the current literature [131], in Type I hybrid masonry, only shear force transfers to the masonry panel, and specifically there is no axial load transmission due to existence of gaps between the masonry panel and the frame as well as presence of slotted holes in the steel connectors. The story shear transfers through the steel links connecting the beam to the masonry panel (Figure 8.1 (a)).

(a)   (b)   (c)
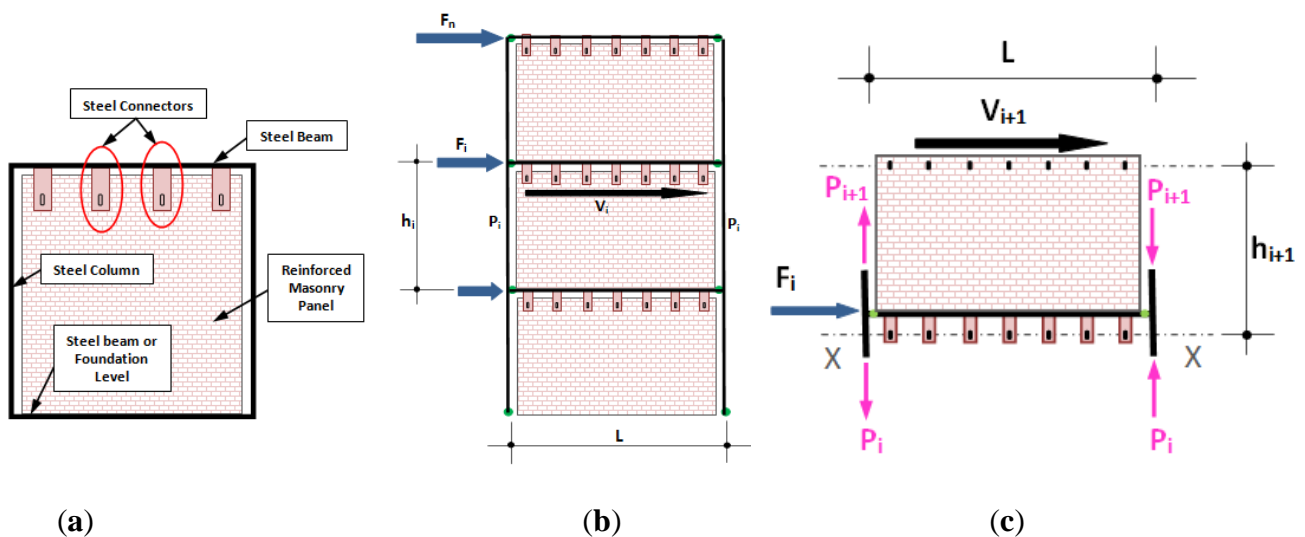
Figure 8.1: (**a**) Hybrid masonry Type I. (**b**) Parameters used in lateral load analysis of hybrid masonry Type I. (**c**) Free-body diagram of a masonry panel in hybrid masonry Type I systems.

8.2.1 Lateral load analysis in hybrid masonry Type I

The free-body diagram of a masonry panel in hybrid Type I is shown in Figure 8.1(c). Beams are pin-ended in hybrid masonry systems. Therefore, the value of moments in columns are negligible, and are not considered in the following derivations.

The story shear at level $i+1$ is given by

$$V_{i+1} = \sum_{j=i+1}^{n} F_j \tag{8.1}$$

From moment equilibrium around the *X-X* axis in Figure 8.1(c), the axial force in the column is given by

$$\sum M_{X-X} = 0 \quad \rightarrow \quad P_i L = P_{i+1} L + V_{i+1} h_{i+1} + F_i (h_{CP})_i$$

$$P_i = P_{i+1} + V_{i+1} \frac{h_{i+1}}{L} + F_i \frac{(h_{CP})_i}{L} \tag{8.2}$$

where h_{CP} is the length from the slotted holes to the point of application of story forces. Substituting Equation (8.1) in Equation (8.2), we have

$$P_i = P_{i+1} + \left(\sum_{j=i+1}^{n} F_j \right) \frac{h_{i+1}}{L} + F_i \frac{(h_{CP})_i}{L} \tag{8.3}$$

Similarly, for P_{i+1},

$$P_{i+1} = P_{i+2} + V_{i+2} \frac{h_{i+2}}{L} + F_{i+1} \frac{(h_{CP})_{i+1}}{L} \tag{8.4}$$

Assuming h_{CP} is identical in all stories, and by substituting corresponding values for P_{i+1}, P_{i+2}, ..., P_n in Equation (8.2), one can get

$$P_i = \frac{\sum_{j=i+1}^{n} V_j h_j}{L} + \left(\sum_{j=i}^{n} F_j \right) \frac{h_{CP}}{L} = \frac{\sum_{j=i+1}^{n} V_j h_j + V_i h_{CP}}{L} \tag{8.5}$$

For very short connector plates, the last term in Equation (8.2) to Equation (8.5) can be ignored. In RAM Element software [155] the steel connector lengths are assumed to be negligible, and therefore the value of axial load in columns is estimated from the following formula [147, 124]. However, in realistic situations, the length of connector plates is not very small and its effect on column axial load cannot be neglected. From Equation (8.5), the larger the length of steel

connectors, the larger the axial loads in columns (under lateral load). The frame and the panel moments under lateral load are given in the following equations

$$\left(M_{Frame}\right)_i = P_i\,L = \sum_{j=i+1}^{n} V_j\,h_j + V_i\,h_{CP} \tag{8.6}$$

$$\left(M_{Panel}\right)_i = V_i\,(h_p)_i \tag{8.7}$$

Assuming that the panel height is identical in all stories and that it is approximately equal to the story height (e.g., $(h_p)_i = h_i = h$), we have

$$\left(\frac{M_{Frame}}{M_{Panel}}\right)_i = \frac{\sum_{j=i+1}^{n} V_j\,h_j + V_i\,h_{CP}}{V_i\,(h_p)_i} \cong \frac{\sum_{j=i+1}^{n} V_j}{V_i} + \frac{h_{CP}}{h} \tag{8.8}$$

If right hand side of Equation (8.6) is constant (i.e., if lateral load pattern, steel connector length and story heights remain unchanged throughout the stories), column axial load has an inverse relation with the frame bay width, i.e., increasing the bay width in this case reduces the axial load in the columns.

From Equation (8.8), the ratio of frame overturning moment to that of the panel at level i is not dependent on L (i.e., bay width), and it depends on the lateral load pattern, length of steel connectors and both the story and the panel heights. Additionally, Equation (8.8) shows that if lateral load distribution pattern is scaled uniformly, the ratio does not change. However, the ratio changes if lateral load pattern changes. For example, consider a four-story structure in which the story height is the same in all stories, and is subjected to an inverse triangular lateral load pattern with the magnitude equal to 1 to 4 at the 1st to 4th stories, successively. For the first story we have

$$\left(\frac{M_{Frame}}{M_{Panel}}\right)_1 \cong \frac{\sum_{j=2}^{n} V_j}{V_1} + \frac{h_{CP}}{h} = \frac{9+7+4}{10} + \frac{h_{CP}}{h} = 2 + \frac{h_{CP}}{h} \tag{8.9}$$

Now consider a rectangular lateral load pattern producing the same base shear as that of the inverse triangular lateral load pattern. The loading magnitude at each story will then be equal to 2.5. Hence,

$$\left(\frac{M_{Frame}}{M_{Panel}}\right)_1 \cong \frac{\sum_{j=2}^{n} V_j}{V_1} + \frac{h_{CP}}{h} = \frac{7.5+5+2.5}{10} + \frac{h_{CP}}{h} = 1.5 + \frac{h_{CP}}{h} \tag{8.10}$$

8.2.2 Lateral stiffness of hybrid masonry Type I

In this section, using a simplified model we obtain the lateral stiffness of a hybrid masonry Type I structural system. In the system, each masonry panel is connected in series with the steel connectors (Figure 8.2(a)). Hence, for a single panel, the displacement of the panel is given by

$$\Delta_{Pij} = \Delta_{Cij} + \Delta_{Mij} \tag{8.11}$$

in which the indices i and j represent the bays and stories numbers, respectively. Also, the indices P, C and M denote panel (hybrid panel), connectors and masonry panel, successively. From the above relation we have

$$\frac{V}{K_{Pij}} = \frac{V}{K_{Cij}} + \frac{V}{K_{Mij}} \tag{8.12}$$

$$\frac{1}{K_{Pij}} = \frac{1}{K_{Cij}} + \frac{1}{K_{Mij}} \tag{8.13}$$

The steel connectors per each panel are acting in parallel with each other. Hence, the lateral stiffness of the connectors per panel at bay i and story j, K_{Cij}, can be estimated as

$$K_{Cij} = \sum_{1}^{N_{CP\_panel}} K_{CP} = N_{CP\_panel} (K_{CP}) \tag{8.14}$$

From Equation (8.13), in a single hybrid masonry panel, the total stiffness of the masonry panel and connectors acting in series is dominated by the more flexible element, i.e., the connector

plates which are much more flexible than the masonry panels. Hence, for a single panel, lateral stiffness of the hybrid panel can be considered equal to that of the connectors as given in the following.

$$K_{Pij} \cong K_{Cij} \tag{8.15}$$
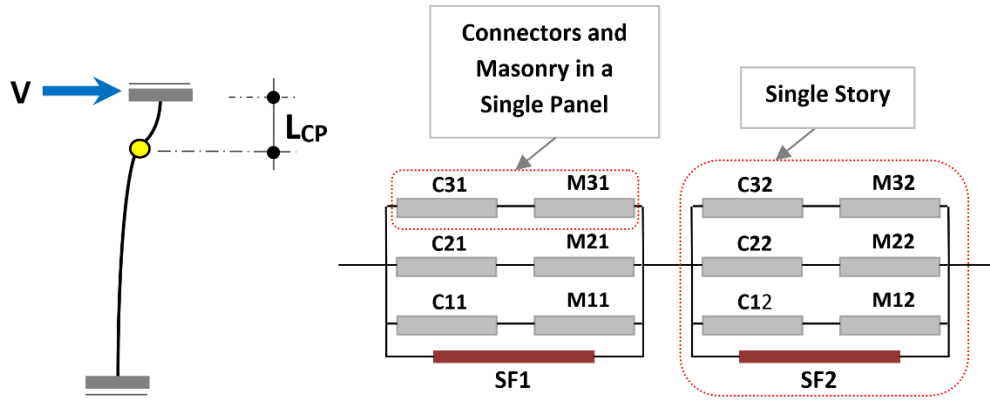
Figure 8.2: (**a**) Schematic connection of a hybrid masonry panel to steel connectors. (**b**) Schematic connection of elements in a two-story and three-bay hybrid masonry Type I building system. *Cij* represents the steel connectors in the *i*th bay and *j*th story, and *Mij* stands for the masonry panel in the *i*th bay and *j*th story. *SFj* represents the steel frame at the *j*th story.

The schematic connections of the structural elements in a two-story and three-bay hybrid masonry Type I building system is illustrated in Figure 8.2(b). The lateral stiffness of the *j*th story can be estimated as

$$K_{Sj} = \sum_{i=1}^{No.of\ HM\ bays} K_{Pij} + K_{SFj} = \sum_{i=1}^{No.of\ HM\ bays} K_{Cij} + K_{SFj} \tag{8.16}$$

where K_{SFj} is the stiffness of the steel frame at the *j*th story. Assuming the steel beams have pinned ends, and disregarding the stiffness of the frame, we have

$$K_{Sj} \cong \sum_{i=1}^{No.of\ HM\ bays} (N_{CP\_panel}\ K_{CP})_i \tag{8.17}$$

Assuming only one type of steel connector is used at each story, we have

$$K_{Sj} = K_{CP} \sum_{i=1}^{No.of\ HM\ bays} (N_{CP\_panel})_i = (N_{CP\_Story})_j (K_{CP})_j \qquad (8.18)$$

in which $(N_{CP\_Story})_j$ is the number of steel connectors at the jth story. The relation above shows that in a system with long hybrid masonry bays in which the steel connectors are much more flexible than the masonry panel, the number and the stiffness of connector plates control the story stiffness. Note that the relation above is true on the basis of the assumptions that the steel frame does not contribute in the lateral stiffness and that the connector plates are much more flexible than the masonry panels. By considering the steel beams as pin-ended and designing the connector plates as energy absorption fuses, the realistic situation can be close to the assumed one.

8.3   Performance-based Seismic Design of Hybrid Masonry Structural Systems

In this section, a performance-based design approach is proposed for seismic analysis and design of hybrid masonry Type I systems. The design methodology is based on formation of the plastic hinges in the connector plates, i.e., case (a) described by Eidini et al. [131] (see Chapter 7). The main assumptions used in the proposed design process are summarized as follows:

- Plastic hinges only form in the connector plates. This assumption is accommodated through capacity design of the system described by Eidini et al. [131].
- To obtain the story displacement, only connector plates are considered and the displacements of the masonry panels are ignored (rotation of the masonry panels and the flexural and shear displacement of the panel are small compared to the deformation of the connectors, and are neglected in the calculations).
- Only one type of connector plate is used at each story, i.e., the geometry and load-displacement behavior of all connector plates are the same (this assumption simplifies the design process).

The performance-based seismic design procedure presented in this study is an iterative process based on CSM. The process is illustrated in Figure 8.3. The steps of the proposed CSM-based approach for seismic design of hybrid masonry Type-I systems with fuse connector plates are given in the following.

1) Estimate the base shear. Assume a value for R factor (force reduction factor), and calculate lateral load demand for preliminary design stage. R=6 is suggested at this stage.
2) Design the system based on the steps for case (a) described by Eidini et al. [131].
3) Construct the earthquake response spectrum in acceleration displacement (A-D) format. To convert a spectrum from the S_a-T format to A-D format use the following relation.

$$S_{di} = \frac{T_i^2}{4\pi^2} S_{ai} g \qquad (8.19)$$

4) Construct the capacity curve of the system in terms of the base shear versus roof displacement. As described in Section 8.2.2, almost all lateral shear is resisted by the system of connector plates and the masonry panel. Moreover, the connector plates per each panel are acting in parallel whose resultant system is performing in series with the masonry panel. Hence, given the load-displacement curve for the connector plates, the capacity curve of the system can be constructed in terms of base shear versus roof displacement. The process is illustrated in Figure 8.4 and Figure 8.5. Therefore, we have

$$\left(V_{Panel}\right)_{Capacity} = (F_u)_{CP} \cdot N_{CP\_panel} \qquad (8.20)$$

in which $(V_{Panel})_{Capacity}$ is the shear capacity of each hybrid masonry panel; $(F_u)_{CP}$ is the ultimate shear load capacity of a connector plate. Story shear can then be calculated from the sum of shear capacity of the panels at each story.

$$V_{Story} = \sum (V_{Panel})_{Capacity} \qquad (8.21)$$

5) Convert the capacity curve of the system to that of a single degree of freedom (SDOF) representation in A-D format. The conversion is carried out via the following formula.

$$S_{ai} = \frac{V_i / W}{\alpha_1} \qquad (8.22)$$

144

$$S_{di} = \frac{\Delta_{roof}}{PF_1 \times \varphi_{roof,1}} \qquad (8.23)$$

where (S_{ai}, S_{di}) are points on capacity spectrum curve corresponding to (V_i, Δ_{roof}) on the capacity curve of the system. α_1 and PF_1 are the mass and modal participation factors of the first mode, respectively; $\phi_{roof,1}$ is amplitude of the first mode at the roof level; V is base shear; W is the dead load plus probable live load; Δ_{roof} is the roof displacement; S_a is the spectrum acceleration; S_d is the spectrum displacement.

$$\alpha_1 = \frac{\left[\sum_{i=1}^{N}(w_i\phi_{i1})/g\right]^2}{\left[\sum_{i=1}^{N}\frac{w_i}{g}\right]\left[\sum_{i=1}^{N}(w_i\phi_{i1}^2)/g\right]} \qquad PF_1 = \left[\frac{\sum_{i=1}^{N}(w_i\phi_{i1})/g}{\sum_{i=1}^{N}(w_i\phi_{i1}^2)/g}\right] \qquad (8.24)$$

6) Draw the demand versus capacity curve in A-D format in a single plot.

7) Determine the performance point, i.e., the intersection of the demand with the capacity curve. The performance point obtained in this way is for a SDOF system which needs to be converted to that of a multi-degree of freedom (MDOF) system.

8) Evaluate performance of the structure. If the performance point is before and close to the end point of the capacity curve, *i.e.*, it meets the following relation, go to the next step; otherwise the system design needs to be verified.

$$0 \le \frac{d_e - d_p}{d_p} \le tolerance \qquad (8.25)$$

where d_e and d_p are ultimate and performance point displacements, respectively. In this study 0.05 is used as the tolerance.

9) Check code displacement limit criteria. If OK, design the system for the demand on each elements; otherwise use less ductile connector plates and go to Step 3.
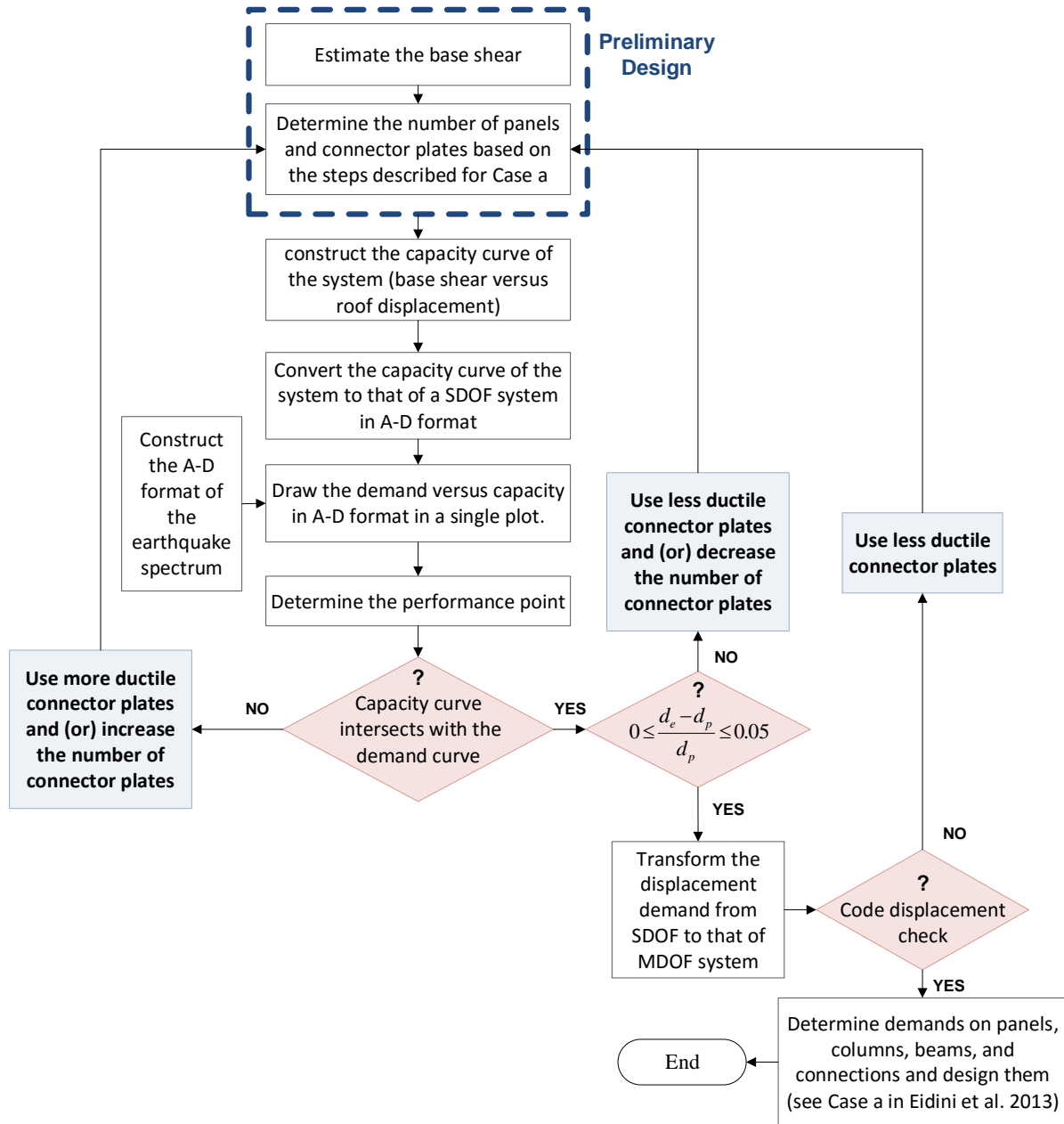
Figure 8.3: CSM-based design of hybrid masonry Type I building systems with fuse connector plates.
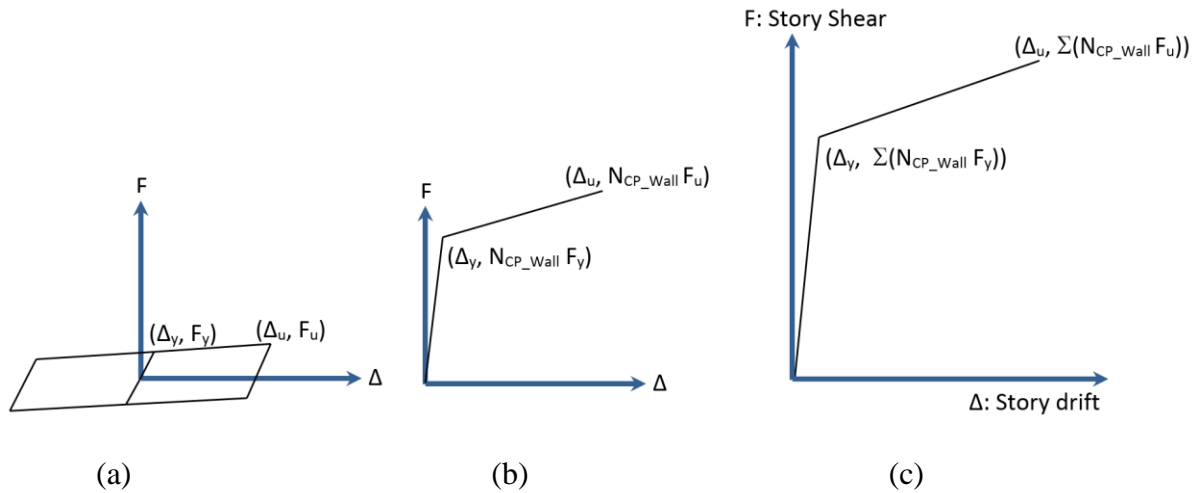
Figure 8.4: (**a**) Envelope curve derived from the test results; (**b**) load-displacement curve for a hybrid masonry panel Type-I; (**c**) Story shear-displacement curve for a frame employing hybrid masonry Type-I panels.
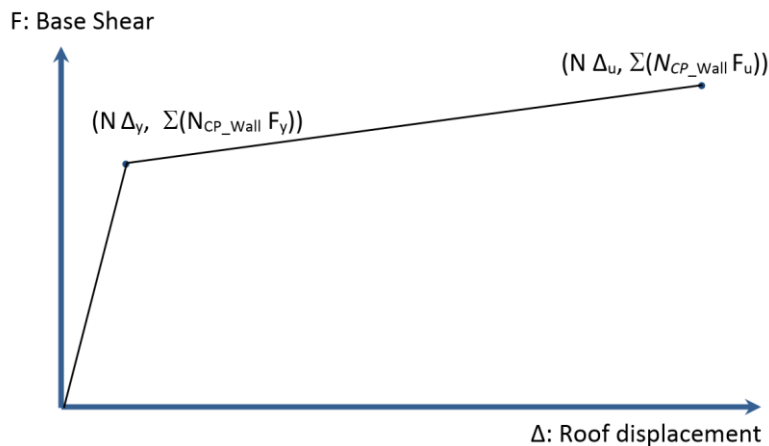
Figure 8.5: Base shear versus roof displacement.

8.4   Description of a Prototype Building

The example considered for this section is a three-story office building located in a moderate seismic hazard region. The building has a rectangular plan configuration with 21.9 m long in the E-W direction and 21.9 m wide in the N-S direction (Figure 8.6). Each story height is 3.7 m. They are framed in structural steel with 7.3 m bays in each direction. Floors include 8.3 cm

lightweight concrete placed on metal deck. Structural steel members are wide-flange shapes comprised of A992 steel. The values of loading are: dead load (floors)= 3.0 kN/m²; dead load (roof)= 2.6 kN/m²; live load= 2.4 kN/m² (office buildings); live load= 1.2 kN/m² (for roof is assumed); cladding loads: 1.2 kN/m² (evenly distributed over the exterior wall area of the building, including a 1.1-m-high parapet wall above the roof level). The design response spectrum parameters considered in this section are: site class D, S_S=0.9 g, S_1=0.3 g, F_a=1.14, F_v=1.8, S_{MS}=1.03 g, S_{M1}=0.54 g, S_{DS}=0.68, S_{D1}=0.36, occupancy category-II (I=1.0), and redundancy factor ρ=1.
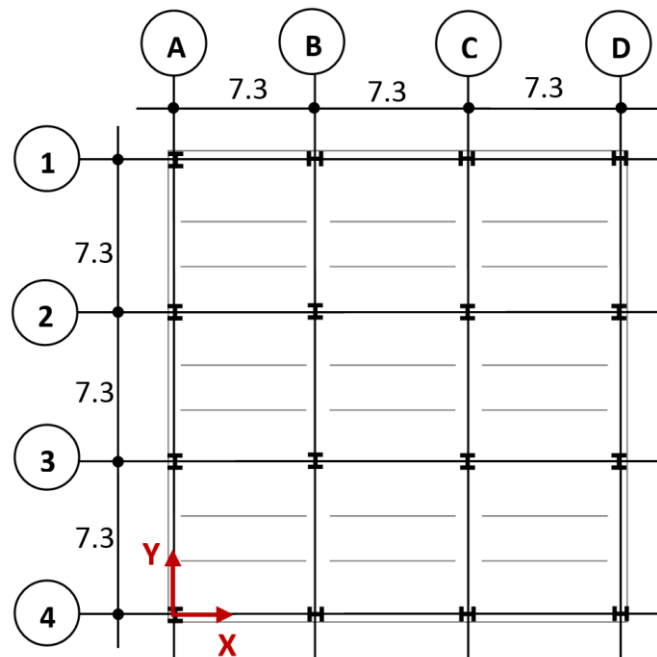
Figure 8.6: Typical floor framing plan (dimensions in meters).

8.5   Design of the Prototype Building

The system is first designed based on the steps described for the Case a described by Eidini et al. [131]. For preliminary seismic design stage, we assume R=6 for the system. The assumed R factor for the current hybrid masonry structure is investigated in the process as well. The building is designed assuming two lateral load resisting systems (LLRS) in each direction. In addition to the key assumptions used in the design process (see Section 8.3), the over-strength

factor (Ω_0) equal to 2 is used in the capacity design process for the steel connector plates. The break-out strength of a panel at one connector location is considered to be 89 kN (20 kips), based on preliminary experimental studies by Goodnight et al. [135]. Considering W14 column section and a 64 mm (2.5 in) gap at each side of the panel, the length of the masonry panel is 6.8 m. For this length of the panel, from the following relation [131], the maximum number of connectors per panel is equal to 16.

$$N_{CP\_panel} \leq L_{panel} / 0.41 \qquad (8.26)$$

where L_{panel} is the panel length (m). The connector plate used in the CSM design process is the tapered fuse specimen (P4_T4_Ft3-01), detailed and tested at the University of Hawaii [134] to perform as energy dissipating links. The test set up for the connector plate along with the Load-Displacement behavior of the connector is shown in Figure 8.7. The envelope of the curve, used in the design process, is also shown in Figure 8.7(b). For the test specimen, the yield and ultimate forces and displacements used in the design process are given in Table 8.1. Table 8.2 presents the details of calculations to obtain the number of steel connectors per panel and the lateral-load capacity of each hybrid masonry panel. The data required for drawing the capacity curve of the system is also presented in Table 8.3.
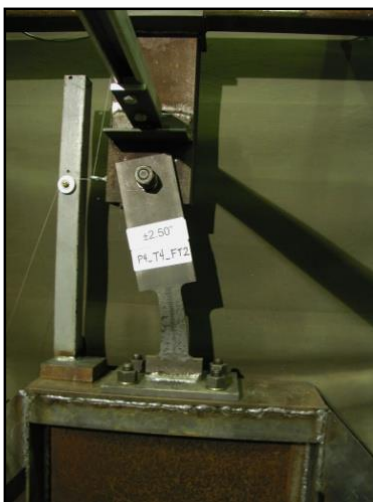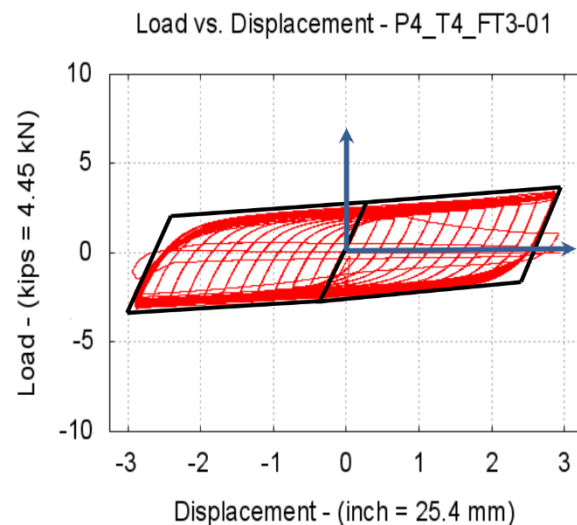
(**a**)   (**b**)

Figure 8.7: (**a**) Test set up for P4_T4_Ft3-01 fuse reported by Johnson et al. [134]. (**b**) Load versus displacement for a sample fuse [134] and its envelope drawn by black thick line.

Table 8.1: Critical points of hysteretic response for the fuse used in the design.

Yield Point		Ultimate Point	
Δ_y mm	F_y kN	Δ_u mm	F_u kN
5.3	6.7	73.7	13.3

Table 8.2: The number of steel connectors used per panel and lateral-load capacity of each hybrid masonry panel.

Level	$(V_u)_{LLRS}$ [1] kN	N_{panel} [2]	$(V_u)_{panel}$ [3] kN	N_{CP_panel} [4] Required	N_{CP_panel} [5] min	N_{CP_panel} [6] Used	$(V_C)_{panel}$ [7] kN
3	88.4	2	44.2	2	1	3	80
2	161.3	2	80.7	4	2	6	160
1	197.8	3	65.9	3	2	7	187

Note:

(1) Lateral-load demand on each LLRS. The structures include two LLRS.

(2) Number of hybrid masonry panels at each level per LLRS.

(3) Lateral-load demand per each hybrid masonry panel.

(4) Required number of steel connectors per panel.

(5) Minimum number of steel connectors per panel from Equation (6.7).

(6) Used number of steel connectors per panel.

(7) Lateral-load capacity of each panel.

Table 8.3: The data needed to draw the capacity curve of the system.

Level	$(V_{u\text{-}LLRS})_C$ kN	$(\Delta_u)_{CP}$ mm	$(D_{Story})_u$ mm	$(V_{y\text{-}LLRS})_C$ kN	$(\Delta_y)_{CP}$ mm	$(D_{Story})_u$ mm
3	160.1	2.9	8.7	80.1	0.21	0.63
2	320.3	2.9	5.8	160.1	0.21	0.42
1	560.5	2.9	2.9	280.2	0.21	0.21

Note:

$\mu = \Delta_u/\Delta_y = 13.8$ $R_\mu = \sqrt{(2\mu-1)} = 5.16$

     $\Omega_d = 2$ $R = 10$

$$R = R_\mu \Omega_d Y \qquad (8.27)$$

where R_μ and Ω_d are the ductility reduction and over-strength factors, respectively, as given by the following relations [156, 143]. The parameter Y is the allowable stress factor [156].

$$R_\mu = \frac{V_e}{V_y} \qquad \Omega_d = \frac{V_y}{V_d} \tag{8.28}$$

For the structures designed based on the ultimate strength method, the allowable stress factor is equal to unity. Hence, the response reduction factor is given by

$$R = R_\mu \Omega_d \tag{8.29}$$

For intermediate period range, and from the equal energy criterion we have [143]

$$R_\mu = \sqrt{2\mu - 1} \tag{8.30}$$

Considering $\Omega_d = \Omega_0 = 2$, we have

$$R = 2\sqrt{2\mu - 1} \tag{8.31}$$

Assuming the first mode is the predominant mode of the system, capacity curve of the system is converted to that of a SDOF representation in A-D format [153]. Furthermore, the demand and capacity curves are drawn in A-D format in a single plot. To obtain the demand curve, the earthquake spectrum needs to be reduced. The reduction factors account for the energy dissipated by the structure during a seismic event. The spectrum reduction factors are used as follows

$$SR_A \approx \frac{3.21 - 0.68\, Ln\left(\beta_{eff}\right)}{2.12} \tag{8.32}$$

$$SR_V \approx \frac{2.31 - 0.41\, Ln\left(\beta_{eff}\right)}{1.65} \tag{8.33}$$

In the above formula, SR_A and SR_V are spectral reduction values in constant acceleration and constant velocity ranges of the spectrum, respectively; β_{eff}, is the effective damping of the structure, which combines the inherent viscous damping and hysteretic damping. It can be calculated from the following relation [153]:

$$\beta_{eff} = \kappa\beta_0 + 5 = \frac{63.7\kappa\left(a_y d_p - d_y a_p\right)}{a_p d_p} + 5 \qquad (8.34)$$

in which, β_0, is the viscous damping equivalent to the hysteretic damping; 0.05, is the assumed inherent viscous damping of the structure; (d_y, a_y) and (d_p, a_p) are the coordinates of the yield and performance points, respectively (see Figure 8.8); Performance point is located on the intersection of the demand and capacity curves and is determined via an iterative procedure [153]. The parameter κ is a damping modification factor introduced in ATC 40 for existing Reinforced Concrete (RC) structures. The factor is dependent on the structural behavior. In ATC 40, structural behavior is also categorized based on quality of the lateral load resisting system and duration of the ground motion. The structure under investigation is a newly designed hybrid masonry building, and not a RC structure. For this example, since inelasticity is concentrated to the steel connector fuses, a higher ductility than that of an existing RC structure, and consequently a higher κ factor than that suggested in ATC 40 are expected. For the current example, the same κ factor as in the ATC 40 for the structures of category A is used, which is conservative.

The performance point, i.e., the intersection of the demand with the capacity curve, is then determined. The performance point obtained in this way is for a SDOF system that needs to be converted to that of a MDOF system.

The demand versus capacity curve in A-D format, for the example system, is presented in Figure 8.9. The figure shows that the system provides sufficient capacity and the performance point is (0.1 g, 6.8 in).
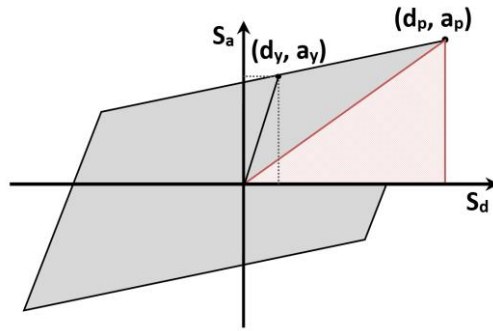
Figure 8.8: Bilinear representation of the capacity spectrum and the key points in damping calculation.
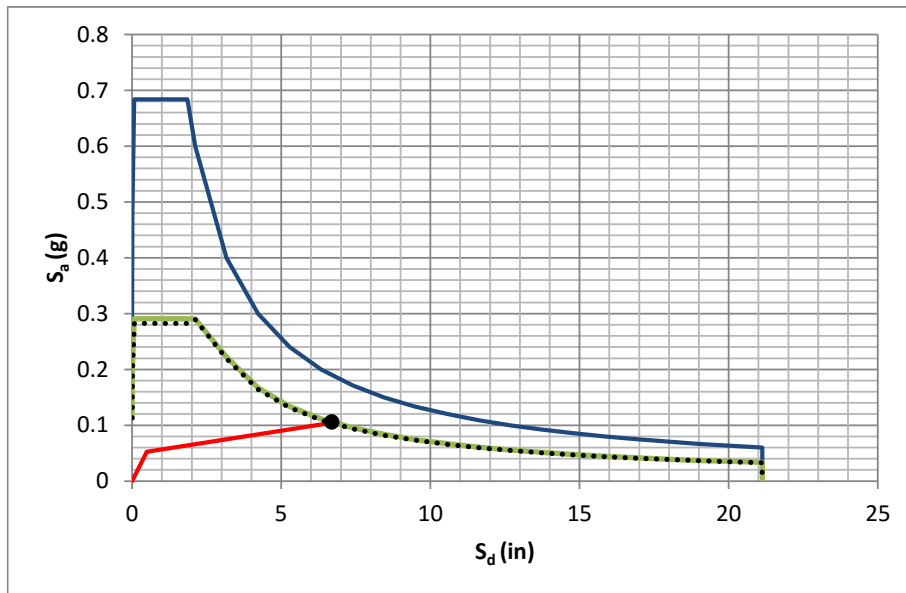
Figure 8.9: Final iteration result. The dotted black line (2nd Iteration) matches well with the green line. Therefore, performance point is shown by a solid black circle in the figure.

8.6 Concluding Remarks and Future Research

A Capacity Spectrum Method-based seismic design approach has been proposed for hybrid masonry Type I structural systems with fuse connectors. Advantages of hybrid masonry Type I along with the straightforward implementation of the performance based design approaches for

fuse-based hybrid masonry panels, offer an interesting solution for seismic design of these types of structures.

The proposed approach is capable of providing an estimate of the seismic demands, e.g., the force and displacement demands on a hybrid masonry Type I structure with fuse connectors without performing a nonlinear push-over analysis. In this regard, as a substitute for nonlinear push-over analysis, we obtain the capacity curve of the system via knowing the load-displacement behavior of the connector plates. Moreover, using the test results carried out on connector plates at the University of Hawaii, the application of the method is presented for analysis and design of an example system. The proposed method is for the structures in which the first mode is the predominant mode of the structure. Hence, it is suitable for low and mid-rise buildings. Based on the study by Eidini et al. [131], hybrid masonry Type I is also applicable to low and mid-rise buildings.

In addition to the advantages of displacement-based design approaches cited in the literature [157], the major benefits of the proposed approach are as follows:

- The method is an interactive seismic analysis and design procedure which is not dependent on the code proposed seismic response factors, but rather on the performance of the system.
- The preliminary design is only dependent on the design of the fuses. Therefore, less effort is needed compared with the application of the performance-based design approaches on other structures.

Before the proposed method can be effectively used, several issues must be addressed as listed in the following.

- In this study, the spectrum reduction factors have been chosen based on the proposed values in the ATC40. However, a higher reduction factor is expected due to the higher ductility of the Type I hybrid masonry with fuse connectors. More research is required on the appropriate reduction factor for this type of the structure.
- Only one type of steel connector plate has been used in the design process. For the effective application of the proposed method, availability of the database on the load-

displacement relationships for steel connector plats is necessary.

- The length of the slotted holes in the connector plates is required to be sufficient to accommodate the story drifts during a seismic event. Otherwise, the axial load will be transferred to the connector plates.

- Under lateral load a hybrid masonry panel may fail due to the lack of strength in either in-plane or out-of-plane directions. This study only addresses the in-plane behavior of the panels.

- The push-over curves are obtained based on the assumption that the steel frame does not contribute in the lateral stiffness. Effect of the stiffness of the continuous columns on the lateral stiffness of the system, even though small, needs to be investigated.

- For the case of the panels with small bay lengths, the effect of the stiffness of the masonry panels on the lateral stiffness must be investigated.

- Base shear capacity is only dependent on the first story connector plates! Force-displacement curves of the other stories need to be checked separately.

- As an alternative, fix the displacement (target displacement) and calculate the demand accordingly. Start with a target displacement and a value for ductility. Then, calculate the acceleration demand (base shear). Iteration is not needed in this approach.

- Perform the pushover analysis of the structures considering the effect of the columns in the frame, and compare the result with the simplified model proposed in the current work. In this regard, the nonlinear force-displacement, obtained numerically for the connector plate used in the proposed design procedure, has been compared and calibrated to match with the corresponding force-displacement curve obtained from experimental test (see Figure 8.10). Hence, it can be used for further investigations of the behavior of the prototype structures using a nonlinear analysis.
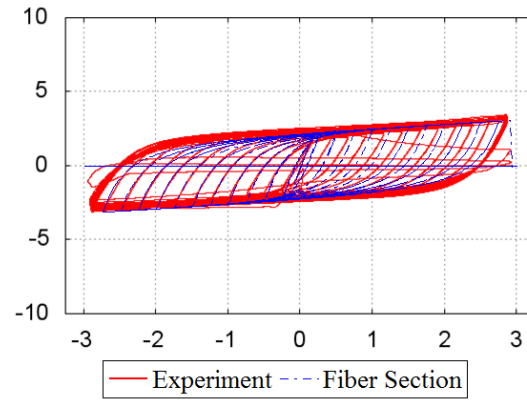
Figure 8.10: Load versus displacement for a sample fuse obtained experimentally shown by red line [134] versus the corresponding plot obtained from computational simulation performed by OpenSees.

Appendix A: Artworks Related to the BCH₂ Pattern
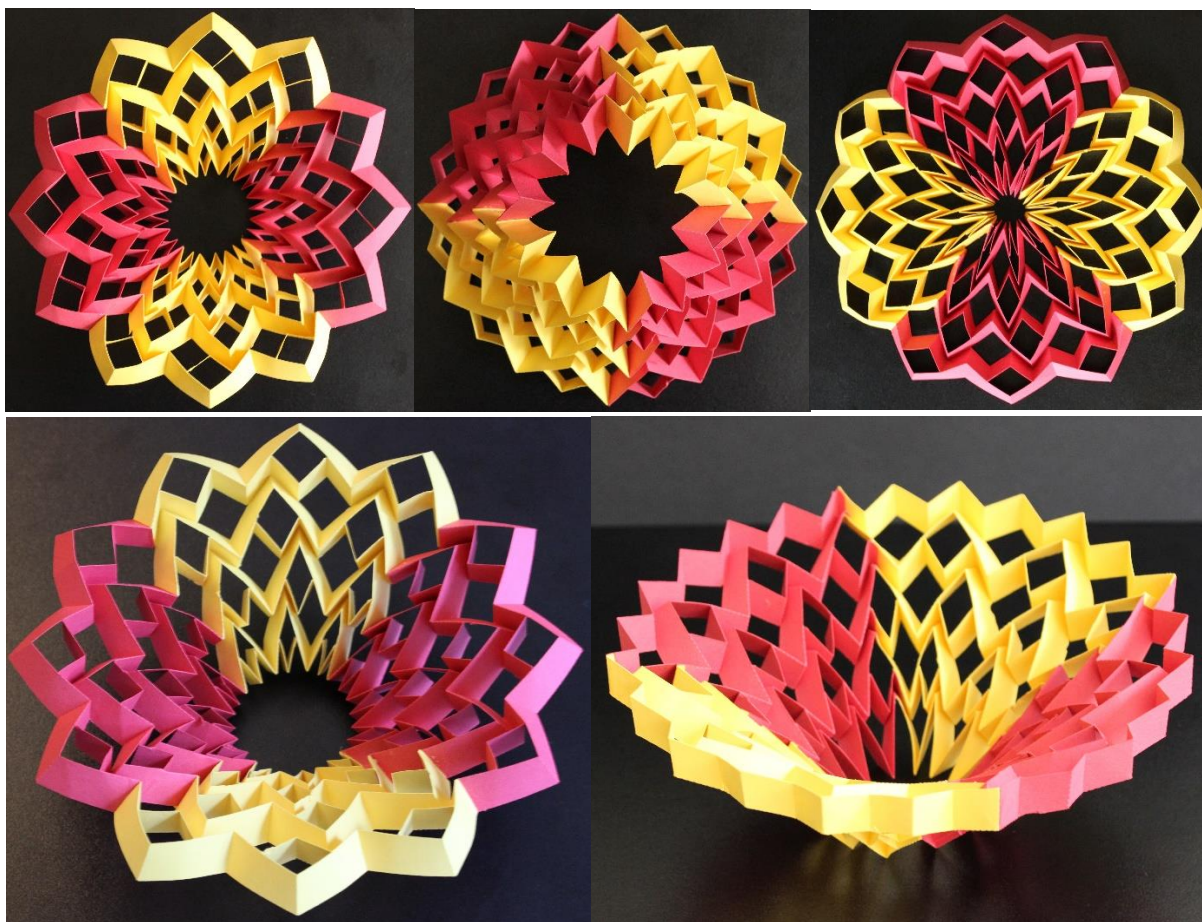
Figure A.1: Novel artworks related to the BCH$_2$ pattern. Figure shows different positions of a kinetic structure.

References

[1] H. C. Greenberg, M. L. Gong, S. P. Magleby and L. L. Howell, "Identifying links between origami and compliant," *Mechanical Sciences (Open Access),* p. 217–225, 2011.

[2] J. Vincent, "Deployable structures in nature," in *Deployable Structures*, New York, Springer-Verlag Wien, 2001, pp. 37-51.

[3] K. Miura and M. Natori, "2-D Array Experiment on Board a Space," *Space Power,* vol. 5, p. 345–356, 1985.

[4] K. Miura, "Concepts of deployable space structures," *International Journal of Space Structures,* vol. 8, no. 1, pp. 3-16, 1993.

[5] K. Kuribayashi, K. Tsuchiya, Z. You, D. Tomus, M. Umemoto, T. Ito and M. Sasaki, "Self-deployable origami stent grafts as a biomedical application of Ni-rich TiNi shape memory alloy foil," *Materials Science and Engineering: A,* vol. 419, no. 1-2, pp. 131-137, 2006.

[6] A. Heller, "A Giant Leap for Space Telescopes," *Science and Technology by Lawrence Livermore National Laboratory,* pp. 12-18, 2003.

[7] E. Elsayed and B. B. Basily, "A continuous folding process for sheet materials," *International Journal of Materials and Product Technology,* vol. 21, pp. 217-238, 2004.

[8] C. Cromvik, "Numerical Folding of Airbags Based on Optimization and Origami," Chalmers University of Technology and Goteborg University, Goteborg , 2007.

[9] J. Ma and Z. You, "Energy Absorption of Thin-Walled Square Tubes With a Prefolded Origami Pattern—Part I: Geometry and Numerical Simulation," *Journal of Applied Mechanics,* vol. 81, p. 011003, 2014.

[10] M. Schenk and S. D. Guest, "Geometry of Miura-folded metamaterials," *Proceedings of the National Academy of Sciences,* vol. 110, no. 9, pp. 3276-3281, 2013.

[11] S. D. Guest and S. Pellegrino, "Inextensional Wrapping of Flat Membranes," in *Proceedings of the First International Seminar on Structural Morphology*, Montpellier, 1992.

[12] T. Fukuchi, "Nagata Acoustics News," 25 December 2002. [Online]. Available: http://www.nagata.co.jp/news/news0212-e.htm.

[13] K. Fuchi, J. Tang, B. Crowgey, A. R. Diaz, E. J. Rothwell and R. O. Ouedraogo, "Origami Tunable Frequency Selective Surfaces," *Antennas and Wireless Propagation Letters, IEEE,* vol. 11, pp. 473-475, 2012.

[14] K. Kuribayashi and Z. You, "Deployable Stent". US Patent 7,060,092, 2006.

[15] K. Miura and T. Tachi, "Synthesis of rigid-foldable cylindrical polyhedra," *Journal of the International Society for the Interdisciplinary Study of Symmetry (ISIS-Symmetry),* no. Special Issue for the Festival-Congress, Gmünd, Austria, pp. 204-213, 2010.

[16] S. Heimbs, "Foldcore sandwich structures and their impact behaviour: An overview," in *Dynamic Failure of Composite and Sandwich Structures*, Springer Netherlands, 2013, pp. 491-544.

[17] A. Hanaor and R. Levy, "Evaluation of Deployable Structures for Space Enclosures," *Int. J. Space Struct.,* vol. 16, no. 4, pp. 211-229, 2001.

[18] N. Friedman, G. Farkas and A. Ibrahimbegovic, "Deployable/retractable structures towards sustainable development," *Pollack Periodica,* vol. 6, no. 2, p. 85–97, 2011.

[19] R. Kronenburg, Flexible: architecture that responds to change, Laurence King, 2007.

[20] T. Tachi, *Architectural Origami - Architectural Form Design Systems based on Computational Origami,* Lecture notes for MIT 6.849, 2010.

[21] A. E. Del Grosso and P. Basso, "Adaptive building skin structures," *Smart Materials and Structures,* vol. 19, no. 12, p. 124011, 2010.

[22] Y. Chen and J. Feng, "Folding of a Type of Deployable Origami Structures," *International Journal of Structural Stability and Dynamics,* vol. 12, no. 6, p. 1250054, 2012.

[23] M. Schenk and S. Guest, "Origami folding: A structural engineering approach," in *Origami 5: Fifth International Meeting of Origami Science, Mathematics, and Education (5OSME)*, 2011.

[24] K. Miura, "Method of packaging and deployment of large membranes in space," in *31st Congress of the International Astronautical Federation*, Japan Aerospace Exploration Agency, Tokyo, 1980.

[25] R. D. Resch and H. Christiansen, "The design and analysis of kinematic folded plate systems," in *Proceedings of IASS Symposium on Folded Plates and Prismatic Structures*, 1970.

[26] T. Tachi, M. Masubuchi and M. Iwamoto, "Rigid Origami Structures with Vacuumatics: Geometric Considerations," [Online]. Available: http://origami.c.u-tokyo.ac.jp/~tachi/cg/VacuumaticOrigamiIASS2012.pdf. [Accessed August 2015].

[27] K. Miura, "Proposition of pseudo-cylindrical concave polyhedral shells," in *Proceedings of IASS Symposium on Folded Plates and Prismatic Structures*, 1970.

[28] F. Heinzelmann, "Lightweight origami structure & daylighting modulation," in *Proceedings of the IASS Symposium*, Valencia, 2009.

[29] "Abu Dhabi Investment Council Headquarters (Al Bahr Towers)," ARUP, [Online]. Available: http://www.arup.com/projects/abu_dhabi_investment_council_headquarters/adic_gallery1.aspx.

[30] D. A. Huffman, "Curvature and creases: A primer on paper," *IEEE Transaction on Computers,* vol. 25, pp. 1010-1019, 1976.

[31] K. Miura, "A Note on Intrinsic Geometry of Origami, 6–7 December," in *Proc. 1st Int. Meet. of Origami Science*, Ferrara, Italy, 1989.

[32] T. Hull, in *Project Origami*, AK Peters, 2006, p. 229–235.

[33] N. Watanabe and K. Kawaguchi, "The method for judging rigid foldability," in *Origami4: Proceedings of the Fourth International Conference on Origami in Science, Mathematics, and Education*, 2009.

[34] T. Tachi, "Simulation of rigid origami," in *R.J. Lang, ed., Origami 4: Fourth International Meeting of Origami Science, Mathematics, and Education (4OSME)*, 175-188, 2009.

[35] S. M. Belcastro and T. C. Hull, "Modelling the folding of paper into three dimensions using affine transformations," *Linear Algebra and its Applications,* vol. 348, pp. 273-282, 2002.

[36] S. Krishnan, "The Christian Science Monitor," 17 September 2003. [Online]. Available: http://www.csmonitor.com/2003/0917/p01s03-woap.html. [Accessed 6 March 2014].

[37] Z. Wu, I. Hagiwara and X. Tao, "Optimisation of crush characteristics of the cylindrical origami structure," *International Journal of Vehicle Design,* vol. 43, no. 1-4, pp. 66-81, 2007.

[38] H. Engel, Structure Systems, Praeger, foreword by Ralph Rapson, 1968.

[39] Z. Y. Wei, Z. V. Guo, L. Dudte, H. Y. Liang and L. Mahadevan, "Geometric mechanics of periodic pleated origami," *Physical Review Letters,* vol. 110, no. 21, pp. 215501-215505, 2013.

[40] A. Norman, K. Seffen and S. Guest, "Morphing of Curved Corrugated Shells," *Int. J. Solids Structures,* vol. 46, no. 7-8, pp. 1624-1633, 2009.

[41] K. A. Seffen, "Compliant Shell Mechanisms," *Philosophical Transactions of the Royal Society of London A: Mathematical, Physical and Engineering Sciences,* vol. 370, no. 1965, pp. 2010-2026, 2012.

[42] K. Fuchi, A. R. Diaz, E. J. Rothwell, R. O. Ouedraogo and J. Tang, "An origami tunable metamaterial," *Journal of Applied Physics,* vol. 111, no. 8, p. 084905, 2012.

[43] "Resonant Chamber," [Online]. Available: http://archinect.com/firms/project/14483206/resonant-chamber/45313996.

[44] C. L. Randall, E. Gultepe and D. H. Gracias, "Self-folding devices and materials for biomedical applications," *Trends in biotechnology,* vol. 30, no. 3, pp. 138-146, 2012.

[45] L. Ionov, "Soft microorigami: self-folding polymer films," *Soft Matter,* vol. 7, no. 15, pp. 6786-

6791, 2011.

[46]   E. G. Rapp, "Sandwich-type structural element". United States of America Patent 2,963,128, 6 December 1960.

[47]   G. A. Sehrndt, "Verbundplatte und Verfahren zu ihrer Herstellung". DD Patent 1434112, 1960.

[48]   K. Miura, "Map fold a la Miura style, its physical characteristics and application to the space science," *Research of Pattern Formation,* no. ed R Takaki (Tokyo: KTK), pp. 77-90, 1994.

[49]   M. Schenk, S. D. Guest and G. J. McShane, "Novel stacked folded cores for blast-resistant sandwich beams," *International Journal of Solids and Structures,* vol. 51, no. 25, pp. 4196-4214, 2014.

[50]   J. L. Silverberg, A. A. Evans, L. McLeod, R. C. Hayward, T. Hull, C. D. Santangelo and I. Cohen, "Using origami design principles to fold reprogrammable mechanical metamaterials," *Science ,* vol. 345, no. 6197, pp. 647-650, 2014.

[51]   S. Li and K. W. Wang, "Fluidic origami cellular structure--combining the plant nastic movements with paper folding art," in *Proceedings SPIE 9431, Active and Passive Smart Structures and Integrated Systems*, San Diego, California, United States, 2015.

[52]   A. Brunner, "Expansible Surface Structure". United States of America Patent 3362118, 9 January 1968.

[53]   Z. You and K. Kuribayashi, "Expandable tubes with negative Poisson's ratio and their application in medicine," in *Origami4: Fourth International Meeting of Origami Science, Mathematics, and Education*, 2009.

[54]   J. Ma and Z. You, "Modelling of the Waterbomb Origami Pattern and its Applications," in *Proceedings of the ASME 2014 International Design Engineering Technical Conferences and Computers and Information in Engineering Conference (IDETC/CIE)*, Buffalo, New York, USA, 2014.

[55]   D.-Y. Lee, J.-S. Kim, S.-R. Kim, J.-S. Koh and K.-J. Cho, "The Deformable Wheel Robot Using Magic-Ball Origami Structure," in *Proceedings of the ASME 2013 International Design Engineering Technical Conferences & Computers and Information in Engineering Conference, IDETC/CIE*, Oregon, 2013.

[56]   "Archinet," [Online]. Available: http://archinect.com/firms/project/14483206/resonant-chamber/45313996.

[57]   H. U. Buri, "Origami - Folded Plate Structures; PhD Thesis," École Polytechnique Fédérale De Lausanne, 2010.

[58]   R. H. Knapp, "Pseudo-cylindrical shells: A new concept for undersea structures," *Journal of Engineering for Industry,* vol. 99, no. 2, pp. 485-492, 1977.

[59] I. Katsuhiro, M. Ishinabe, S. Kobayashi, H. Matsubayashi and Y. Nishimura, "Packing can". US Patent 5,100,017, 31 March 1992.

[60] H. Buri and Y. Weinand, "ORIGAMI-folded plate structures, architecture," in *10th World Conference on Timber Engineering*, 2008.

[61] H. Khalilpasha and A. F, "Textured deep subsea pipelines," *International Journal of Mechanical Sciences,* vol. 68, pp. 224-235, 2013.

[62] T. Tachi and K. Miura, "Rigid-Foldable Cylinders and Cells," *Journal of the International Association for Shell and Spatial Structures (IASS),* vol. 53, no. 4, pp. 217-226, 2012.

[63] K. C. Cheung, T. Tachi, S. Calisch and K. Miura, "Origami interleaved tube cellular materials," *Smart Materials and Structures ,* vol. 23, no. 9, p. 094012, 2014.

[64] T. Nojima and K. Saito, "Development of newly designed ultra-light core structures," *JSME International Journal Series A,* vol. 49, no. 1, pp. 38-42, 2006.

[65] M. Eidini and G. H. Paulino, "Unravelling Metamaterial Properties in Zigzag-base Folded Sheets," *Science Advances,* vol. 1, no. 8, p. e1500224, 2015.

[66] E. A. Peraza-Hernandez, D. J. Hartl, R. J. Malak Jr and D. C. & Lagoudas, "Origami-inspired active structures: a synthesis and review," *Smart Materials and Structures ,* vol. 23, no. 9, p. 094001, 2014.

[67] B. H. Hanna, J. M. Lund, R. J. Lang, S. P. Magleby and L. L. Howell, "Waterbomb base: a symmetric single-vertex bistable origami mechanism," *Smart Materials and Structures,* vol. 23, no. 9, p. 094009, 2014.

[68] K. Miura, "Zeta-Core Sandwich - Its Concept and Realization," *Inst. of Space and Aeronautical Science, University of Tokyo,* vol. 480, pp. 137-164, 1972.

[69] F. Haas and R. J. Wootton, "Two basic mechanisms in insect wing folding," *Proceedings of the Royal Society of London.Series B: Biological Sciences,* vol. 263, pp. 1651-1658, 1996.

[70] H. Kobayashi, B. Kresling and J. F. V. Vincent, "The geometry of unfolding tree leaves," *Proceedings of the Royal Society of London.Series B: Biological Sciences,* vol. 265, pp. 147-154, 1998.

[71] L. Mahadevan and S. Rica, "Self-organized origami," *Science,* vol. 307, p. 1740, 2005.

[72] B. Audolya and A. Boudaoud, "Buckling of a stiff film bound to a compliant substrate—Part III: Herringbone solutions at large buckling parameter," *J. Mech. Phys. Solids,* vol. 56, pp. 2444-2458, 2008.

[73] K. Miura, "The science of Miura-ori: a review," in *4th International Meeting of Origami Science, Mathematics, and Education, RJ Lang, Ed., AK Peters*, 2009.

[74] X. Chen and J. W. Hutchinson, "Herringbone buckling patterns of compressed thin films on compliant substrates," *Journal of Applied Mechanics,* vol. 71, pp. 597-603, 2004.

[75] M. B. Amar and F. Jia, "Anisotropic growth shapes intestinal tissues during embryogenesis," *Proceedings of the National Academy of Sciences,* vol. 110, no. 26, pp. 10525-10530, 2013.

[76] A. E. Shyer, T. Tallinen, N. L. Nerurkar, Z. Wei, E. S. Gil, D. L. Kaplan, C. J. Tabin and L. Mahadevan, "Villification: how the gut gets its villi," *Science,* vol. 342, no. 6155, pp. 212-218, 2013.

[77] J. Ginepro and T. C. Hull, "Counting Miura-ori foldings," *Journal of Integer Sequences,* vol. 17, no. 2, p. 14.10.8, 2014.

[78] C. Lv, D. Krishnaraju, G. Konjevod, H. Yu and H. Jiang, "Origami based Mechanical Metamaterials," *Scientific Reports,* vol. 4, p. 5979, 2014.

[79] "ART.COM," [Online]. Available: http://www.art.com.

[80] "Garden Centre Online," [Online]. Available: http://www.gardencentreonline.co.uk/1-meter-of-hornbeam-hedging-plants-carpinus-betulus-4-plants.html#prettyPhoto/0/. [Accessed 4 March 2014].

[81] T. Tachi, "One-DOF cylindrical deployable structures with rigid quadrilateral panels," in *Symposium of the International Association for Shell and Spatial Structures*, Valencia, 2009.

[82] D. Balkcom, "Robotic origami folding," 2004.

[83] W. McGuire, R. H. Gallagher and R. D. Ziemian, Matrix Structural Analysis, New York: Wiley, 2000.

[84] N. Bassik, G. M. Stern and D. H. Gracias, "Microassembly based on hands free origami with bidirectional curvature," *Applied physics letters,* vol. 95, no. 9, p. 091901, 2009.

[85] K. Saito, F. Agnese and F. Scarpa, "A cellular kirigami morphing wingbox concept," *Journal of intelligent material systems and structures 22,* vol. 22, no. 9, pp. 935-944, 2011.

[86] F. Scarpa, M. Ouisse, M. Collet and K. Saito, "Kirigami auxetic pyramidal core: mechanical properties and wave propagation analysis in damped lattice," *Journal of Vibration and Acoustics ,* vol. 135, no. 4, p. 041001, 2013.

[87] Y. Hou, R. Neville, F. Scarpa, C. Remillat, B. Gu and M. Ruzzene, "Graded conventional-auxetic Kirigami sandwich structures: Flatwise compression and edgewise loading," *Composites Part B: Engineering,* vol. 59, pp. 33-42, 2014.

[88] A. Alderson and K. L. Alderson, "Auxetic Materials," *Proceedings of the Institution of Mechanical Engineers, Part G: Journal of Aerospace Engineering,* vol. 221, no. 4, pp. 565-575, 2007.

[89] R. Lakes, "Foam structures with a negative Poisson's ratio," *Science,* vol. 235, no. 4792, pp. 1038-1040, 1987.

[90] T. C. T. Ting and T. Chen, "Poisson's ratio for anisotropic elastic materials can have no bounds," *The quarterly journal of mechanics and applied mathematics,* vol. 58, no. 1, pp. 73-82, 2005.

[91] A. Alderson, K. L. Alderson, G. Chirima, N. Ravirala and K. M. Zied, "The in-plane linear elastic constants and out-of-plane bending of 3-coordinated ligament and cylinder-ligament honeycombs," *Composites Science and Technology ,* vol. 70, no. 7, pp. 1034-1041, 2010.

[92] T. Lim, "On simultaneous positive and negative Poisson's ratio laminates," *physica status solidi (b) ,* vol. 244, no. 3, pp. 910-918, 2007.

[93] S. Felton, M. Tolley, E. Demaine, D. Rus and R. Wood, "A method for building self-folding machines," *Science ,* vol. 345, no. 6197 , pp. 644-646, 2014.

[94] M. Eidini, "Zigzag-base folded sheet cellular mechanical metamaterials," *Under Review.*

[95] K. Miura, "The science of miura-ori," in *4th International Meeting of Origami Science, Mathematics, and Education, RJ Lang, Ed., AK Peters*, 2009.

[96] K. Tanizawa and K. Miura, "Large displacement configurations of bi-axially compressed infinite plate," *Japan Society for Aeronautical and Space Sciences, Transactions,* vol. 20, pp. 177-187, 1978.

[97] M. Schenk and S. D. Guest, "Geometry of miura-folded metamaterials," *Proceedings of the National Academy of Sciences,* vol. 110, no. 9, pp. 3276-3281, 2013.

[98] Z. T. M. Song, R. Tang, Q. Cheng, X. Wang, D. Krishnaraju, R. Panat, C. K. Chan, H. Yu and H. Jiang, "Origami lithium-ion batteries," *Nature communications,* vol. 5, p. 3140 , 2014.

[99] T. Tachi, "Generalization of rigid foldable quadrilateral mesh origami," in *Proc. of the Int. Association for Shell and Spatial Structures (IASS) Symp*, Valencia, Spain, 2009.

[100] F. Gioia, D. Dureisseix, R. Motro and B. Maurin, "Design and analysis of a foldable/unfoldable corrugated architectural curved envelop," *Journal of Mechanical Design,* vol. 134, no. 3, p. 031003, 2012.

[101] S. Heimbs, "Foldcore sandwich structures and their impact behaviour: An overview," in *Dynamic Failure of Composite and Sandwich Structures*, Springer Netherlands, 2013, pp. 491-544.

[102] K. E. Evans and A. Alderson, "Auxetic materials: functional materials and structures from lateral thinking!," *Advanced materials ,* vol. 12, no. 9, pp. 617-628, 2000.

[103] W. Yang, Z.-M. Li, W. Shi, B.-H. Xie and M.-B. Yang, "Review on auxetic materials," *Journal of materials science,* vol. 39, no. 10, pp. 3269-3279, 2004.

[104] A. Alderson and K. L. Alderson, "Auxetic Materials," *Proceedings of the Institution of Mechanical Engineers, Part G: Journal of Aerospace Engineering,* vol. 221, no. 4, pp. 565-575, 2007.

[105] J. N. Grima, A. Alderson and K. E. Evans, "Auxetic behaviour from rotating rigid units," *Physica status solidi (b),* vol. 242, no. 3, pp. 561-575, 2005.

[106] J. N. Grima, V. Zammit, R. Gatt, A. Alderson and K. E. Evans, "Auxetic behaviour from rotating semi-rigid units," *Physica Status Solidi (b) ,* vol. 244, no. 3, pp. 866-882, 2007.

[107] D. Prall and R. S. Lakes, "Properties of a chiral honeycomb with a Poisson's ratio of -1," *International Journal of Mechanical Sciences,* vol. 39, no. 3, pp. 305-314, 1997.

[108] A. Spadoni and M. Ruzzene, "Elasto-static micropolar behavior of a chiral auxetic lattice," *Journal of the Mechanics and Physics of Solids,* vol. 60, no. 1, pp. 156-171, 2012.

[109] R. F. Almgren, "An isotropic three-dimensional structure with Poisson's ratio -1," *Journal of Elasticity ,* vol. 15, no. 4, pp. 427-430, 1985.

[110] K. E. Evans, A. Alderson and F. R. Christian, "Auxetic two-dimensional polymer networks. An example of tailoring geometry for specific mechanical properties," *J. Chem. Soc., Faraday Trans.,* vol. 91, no. 16, pp. 2671-2680, 1995.

[111] H. Yasuda and J. Yang, "Reentrant Origami-Based Metamaterials with Negative Poisson's Ratio and Bistability," *Physical Review Letters,* vol. 114, no. 18, p. 185502, 2015.

[112] K. Bertoldi, P. M. Reis, S. Willshaw and T. Mullin, "Negative Poisson's ratio behavior induced by an elastic instability," *Advanced Materials,* vol. 22, no. 3, pp. 361-366, 2010.

[113] S. Babaee, J. Shim, J. C. Weaver, E. R. Chen, N. Patel and K. Bertoldi, "3D soft metamaterials with negative Poisson's ratio," *Advanced Materials,* vol. 25, no. 36, pp. 5044-5049, 2013.

[114] Y. Cho, J.-H. Shin, A. Costa, T. A. Kim, V. Kunin, J. Li, S. Y. Lee, S. Yange, H. Nam Hanf, I.-S. Choi and D. J. Srolovitze, "Engineering the shape and structure of materials by fractal cut," *Proceedings of the National Academy of Sciences ,* vol. 111, no. 49, pp. 17390-17395, 2014.

[115] Z. Wang and H. Hu, "3D auxetic warp-knitted spacer fabrics," *physica status solidi (b),* vol. 251, no. 2, pp. 281-288, 2014.

[116] M. Glazzard and P. Breedon, "Weft-knitted auxetic textile design," *Physica Status Solidi (b),* vol. 251, no. 2, pp. 267-272, 2014.

[117] H. Kobayashi, B. Kresling and J. F. V. Vincent, "The geometry of unfolding tree leaves," *Proceedings of the Royal Society of London. Series B: Biological Sciences,* vol. 265, pp. 147-154, 1998.

[118] J. A. Rogers, T. Someya and Y. Huang, "Materials and mechanics for stretchable electronics," *Science,* vol. 327, no. 5973, pp. 1603-1607, 2010.

[119] Y. Zhang, Y. Huang and J. A. Rogers, "Mechanics of stretchable batteries and supercapacitors," *Current Opinion in Solid State and Materials Science,* 2015.

[120] A. Lamoureux, K. Lee, M. Shlian, S. R. Forrest and M. Shtein, "Dynamic kirigami structures for integrated solar tracking," *Nature communications,* p. 6:8092, 2015.

[121] T. Castle, Y. Cho, X. Gong, E. Jung, D. M. Sussman, S. Yang and R. D. Kamien, "Making the cut: Lattice kirigami rule," *Physical review letters,* vol. 113, no. 24, p. 245502, 2014.

[122] J. M. Gattas, W. Wu and Z. You, "Miura-Base Rigid Origami: Parameterizations of First-Level Derivative and Piecewise Geometries," *Journal of Mechanical Design,* vol. 135, no. 11, p. 111011, 2013.

[123] S. A. Zirbel, R. J. Lang, M. W. Thomson, D. A. Sigel, P. E. Walkemeyer, B. P. Trease, S. P. Magleby and L. L. Howell, "Accommodating thickness in origami-based deployable arrays," *Journal of Mechanical Design,* vol. 135, no. 11, p. 111005, 2013.

[124] M. Eidini and D. P. Abrams, "Lateral force distributions for various types of hybrid masonry panels," in *Proceedings of the Eleventh North American Masonry Conference*, Minneapolis, Minnesota, USA, 2011.

[125] D. T. Biggs, "Hybrid Masonry Structures," in *Proceedings of the Tenth North American Masonry Conference*, Boulder, Colorado, USA, 2007.

[126] NCMA, "Hybrid concrete masonry design, TEK 14-9A," National Concrete Masonry Association , Herndon, Virginia, USA, 2009.

[127] D. P. Abrams, "NSF NEESR research on hybrid masonry seismic structural systems," in *Proceedings of the Eleventh North American Masonry Conference*, Minneapolis, Minnesota, USA, 2011.

[128] R. Elements, *Bentley RAM Elements , Version 10.7.0.17,* 2010.

[129] L. L. Pook and J. L. Dawe, "Effects of Interface conditions Between a Masonry Shear Panel and Surrounding Steel Frame," in *Proceedings of the Forth Canadian Masonry Symposium*, 1986.

[130] J. L. Dawe and C. K. Seah, "Behavior of masonry infilled steel frames," *Canadian Journal of Civil Engineering,* pp. 865-876, 1989.

[131] M. Eidini, D. Abrams and L. Fahnestock, "Seismic Design and Viability of Hybrid Masonry Building Systems," *J. Struct. Eng.,* vol. 139, no. 3, pp. 411-421, 2013.

[132] V. Bertero and S. Brokken, "Infills in seismic resistant building," *Journal of Structural Engineering,* vol. 109, no. 6, p. 1337–1361, 1983.

[133] NCMA, "Hybrid concrete masonry construction details, TEK 3-3B," National Concrete Masonry Association, Herndon, Virgina, USA, 2009.

[134] G. Johnson, I. N. Robertson, S. Goodnight and R. Ozaki-Train, "Behavior of energy dissipating connectors and fuses," in *Proceedings of the Eleventh North American Masonry Conference*, Minneapolis, MN, 2011.

[135] S. R. Goodnight, P. Johnson G and I. N. Robertson, "Connector development for hybrid masonry seismic structural systems, Research Report UHM/CEE/11-03," University of Hawaii, Manoa, HI, 2011.

[136] R. Ozaki-Train and I. N. Robertson, "Hybrid masonry connector development and design, Research Report UHM/CEE/11-04," University of Hawaii, Manoa, HI, 2011.

[137] T. Paulay and M. J. N. Priestley, Seismic Design of Reinforced Concrete and Masonry Buildings, New York: Wiley, 1992.

[138] ASCE, "Minimum design loads for buildings and other structures - ASCE/SEI 7-10 (2010)," ASCE, Reston, VA, 2010.

[139] D. P. Abrams, "A set of class notes for a course in masonry structures," Department of Civil and Environmental Engineering, Univ. of Illinois at Urbana-Champaign, Urbana, IL, 2009.

[140] P. Soroushian, K. Obaseki and K. Choi, "Non-linear modeling and seismic analysis of masonry shear walls," *Journal of Structural Engineering,* vol. 114, no. 5, p. 1106–1119, 1988.

[141] MSJC, "Building Code Requirements for Masonry Structures (ACI 530-05/ASCE 5-05/TMS 402-05)," The Masonry Society (TMS), Boulder, CO, 2008.

[142] C.-M. Uang, M. Bruneau, A. S. Whittaker and K.-C. Tsai, "Seismic design of steel structures," in *The Seismic Design Handbook*, 2 ed., F. Naeim, Ed., Boston, Kluwer Academic Publishers, 2001, pp. 409-462.

[143] A. S. Elnashai and L. Di Sarno, Fundamentals of earthquake engineering, New York: Wiley, 2008.

[144] AISC, "Specification for Structural Steel Buildings - ANSI/AISC 360-10," American Institute of Steel Construction, Chicago, 2010.

[145] AISC, "Seismic Provisions for Structural Steel Buildings - ANSI/AISC 341-10," American Institute of Steel Construction, Chicago, 2010.

[146] FEMA, "Structural steel design. Chapter 5, NEHRP recommended provisions: Design examples," Building Seismic Safety Council, National Institute of Building Sciences, Washington, DC, 2006.

[147] D. P. Abrams, L. A. Fahnestock and M. Eidini, "Basic mechanisms for hybrid masonry structures," in *Proceedings of the 2010 ASCE Structures Congress*, 2010.

[148] A. K. Chopra and R. K. Goel, "Capacity-demand-diagram methods based on inelastic design spectrum," *Earthquake spectra,* vol. 15, no. 4, pp. 637-656, 1999.

[149] P. Fajfar, "Capacity spectrum method based on inelastic demand spectra," *Earthquake Engineering & Structural Dynamics,* vol. 28, no. 9, pp. 979-993, 1999.

[150] S. A. Freeman, "The Capacity Spectrum Method as a Tool for Seismic Design," in *Proceedings of the 11th European conference on earthquake engineering*, 1998.

[151] S. A. Freeman, "Review of the development of the capacity spectrum method," *ISET Journal of Earthquake Technology,* vol. 41, no. 1, pp. 1-13, 2004.

[152] C. Casarotti and R. Pinho, "An adaptive capacity spectrum method for assessment of bridges subjected to earthquake action," *Bulletin of Earthquake Engineering,* vol. 5, no. 3, pp. 377-390, 2007.

[153] ATC, "Seismic Evaluation and Retrofit of Concrete Buildings," ATC 40, Applied Technology Council, Redwood City, CA, 1996.

[154] G. Al-Chaar, "Evaluating strength and stiffness of unreinforced masonry infill structures. Report No. ERDC/CERL TR-02-1," U.S. Army Corps of Engineers, Champaign, IL, 2002.

[155] RAM, *Bentley RAM Elements , Version 10.7.0.17,* 2010.

[156] M. R. Maheri and R. Akbari, "Seismic behaviour factor, R, for steel X-braced and knee-braced RC buildings," *Engineering structures,* vol. 25, no. 12, pp. 1505-1513, 2003.

[157] M. S. Medhekar and D. J. L. Kennedy, "Displacement-based seismic design of buildings-theory," *Engineering structures,* vol. 22, no. 3, pp. 201-209, 2000.